DEFECT-MEDIATED TRANSFORMATIONS IN THIN METAL FILMS

A Dissertation

Presented to the Faculty of the Graduate School

of Cornell University

In Partial Fulfillment of the Requirements for the Degree of

Doctor of Philosophy

by

Elizabeth Anne Ellis

August 2018

DEFECT-MEDIATED TRANSFORMATIONS IN THIN METAL FILMS

Elizabeth Anne Ellis

Cornell University 2018

Thin metal films are widely used in industry, and often show strikingly different behavior than the same material bulk form. Two thin-film phenomena were explored in this work: the β-to-α phase transformation in tantalum thin films, and the (111)-to-(100) texture transformation in face-centered cubic metal thin films. Both are revealed to rely on specific defect structures.

To understand the β-to-α phase transformation in Ta films, we first investigated the nature of the metastable β phase of tantalum. A series of Ta films was deposited in an ultra-high vacuum system under varying Ar sputter pressures to investigate the role of energetic deposition on phase formation, structure, and properties. By measuring the stress in each film, we unambiguously established that only the β phase of Ta appears, despite large variations in deposition energy. All films exhibit (002) fiber texture, and the while the breadth of this component increased with increasing sputter pressure, no other texture component appeared. In comparing these results with a detailed review of the literature, a theory of phase selection in Ta films was formulated that is consistent with virtually all reported results. As these films consist of 100% β-Ta with no evidence of contamination with either oxygen or the stable α phase, we were also able to provide representative measurements of the resistivity and Hall-Petch constants of pure β-Ta.

When annealed, these films underwent the β-to-α phase transformation, and electron backscatter diffraction revealed that they formed an unusual microstructure with continuous

orientation gradients and discontinuous grain boundaries. The variation in initial β-Ta microstructure resulted in substantial variation in the phase-transformed microstructure. The magnitude of the orientation gradient decreased with increasing sputter pressure, and the distance between high-angle orientation increased with increasing sputter pressure. We propose a simple rotation mechanism by which the orientation gradient might form, which is consistent with all observed variations in the gradient microstructure. Using a genetic algorithm, we identified the geometrically necessary dislocations needed to produce these orientation gradient patterns according to this mechanism.

The (111)-to-(100) texture transformation is a well-known phenomenon occurring in FCC films deposited with (111) fiber texture. Upon annealing, films below some critical thickness retain (111) texture, while those above the critical thickness transform to a (100) texture. The transformation is often explained by a competition between strain energy and interface energy: thin films retain (111) texture because the (111) interface has low surface energy, while thick films transform to (100) because the (100) orientation is more compliant and therefore has a lower strain energy for a given strain. However, recent work has suggested that neither strain energy nor interface energy play a dominant role in the transformation. We investigated the driving forces involved in this transformation by using a bulge test to induce different strain energies in thin Ag films under identical annealing conditions, and observing the progression of the texture transformation using synchrotron x-ray diffraction. Despite a large change in strain energy, the applied stresses had no effect on the transformation. We therefore evaluated various defects as potential driving forces for the transformation, and show that nanotwins provide both an adequate driving force and a potential orientation selection mechanism for the (111)-to-(100) transformation.

Biographical Sketch

Elizabeth Ellis grew up in Washington State and attended Harvey Mudd College in Claremont, California for her undergraduate degree, where she received a Bachelor of Science in Engineering. While studying civil structures at Mudd, she realized she wanted to understand more about the fundamental science underlying the dams and bridges she tested. This led her to graduate school at Cornell University, where she has studied under Professor Shefford Baker in the field of Theoretical and Applied Mechanics. She currently lives in Oak Ridge, Tennessee.

Acknowledgements

This thesis was made possible by the contributions and support of many people. All of them deserve my thanks.

First, to Professor Baker: Thank you for all of the directing, advising, teaching and coaching you've provided over the years. Under your guidance I've become a better researcher, a better writer, a better teacher, and a better speaker.

To my committee members, Professor Miller and Professor Thompson: Thank you both for engaging with my project and always being available for discussion and advice.

To Markus: Thank you for teaching me everything I now about the day-to-day running of a lab, not to mention all your help with experiments.

To Marissa and Ari: Thank you both for all you work on these projects, and for always being willing to put in late nights and early mornings.

To the rest of the Baker group: Thank you all for listening to countless hours of practice presentations, and for the company and commiseration.

To Mick Thomas, John Grazul, John Hunt, Don Werder, Phil Carubia, and Maura Weathers: Thank you for all of your help with your equipment, especially on the weekend and in the middle of the night.

To Marcia Sawyer and Michele Conrad: Thank you for all of your help with last-minute scheduling and paperwork.

To all of my Ithaca friends: Thank you for keeping me healthy and sane.

To my family: Thank you for years of unconditional support and encouragement, without which I would not have made it this far.

Finally, to Mitchell: Thank you for being so nice to me. I'm not sure if you knew, but I like you.

Table of Contents

List of Figures

CHAPTER 1

Introduction

Thin films underlie a vast number of modern technologies, from microelectronics to telescopes to medical implants. Because of their small size, thin metal films often have unusual properties that differ markedly from the properties of the same metal in bulk form. The non-equilibrium processes used to deposit thin films often result in microstructures, phases, and behavior seen only in thin films. As such, thin films have received, and continue to receive, considerable study.

This thesis focuses on two important transformations that occur only in thin films: the β-to-α phase transformation in tantalum films, and the (111)-to-(100) texture transformation in face-centered cubic films. Both have important implications for devices using these films, and, as we will show, both are governed by structural defects caused by non-equilibrium deposition processes.

1.1 Thin film structure

Metal films consist of a thin metal layer on a substrate. There are many techniques used to manufacture thin metal films, but this thesis will focus on two methods of physical vapor deposition, electron beam evaporation and DC magnetron sputtering. In e-beam evaporation, an electron beam heats a small amount of high-purity metal so that it evaporates and condenses on a substrate. In sputtering, a plasma is lit between the substrate and a metal target, and energetic ions in the plasma eject atoms from the target which then deposit on the substrate.

The resulting film may have a wide range of structures and properties, and in order to understand and organize these structures, several researchers have developed structure zone models describing the thin film structures that result from various combinations of deposition parameters. The first such model was developed by Movchan and Demischen [1] and classifies film structures into three zones based on the homologous temperature at which the film is deposited. The best-known structure zone model, developed by Thornton [2], adds sputter gas pressure as an additional parameter, and adds a fourth structure zone. The resulting model incorporates effects of shadowing, surface diffusion, and bulk diffusion, as summarized in Figure 1.1, below, from [2].

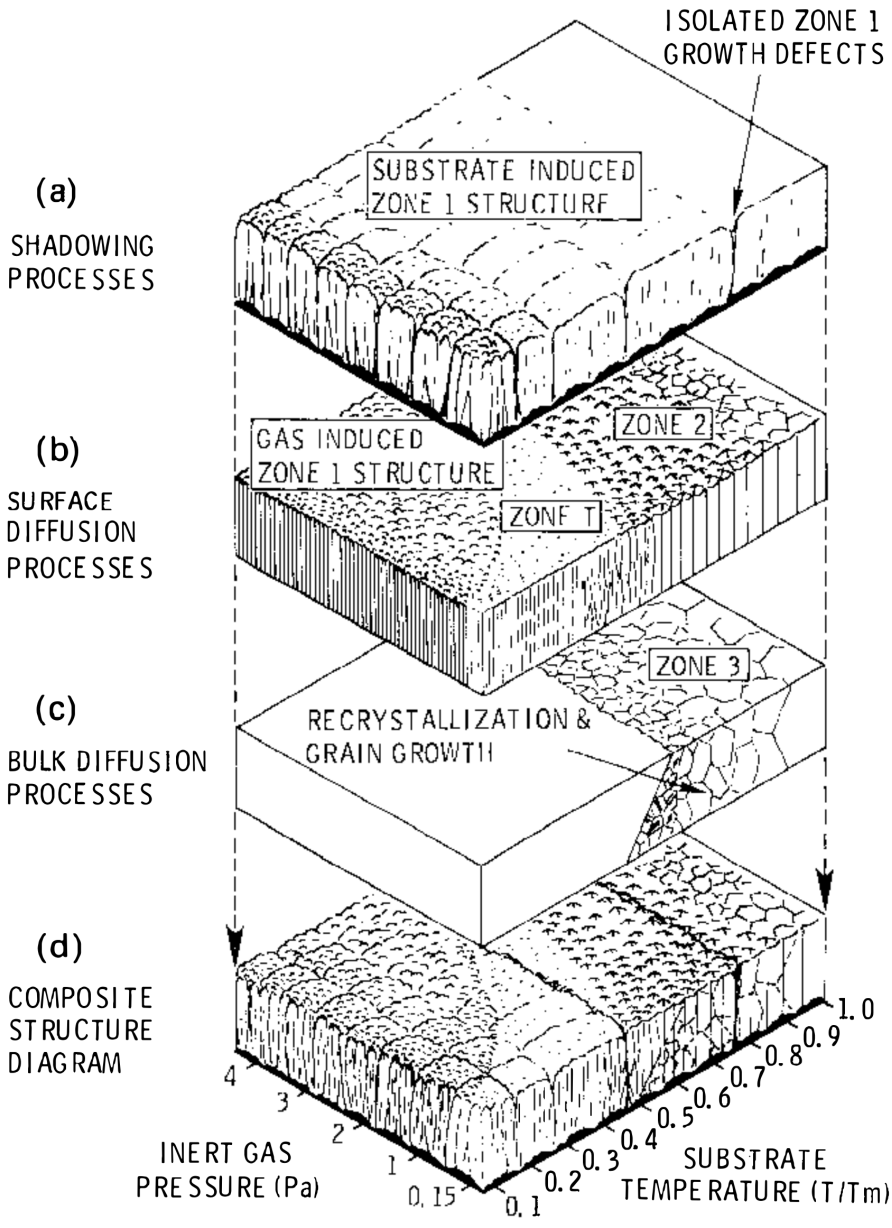

Figure 1.1: Structure zone model developed by Thornton, from [2]*. Thin film structures are divided into four zones depending on homologous temperature and background gas pressure based on the effects of shadowing, surface diffusion and bulk diffusion.*

This model divides film structures into four zones. Zone 1, at low homologous temperature and high gas pressure, consists of highly dislocated conical crystals separated by low-density or voided boundaries, and have low lateral strength. Zone T, at low homologous temperature and low gas pressure, is a transition zone between zones 1 and 2, and has similar

tapered crystals but with dense grain boundaries. As homologous temperature increases, gas pressure exerts less influence. Zone 2, at moderate homologous temperature, consists of relatively defect-free columnar grains separated by high-density boundaries. Zone 3, at high homologous temperature, features equiaxed grains.

Broadly speaking, Zone 1 structure is thought to be caused by a combination of very low diffusion and atomic shadowing, wherein substrate roughness of the growing film blocks certain areas from receiving an adequate flux of depositing material. These shadowed areas are voided or less dense in the final film and form the characteristic low-density boundaries of the Zone 1 structure. As homologous temperature and therefore mobility increases, diffusion becomes more effective. Surface diffusion takes effect first, allowing adatoms to fill spaces that would otherwise have been shadowed and underdense. The resulting Zone 2 structure features columnar grains that develop from the initial nuclei appearing in the first few layers of growth. Once homologous temperature has increased enough to allow for diffusion below the surface of the growing film, the film may recrystallize to form the equiaxed Zone 3 structure.

The second axis of Thornton's structure zone model, sputter gas pressure, indicates that the model was created with sputter deposition in mind. The primary way that sputter pressure affects film structure is by the process of thermalization, in which energetic depositing atoms collide with background gas atoms and lose energy and change direction in the process. More background gas atoms lead to more collisions and therefore lower energy depositing atoms. If enough gas atoms are present, depositing atoms eventually reach the kinetic energy of the background gas and approach the substrate from randomized directions and are considered to have been "thermalized". In Thornton's model, the distinction between low and high gas pressure is reflected primarily in the difference between Zone 1 and Zone T. The Zone T

structure is essentially the limit of the open Zone 1 structure in the case of minimal shadowing effects: adatoms do not have enough mobility to diffuse once they reach the surface, but are not prevented from reaching certain areas by substrate roughness or by the interaction of an oblique depositing flux with the growing film. The Zone T structure therefore has denser boundaries.

The observations underlying Thornton's structure zone model still shed light on evaporated films. The effects of homologous temperature are essentially unchanged by the method of deposition, and the effects of sputter pressure are analogous to the combined effects of adatom energy and shadowing. Evaporation results in relatively low-energy deposition, but also involves virtually no collisions with background gas atoms, as no backfill with inert gas is necessary for evaporation as it is with sputtering. This means that, under good vacuum and over reasonable source-substrate distances, depositing atoms travel along essentially line-of-sight paths from the source to the substrate, meaning shadowing is less prominent.

1.2 Equal biaxial stresses in thin films

Thin films are subject to a number of stresses throughout their lifetimes. They may experience fully internal stresses resulting from non-equilibrium deposition methods, as well as completely externally imposed stresses. Thin films are also subject to another class of stresses caused by their interaction with their substrate.

Substrate interaction stresses occur whenever the film and the substrate would, in a relaxed state, be of different lateral dimensions, but are forced to have the same dimensions. (These stresses are often called "intrinsic" or "internal" stresses, but this terminology is confusing as they are internal only to the film/substrate pair, not to the film itself. The term "substrate interaction stress" will be used throughout this thesis.) Such stresses are virtually

always present in thin films and can be remarkably high, leading to complications for many thin film applications.

A schematic showing the role of lateral dimensions in substrate interaction stress is shown in Figure 1.2, from [3].

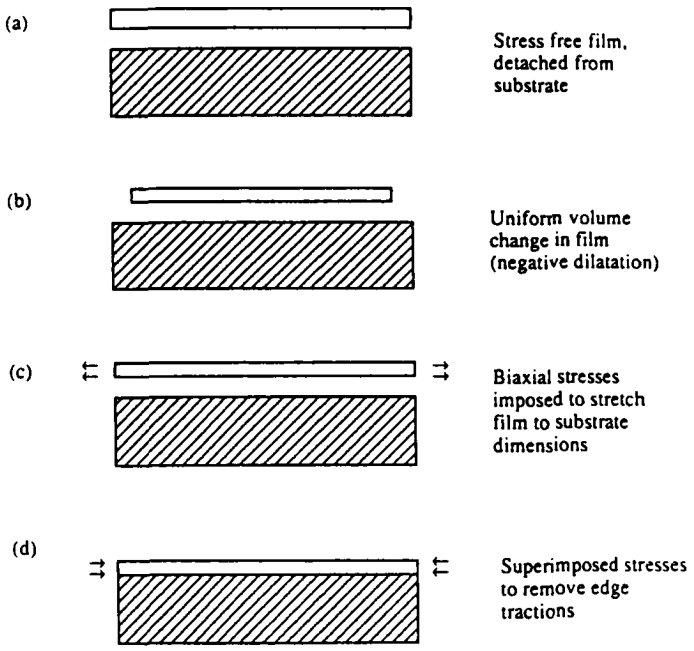

Figure 1.2: Development of equal biaxial film stress due to dimension changes in the film. From [3].

We first imagine a stress-free film, detached from its substrate (a). Because the film is stress-free, it must have the same dimensions when it is removed from the substrate. We then apply a uniform volume change to the film (b). Now, if the film is to be reattached to the substrate, an imposed stress is required to stretch the film back to its original lateral dimensions (c). In particular, if the film can be treated as homogeneous and isotropic in the plane, the imposed stress must be an equal biaxial form: No stress need be applied in the film normal direction, and an equal stress must be applied in the two in-plane directions. For this reason, the full stress tensor describing the stress state in a film is commonly represented by a single scalar value, the magnitude of the equal biaxial stress. This is an assumption, but a useful one, as it is valid in

many common situations. Finally, the film is reattached. To allow the film/substrate pair to exist in static equilibrium, an equal and opposite traction is applied the edges of the adhered film. The final film/substrate package therefore experiences a moment that causes the film and substrate to adopt a curved shape. (Note that while Figure 1.2 shows a film that shrinks in-plane and therefore develops tensile stresses, an identical thought experiment applies to films that grow in the plane of the film and therefore develop compressive stresses.)

There are several common processes by which a film and its substrate might develop different relaxed dimensions. Deposition processes commonly lead to excess material being present in the film, as when energetic species bombard the growing film during deposition and cause self-interstitial defects by embedding atoms into the film structure. Films also commonly develop smaller equilibrium in-plane dimensions during island coalescence, when the boundaries of neighboring grains zip shut to reduce surface energy at the cost of increased strain energy. The equilibrium in-plane dimensions of a film may change after deposition as well. Differential thermal expansion, when the film and substrate materials have different thermal expansion coefficients and experience temperature changes, is common in thin film processing. Other processes, including grain growth and defect annihilation involve a decrease in film volume, while diffusion of impurities into the film cause an increase in film volume. Phase transformations might cause either an increase or a decrease depending on the phases in question.

1.3 The β-to-α phase transformation in Ta films

Tantalum thin films are used in a variety of technological applications. Tantalum films can be deposited in two polymorphs at room temperature and pressure. α-tantalum is the stable bulk equilibrium phase, which has a bcc structure. α-tantalum has relatively low electrical resistivity

and high ductility. α-tantalum is also nearly immiscible in copper, and is widely used as a diffusion barrier between copper and silicon in microelectronic devices. It forms a passivating oxide which renders α-tantalum films nearly inert, making tantalum a good choice for harsh chemical environments or medical implants. The oxide layer also has good dielectric properties, making α-tantalum an ideal choice for thin film capacitors.

Tantalum can also form a metastable β phase with a complex 30-atom tetragonal unit cell [4]. The β phase is generally found only in thin films, and has a high electrical resistivity and is relatively brittle. β-tantalum has a few technological applications, such as in thin film resistors and thermal inkjet print heads, but the α phase is more widely used. It can be difficult to deposit an α-tantalum film, as the β phase often forms under standard deposition conditions. However, as the β phase is metastable and will spontaneously transform to α at high temperatures, an α-tantalum film can also be formed by depositing in the β phase and thermally cycling to transform the film to α tantalum. Under certain conditions, the α-tantalum films produced by this phase transformation have an unusual microstructure, fully described elsewhere [5,6] and summarized in Section 1.3.1, below.

1.3.1 Orientation gradient microstructure in phase-transformed Ta films

The orientation gradient microstructure, and a normal thin film microstructure, are shown in Figure 1.3.

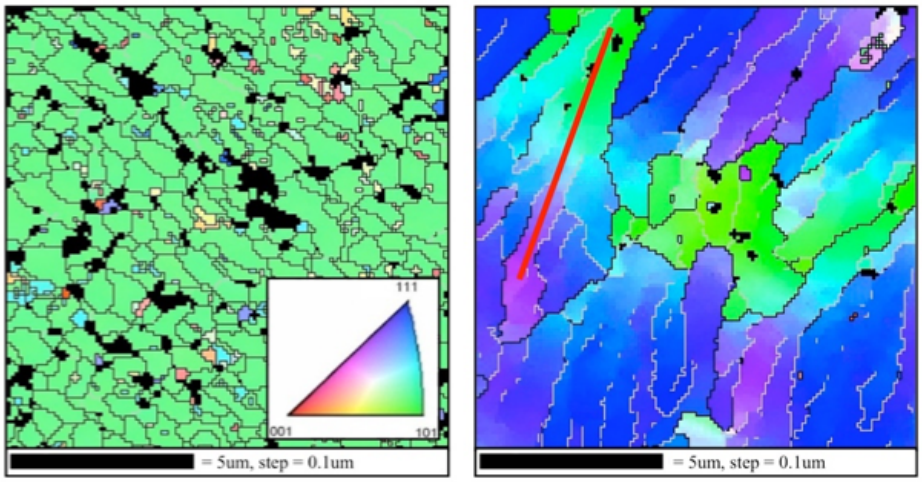

Figure 1.3: EBSD maps of α-Ta films showing (a) normal thin film microstructure and (b) orientation gradient microstructure. From [5].

Both images are electron back-scattered diffraction (EBSD) maps, where color shows the out-of-plane orientation of each pixel according to the stereographic triangle shown in Fig. 1.3a. Black lines correspond to grain boundaries of more than 8º, and grey lines correspond to boundaries between 4 and 8º. Figure 1.3a shows a 400 nm as-deposited α-tantalum film with a normal thin film microstructure, meaning that it has well-defined grains defined by high-angle grain boundaries. Orientation changes occur only across grain boundaries, the mean grain size is comparable to the film thickness, and the film shows strong (101) fiber texture. Figure 1.3b shows the microstructure that results from the phase transformation process described above. Two features distinguish this structure from all known crystalline microstructures. First, the film orientation is not constant throughout each grain. Instead, orientation changes gradually with respect to position, forming continuous orientation gradients throughout the film. Following the red line in Fig. 1.3b, the out-of-plane orientation changes from (101) near the top of the image to (211) near the middle, without crossing a single grain boundary. Second, boundaries are discontinuous: boundaries may begin as high-angle boundaries in one area, then transition to

low-angle boundaries before disappearing altogether. In addition, grains are much larger in this microstructure that in the normal thin film microstructure, though the film is the same thickness as that shown in Fig. 1.3a.

Efforts to understand this microstructure have focused on identifying the geometrically necessary dislocations (GND) that must underlie the structure [5]. The concept of geometrically necessary dislocations is based on work by Nye [7] showing the relationship between unpaired dislocations and lattice plane curvature. This framework allows us to explore the relationship between observed patterns in lattice curvature as measured by EBSD, and the dislocations that must be present. For example, we may consider the rotation shown in Figure 1.3b. Figure 1.4 shows the change in orientation along the red line in Figure 1.3b.

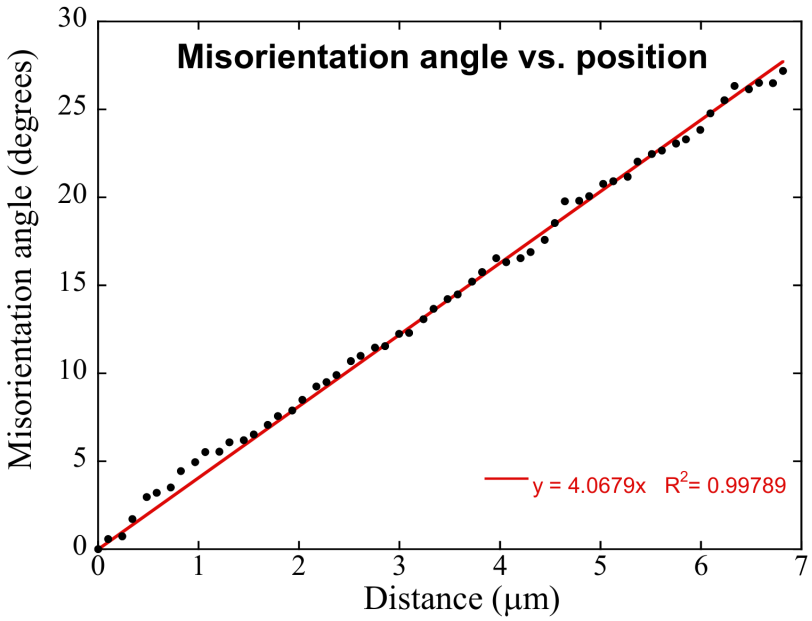

Figure 1.4: Change in misorientation angle with position along red line in Figure 1.5b. From [5].

Change in orientation is represented using misorientation: the angle between the origin of the line at the bottom left and each point along the line is plotted versus the position along the line.

The orientation changes from approximately (110) out of plane to approximately (211) out of plane, rotating at a nearly linear rate of 4°/μm over seven μm. Based on this rate of rotation and the magnitude of the burgers vector for α-Ta, b = 2.863 Å, the geometrically necessary dislocation density along this line is given by:

$$\rho = \frac{\theta}{x} b = 2.4 \times 10^{14}\ m^{-2} \quad (1.1)$$

where θ/x is the magnitude of the rotation and ρ is the minimum dislocation density required to achieve the observed rotation. Of course, this does not include any of the randomly-oriented dislocations that do not contribute to lattice curvature, which are common.

It seems probable that the structure of the initial β film may influence the final structure of the phase-transformed α film, but surprisingly little is actually known about β-Ta films. Any serious attempt to understand how this unusual gradient microstructure forms must therefore begin with an understanding of the β phase itself.

1.3.2 The β phase of Ta

The β phase of tantalum was first described by Mildred H. Read in 1965 [8], and many of the questions raised in this report are still under discussion today. Both α- and β-Ta films were produced by sputtering in 20 mTorr of Ar with a base pressure of 2 x 10^{-6} Torr, and the new phase was observed to have a much higher resistivity than α-Ta (180-220 $\mu\Omega$cm vs. 24-50 $\mu\Omega$cm) and a different crystal structure (an undetermined tetragonal structure vs. bcc). All of the β-Ta films had a prominent fiber texture. However, the nature of the β phase was still unclear. In particular, Read *et al.* could not determine whether β-Ta is a pure allotrope of Ta, or an impurity-stabilized phase.

Later authors argued that β-Ta is not a pure allotrope but is in fact stabilized by oxygen impurities. For example, Westwood et al. [9] deposited Ta films in oxygen-argon atmospheres,

and found that only the β phase is present when the flow of oxygen into the deposition atmosphere is greater than zero—oxygen flow rates as low as 0.05 cm^3/min were sufficient to prevent the formation of the α phase. In a later article [10], he suggests that water vapor may provide the source of this oxygen in many systems, based on mass spectrometry that shows that water vapor added to the chamber during deposition dissociates and is incorporated into growing Ta films as oxygen, and films deposited in oxygen-argon atmospheres are very similar to those deposited in oxygen-water vapor mixtures.

Some, however, find that β-Ta is more likely to appear in clean environments, and that some impurities promote the α phase. Sosniak et al. [11] found that β-Ta films may be deposited in very clean environments with base pressures below 10^{-10} Torr. Schwartz and Feit [12] report that an unidentified impurity present can cause α-Ta to form in systems that normally produce β-Ta, and that when this impurity is removed, the β phase forms. This unknown impurity appeared when new parts were introduced into the deposition system, or when substrates came into contact with various organic substances, including Dextilose paper and a dilute solution of polymer in acetone.

Other researchers have focused on substrates as well. The most thorough of these studies is by Feinstein and Huttemann [13], who studied phase selection on a wide array of different types of substrates. They found that substrates could be divided into three categories depending on whether they produced α or β-Ta. Type 1 substrates, including glass, quartz, ceramic, sapphire, Si, Cu, Ni, and β-Ta, always produce β-Ta. Type 2 substrates, including Au, Pt, Rh, Be and W, always produce α-Ta. Type 3 substrates, including α-Ta, Mo, Si_3N_4, and Ta_2N, normally α-Ta, but could be induced to form β-Ta if the substrate had been treated to produce an oxide layer before deposition. In other words, substrates that form oxides produce β-Ta, and those that

do not produce α-Ta. This indicates that some form of oxygen may be a requirement for the nucleation of β-Ta. This is consistent with the work of Mills [14], who proposed that β-Ta may form by epitaxy on a layer of tetragonal TaO_2 formed during the first few layers of deposition.

However, some researchers have been able to deposit both α and β-Ta on the same substrates, in the same impurity environments, either in successive depositions or in the same film. These authors turn to the characteristics of the depositing atoms to explain their results. Roy et al. [15] deposited Ta films by several different energetic deposition techniques, including bias magnetron sputter deposition, ion-assisted evaporation, pulsed laser deposition, and cathodic arc deposition. They find that the momentum imparted to the growing film per depositing Ta atom is the best parameter to explain their phase selection results. Films deposited with low momentum tend to form with mixed phases, films deposited with moderate momentum for α-Ta, and films deposited with high momentum form β-Ta. A detailed mechanism is not proposed to explain this correlation, but the authors speculate that the momentum dependence they observe may indicate that phase formation involves processes such as forward recoil implantation to create interstitial defects.

A similar effort by Ino et al. [16] focuses on bombarding energy rather than momentum, and adds a second parameter: the flux ratio of Ar ions to depositing Ta atoms. By suing ion-assisted deposition, these authors were able to control energy and ion flux independently, and found that films deposited with both a high ion flux and low energy form α-Ta, while any other combination of these two parameters produces β-Ta. Based on these results, they speculate that β-Ta forms when the growing film does not have enough energy to form the stable α phase, or when energetic deposition causes a sufficient number of defects more easily accommodated by

the β phase. They do not, however, suggest a mechanism by which decreased energy or increased defects might cause the β phase to form.

The overall picture that forms in examining the literature on β-Ta is one of confusion. There is no consensus on the conditions in which β-Ta appears, or the mechanisms by which it forms. Its properties are known in general terms—"high" resistivity, "low" ductility, etc.—but with very little precision. By performing a careful study of β-Ta films deposited under identical low-oxygen conditions and varying only the Ar sputter pressure, we attempt to clarify these issues. In Chapter 3, we show that β-Ta may be deposited over a wide range of deposition energies and in a virtually oxygen-free atmosphere. While stresses and texture change systematically with sputter pressure, the phase remains constant, and our understanding of these effects allow us to propose a mechanism to explain the formation of β-Ta that is consistent with nearly all published results to date. In Chapter 4, we measure properties of these films and report, for the first time, representative values for resistivity and the Hall-Petch constant.

With this understanding of β-Ta in place, we may return to the phase transformation and the unusual microstructure that results. In order to see a complete picture of this orientation gradient microstructure, it is necessary to understand the full range of variation possible when transforming from the β phase to the α phase, as any repeating patterns may indicate important underlying features of the microstructure, and may help to show how it forms. We have already created a series of β-Ta films with systematic variations in microstructure, described in Chapters 3 and 4. A natural question, therefore, is whether this systematic variation in β-Ta microstructure will lead to a corresponding variation in the phase-transformed α-Ta microstructure, and if so, what that variation might tell us about how the gradient microstructure forms.

This question is answered in Chapters 5 and 6, in which we anneal the series of β-Ta films described in Chapters 3 and 4 to transform them to the alpha phase and examine the resulting microstructures. In Chapter 5, we show that the annealed films all show the orientation gradient microstructure described in Section 1.3.1, and the variation in initial β microstructure leads to prominent differences in the morphology of the phase-transformed α-Ta microstructure. While the magnitude and lengths of the gradients depend on initial microstructure, certain similarities between all of the phase-transformed microstructures, allow us to propose a simple rotation mechanism by which the orientation gradients might form. In Chapter 6, we focus on recurring element of the phase-transformed microstructure, and analyze the dislocations needed to produce it using a genetic algorithm.

1.4 The (111)-to-(100) texture transformation in FCC thin films

Face-centered cubic films are used in a variety of applications, including the use of copper for metallization in microelectronics. Many deposition processes used to produce FCC films result in films with a (111) fiber texture—films composed of grains with their (111) planes parallel to the substrate and randomly-oriented in the plane of the film. This structure is not always stable, however: there is a well-known thickness-dependent transformation that often occurs when these films are annealed. If the film is below some critical thickness, the film retains its (111) texture. If, however, the film is above this critical thickness, the film transforms to a (100) fiber texture. This has important implications for FCC film applications, as film properties often depend strongly on texture.

The (111)-to-(100) texture transformation is often attributed to a competition between surface energy and strain energy [17]. The argument is based on the fact that the (111) face in FCC materials usually has a lower surface energy than the (100) face, while the biaxial modulus

of a (100)-textured film is usually lower than that of a (111)-textured film. As the film gets thicker, the interface energy plays a smaller role, and, assuming the equal biaxial strain remains constant, strain energy plays a larger role. According to this model, the critical stress at which the film should transform to the (100) texture is a function of film thickness, given by:

$$\sigma_{111,min} = \sqrt{\frac{2}{h_c}(\gamma_{100} - \gamma_{111})\frac{Y_{111}^2}{(Y_{111} - Y_{100})}} \quad (1.2)$$

where σ_{111} is the magnitude of the equal biaxial stress in the film, h_c is the film thickness, γ_{111} and γ_{100} are the surface energies of the (111)- and (100)-oriented films, and Y_{111} and Y_{100} are the biaxial moduli of the (111)- and (100)-oriented films.

This model provides an appealingly simple explanation for the texture transformation phenomenon, and has been widely cited [17–20]. However, there is surprisingly little experimental evidence for the role of interface and strain energies in this transformation. Vanstreels et al. [21] measured stresses in Cu films and found the transformations in these films to be consistent with the interface strain energy model. Others, however, have found conflicting evidence. Greiser et al. [22,23] observed the (111)-to-(100) texture transformation in Ag films on a variety of substrates, but the critical thickness required for transformation did not depend on the substrate material, which calls into question the role of interface energy in the transformation. Furthermore, a film removed from its substrate still transformed to a (100) texture, despite the complete absence of substrate interaction stress. Sonnweber-Ribic et al. [24] observed a texture transformation in Cu films, but stresses measured by XRD using $\sin^2\psi$ analysis revealed that the strain energy in the films were inadequate to cause the transformation according to the interface/strain energy model. Similarly, Baker et al. [25] observed the texture transformation in Ag films, but found that the presence of a Ti interlayer had no effect on the critical thickness

despite a clear influence on interface energy, and that measured stresses were too low to drive the transformation, according to the model, as shown below.

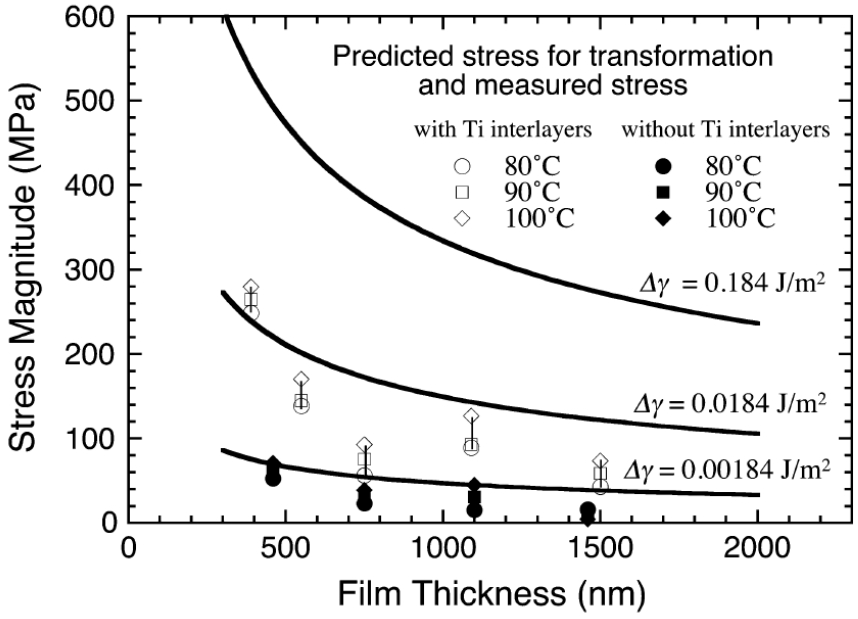

Figure 1.5: Measured stresses in Ag films, plotted with critical transformation stress levels according to the interface/strain energy model. From [25].

Figure 1.5 shows the measured values of the magnitude of the equal biaxial stress in several Ag films, alongside the critical transformation stress given by Equation 1.2. Because the interface energy of the (111) and (100) orientations are not well known, critical stress is calculated for the reported difference in interface energies [26], as well as for differences one and two orders of magnitude smaller than reported. At the reported value, the model predicts that none of the films should transform. However, even for the smallest interface energy difference, the model cannot accurately predict which films transform. Instead of predicting that thick films should transform and thin films retain (111) texture, the model suggests that the thinnest films should transform.

The interface/strain energy model also fails to explain an interesting feature of the morphology of the transformed films: the transformed films often feature abnormally large and irregularly shaped (100) grains. An example from Greiser et al. [22] is shown below.

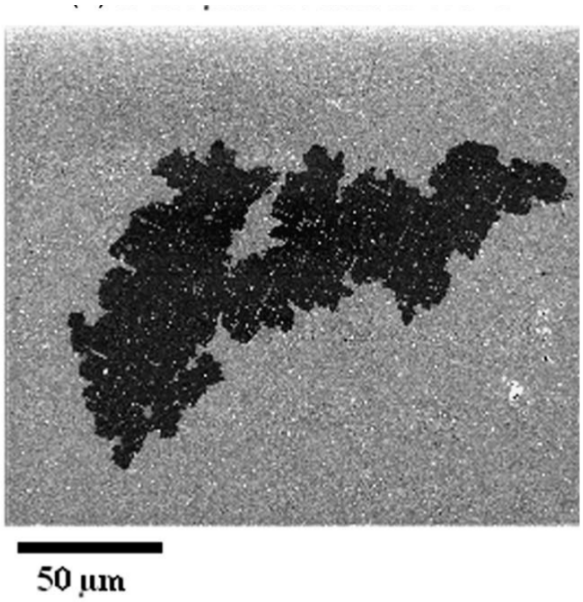

Figure 1.6: Plan-view FIB image of abnormal (100) grain in a Cu film. From [22].

Figure 1.6 shows a single giant (100) grain growing in a matrix of small (111)-oriented grains in a 2.4 μm thick Cu film. The length of the giant grain is more than 60 times the film thickness, and its boundary has a meandering appearance.

The failure of the established interface/strain energy model to explain the (111)-to-(100) texture transformation in FCC films indicates that more work is required to understand the driving forces at work. If neither strain energy nor interface energy can explain the texture transformation, some other source of energy must provide the necessary driving force. Defect energy is an obvious choice, and in Chapter 7 of this thesis we present a thorough investigation into the various forms of defects present in thin FCC films that might provide enough energy to drive the texture transformation. We begin by imposing different strain energies on otherwise identical films using a bulge test, and confirm that changing strain energy has no effect on the transformation. We then examine point defects, line defects, and planar defects as sources of defect energy, and propose a possible mechanism by which the (100) texture might be selected.

1.5 Structure of this thesis

This thesis is organized into eight chapters. Chapter 1 introduces basic thin film concepts as well as the two transformations discussed in this thesis, and Chapter 2 describes some of the experimental methods used in this work.

Chapters 3 and 4 present a series of β-Ta films deposited under various sputter pressures, and remark on phase selection, microstructure, and properties in β-Ta. Chapter 3 focuses on phase selection, stresses, and texture in β-Ta, and proposes a new theory explaining the formation of the β phase. Chapter 4 explores the resistivity, mechanical properties, and morphology of these films.

Chapters 5 and 6 explore these same films after they have undergone a transformation to the stable α-Ta phase, Chapter 5 discusses the unusual orientation gradient microstructure that results, and develops a simple model for how such patterns might form. Chapter 6 calculates the dislocation arrays necessary to form these gradient patterns according to this model. Chapters 5 and 6 are based on award-winning undergraduate and masters work by Marissa Linne and Ari Kestenbaum and advised by me.

Chapter 7 explores the (111)-to-(100) texture transformation in FCC films, and presents the results of a bulge test experiment designed to identify and quantify the relevant driving forces for this transformation.

Finally, Chapter 8 provides a summary and suggestions for future work on each of these topics.

1.6 References

[1] B.A. Movchan, A. V Demchishin, L.D. Kooluck, Structure and mechanical properties of thick Fe , Fe – NbC , Fe – Ni – NbC condensates, J. Vac. Sci. Technol. 869 (1974). doi:10.1116/1.1318081.

[2] J.A. Thornton, High rate thick film growth, Annu. Rev. Mater. Sci. 7 (1977) 239–260. doi:10.1146/annurev.ms.07.080177.001323.

[3] M.F. Doerner, W.D. Nix, Stresses and deformation processes in thin films on substrates, Crit. Rev. Solid State Mater. Sci. 14 (1988) 225–268. doi:10.1080/10408438808243734.

[4] A. Arakcheeva, C. Gervais, V. Grinevitch, The self-hosting structure of b -Ta, Acta Crystallogr. Sect. B. B58 (2002) 1–7.

[5] R.A. Knepper, Thermomechanical behavior and microstructure evolution of tantalum thin films during the beta-alpha phase transformation, Cornell University, 2007.

[6] S.P. Baker, In progress, (2018).

[7] J.F. Nye, Some Geometrical Relations in Dislocated Crystals, Acta Metall. 1 (1953) 153–162.

[8] M.H. Read, C. Altman, A new structure in tantalum thin films, Appl. Phys. Lett. (1965).

[9] W.D. Westwood, N. Waterhouse, Structural and Electrical Properties of Tantalum Films Sputtered in Oxygen-Argon Mixtures, J. Appl. Phys. 42 (1971) 2946–2952.

[10] W.D. Westwood, D.J. Willmott, P.S. Wilcox, Tantalum Films Triode-Sputtered in Mixtures of Argon and Water Vapor, J. Vac. Sci. Technol. 9 (1972) 987. doi:10.1116/1.1317843.

[11] J. Sosniak, W.J. Polito, G.A. Rozgonyi, Effect of Background-Gas Impurities on the Formation of Sputtered β-Tantalum Films, J. Appl. Phys. (1967). doi:10.1063/1.1710059.

[12] N. Schwartz, E.D. Feit, Impurity Effects in the Nucleation of Alpha (bcc)-Tantalum or Beta-Tantalum Films, J. Electrochem. Soc. (1977).

[13] L.G. Feinstein, R.D. Huttemann, Factors controlling the structure of sputtered Ta films, Thin Solid Films. 16 (1973) 129–145.

[14] D. Mills, The Structure of Sputtered Tantalum, J. Can. Ceram. Soc. 35 (1966) 48.

[15] P. Catania, R.A. Roy, J.J. Cuomo, Phase formation and microstructure changes in tantalum thin films induced by bias sputtering, J. Appl. Phys. 74 (1993) 1008–1014.

[16] K. Ino, T. Shinohara, T. Ushiki, T. Ohmi, Ion energy , ion flux , and ion species effects on crystallographic and electrical properties of sputter-deposited Ta thin films, J. Vac. Sci. Technol. A. 15 (1997) 2627–2635.

[17] C. V Thompson, Structure Evolution During Processing of Polycrystalline Films, Annu. Rev. Mater. Sci. 30 (2000) 159–90.

[18] J.A. Floro, C. V Thompson, R. Carel, P.D. Bristowe, Competition between strain and interface energy during epitacial grain growth in Ag films on Ni(001), J. Mater. Res. 9 (1994) 2411.

[19] E.M. Zielinski, R.P. Vinci, J.C. Bravman, Effects of barrier layer and annealing on abnormal grain growth in copper thin films, J. Appl. Phys. 76 (1994) 4516. doi:10.1063/1.357283.

[20] C.V. Thompson, R. Carel, Texture development in polycrystalline thin films, Mater. Sci. Eng. B. 32 (1995) 211–219. doi:10.1016/0921-5107(95)03011-5.

[21] K. Vanstreels, S.H. Brongersma, Z. Tokei, L. Carbonell, W. De Ceuninck, J. D'Haen, M. D'Olieslaeger, Increasing the mean grain size in copper films and features, J. Mater. Res. 23 (2008) 642–662. doi:10.1557/JMR.2008.0080.

[22] J. Greiser, D. Müller, P. Müllner, C.. Thompson, E. Arzt, Growth of giant grains in silver thin films, Scr. Mater. 41 (1999) 709–714. doi:10.1016/S1359-6462(99)00205-5.

[23] J. Greiser, P. Mullner, E. Artzt, ABNORMAL GROWTH OF "GIANT" GRAINS IN SILVER THIN FILMS, Acta Mater. 49 (2001) 1041–1050.

[24] P. Sonnweber-Ribic, P. a. Gruber, G. Dehm, H.P. Strunk, E. Arzt, Kinetics and driving forces of abnormal grain growth in thin Cu films, Acta Mater. 60 (2012) 2397–2406. doi:10.1016/j.actamat.2011.12.030.

[25] S.P. Baker, B. Hoffman, L. Timian, A. Silvernail, E. a. Ellis, Texture transformations in Ag thin films, Acta Mater. 61 (2013) 7121–7132. doi:10.1016/j.actamat.2013.07.061.

[26] M.I. Baskes, Modified embedded-atom potentials for cubic materials and impurities, Phys. Rev. B. 46 (1992) 2727–2742. doi:10.1103/PhysRevB.46.2727.

CHAPTER 2

Experimental Details

This chapter contains details of the experimental methods used in this thesis not included in chapters 3-6. Film deposition is discussed in sections 2.1 and 2.2, and characterization is discussed in sections 2.3 and 2.4.

2.1 High-vacuum evaporation system

The silver films discussed in Chapter 7 of this thesis were deposited in a high-vacuum evaporation system with typical base pressures of 10^{-6} Torr. The evaporation system consists of a single bell jar pumped with rotary vane rough pumps and a cryogenic pump. Film material was vaporized using e-beam evaporation from a water-cooled hearth with space for five crucibles, and substrates were mounted over the hearth to prevent particles from landing on the film. Film thickness was measured during deposition using a vibrating crystal rate monitor, and confirmed after deposition using contact profilometry. The evaporation system also features a computer-controlled linear shutter that can be used to create films with gradients in thickness, allowing for high-throughput measurements of films with many different thicknesses made during a single deposition run. The linear shutter is programmed to move during film deposition, gradually covering more of the substrate so that some areas of the substrate are exposed to the flux of depositing material for much longer times than others. These films therefore have coatings of different thicknesses, but were deposited under identical conditions, allowing for accurate comparisons between different films. The high-throughput process is described more fully in [1].

2.2 Ultra-high vacuum sputter deposition system

The tantalum films discussed in Chapters 3-6 were deposited in a custom-made multi-stage system. A schematic of the system is shown in Figure 2.1.

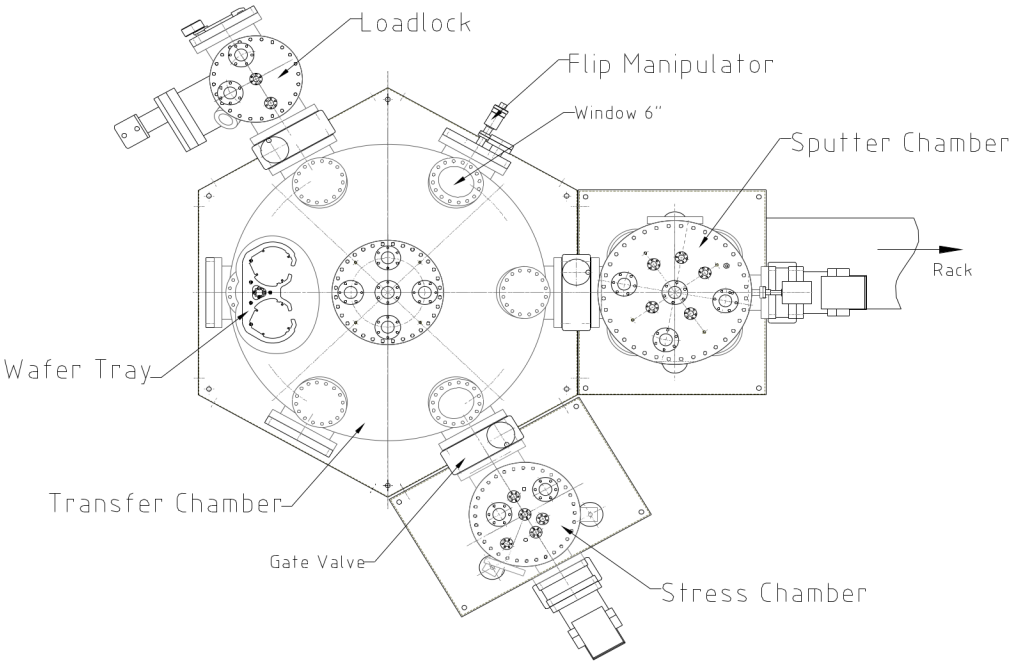

Figure 2.1: Schematic of UHV deposition system used in Chapters 3-6. From [2].

The deposition system consists of four chambers. Substrates are inserted into the system through the load/lock chamber, films are deposited in the sputter chamber, and thermal cycles are performed in the stress chamber. The transfer chamber permits movement between these three chambers without breaking vacuum. The load/lock chamber operates at high vacuum, while the remaining three chambers operate at ultra-high vacuum with typical base pressures of 10^{-9} Torr. The sputter chamber features three water-cooled magnetron sputter guns oriented 23° from vertical, confocal on the wafer holder, to allow for co-sputtering of different materials. The substrate is held above the sputtering guns to avoid large particles falling onto the film surface,

and, in the following experiments, is rotated at 5 rpm during deposition to promote even film thickness. The substrate is not heated but temperature is monitored during film growth.

The stress chamber contains a vacuum furnace and has a window in the bottom of the chamber. Wafer curvature is measured using a custom system by directing the beam of a laser through this window and recording reflections from the wafer in two dimensions. The films discussed in Chapter 6 are annealed in the stress chamber as well, and curvature is measured continually as temperature is increased to 700°C at a rate of 10°C/min. To improve heat transfer between the sample, the heater, and the chamber walls, the stress chamber is filled to 1 Torr with ultrahigh-purity He gas additionally filtered to reduce oxygen contamination levels to below 1 ppb. The sample rests on a water-cooled Cu block with a three-point support to allow the substrate to deflect freely.

Average biaxial film stress is determined from wafer curvature measurements using the Stoney relation [3]:

$$K = \frac{1}{R} = \frac{6\sigma_f t_f}{Y_s t_s^2}, \text{ or} \tag{2.1}$$

$$\sigma_f = \frac{Y_s t_s^2}{6 t^f R} \tag{2.2}$$

where K is the curvature of the film/substrate pair, R is the radius of curvature of the film/substrate pair, σ_f is the magnitude of the equal biaxial film stress, t_f is the film thickness, Y_s is the biaxial modulus of the substrate, and t_s is the thickness of the substrate. Conveniently, Equations 2.1 and 2.2 require no foreknowledge of the properties of the film, only those of the substrate, allowing us to measure stresses in films about which little is known.

The UHV sputter system used in these experiments is ideal for tantalum deposition, where contamination with reactive gases is common and has a dramatic effect on structure and properties. Deposition in environments with even small amounts of oxygen can affect the phase,

mechanical properties, and resistivity of Ta films, as we discuss in Chapters 3-4. By depositing in a UHV environment with additional oxygen filtration, we are able to assess the properties of virtually oxygen-free β-Ta. Oxygen also affects the phase transformation from β to α—even the thin native oxide layer that forms on exposure to atmosphere is enough to alter the transformation behavior [4]— so the ability to anneal films *in situ*, without exposing them to oxygen between deposition and thermal cycling, is critical to examining the microstructure of phase-transformed films in Chapters 5 and 6.

2.3 G2 Experimental Station at the Cornell High Energy Synchrotron Source (CHESS)

The texture measurements described in Chapter 7 were performed in the G2 hutch at the Cornell High-Energy Synchrotron Source (CHESS). The G2 hutch is equipped with a custom-built 6-circle κ diffractometer [5], shown in Figure 2.2.

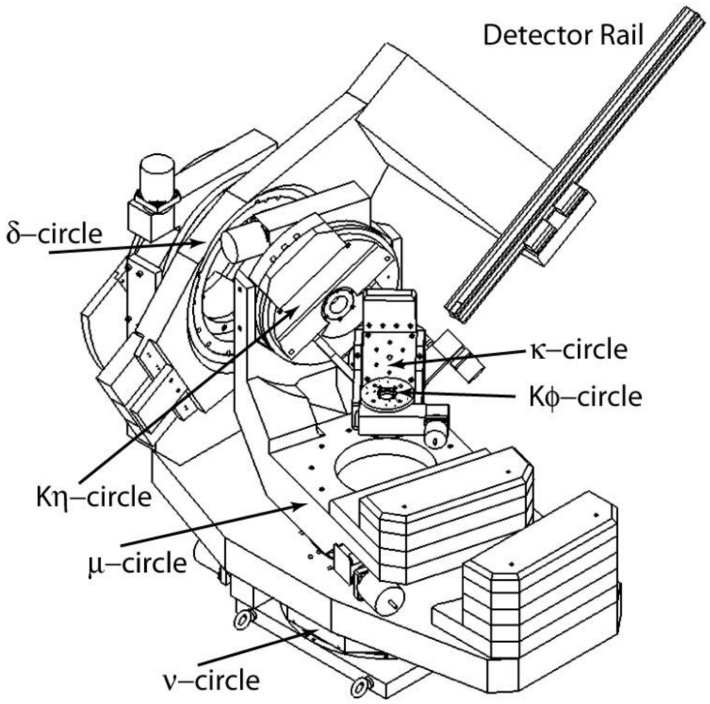

Figure 2.2: Schematic of 6-circle κ diffractometer, from [5].

The G2 station shares a high-energy x-ray beam with the G3 station next door, with a range of incident beam energies from 8 to 16 keV. A Be crystal monochromator diffracts the beam into the G2 station. The diffractometer system consists of the diffractometer, sample stage, area detector, and line detector. The 6-circle κ diffractometer design allows access to all scattering vectors above the sample horizon and allows for both horizontal and vertical diffraction geometries. Rotation stages are counterbalanced with lead weights to reduce sample displacements. The motorized sample stage can also correct for position errors caused by thermal expansion. The system is equipped with both an area detector and a line detector.

For the work described in Chapter 7, we used a custom-built bulge test apparatus mounted on the 6-circle κ diffractometer. For more information about the bulge test apparatus, see Chapter 7.

2.4 Electron Backscatter Diffraction

Electron backscatter diffraction (EBSD) is a technique used to capture spatially-resolved structure and orientation information using a scanning electron microscope and CCD camera. The sample is placed in the SEM and oriented at 70° from vertical. The electron beam illuminates the sample and scatters off of both the top and bottom of lattice planes, producing two diffraction cones from each set of lattice planes. These cones intersect the screen of the camera, producing two nearly parallel lines, called Kikuchi lines. Lattice planes may be identified by the spacing between the Kikuchi lines associated with that plane, and the crystallographic orientation of the sample may be determined by examining the pattern of all of the Kikuchi lines visible on the screen, called the Kikuchi pattern. A sample Kikuchi pattern is shown in Figure 2.3.

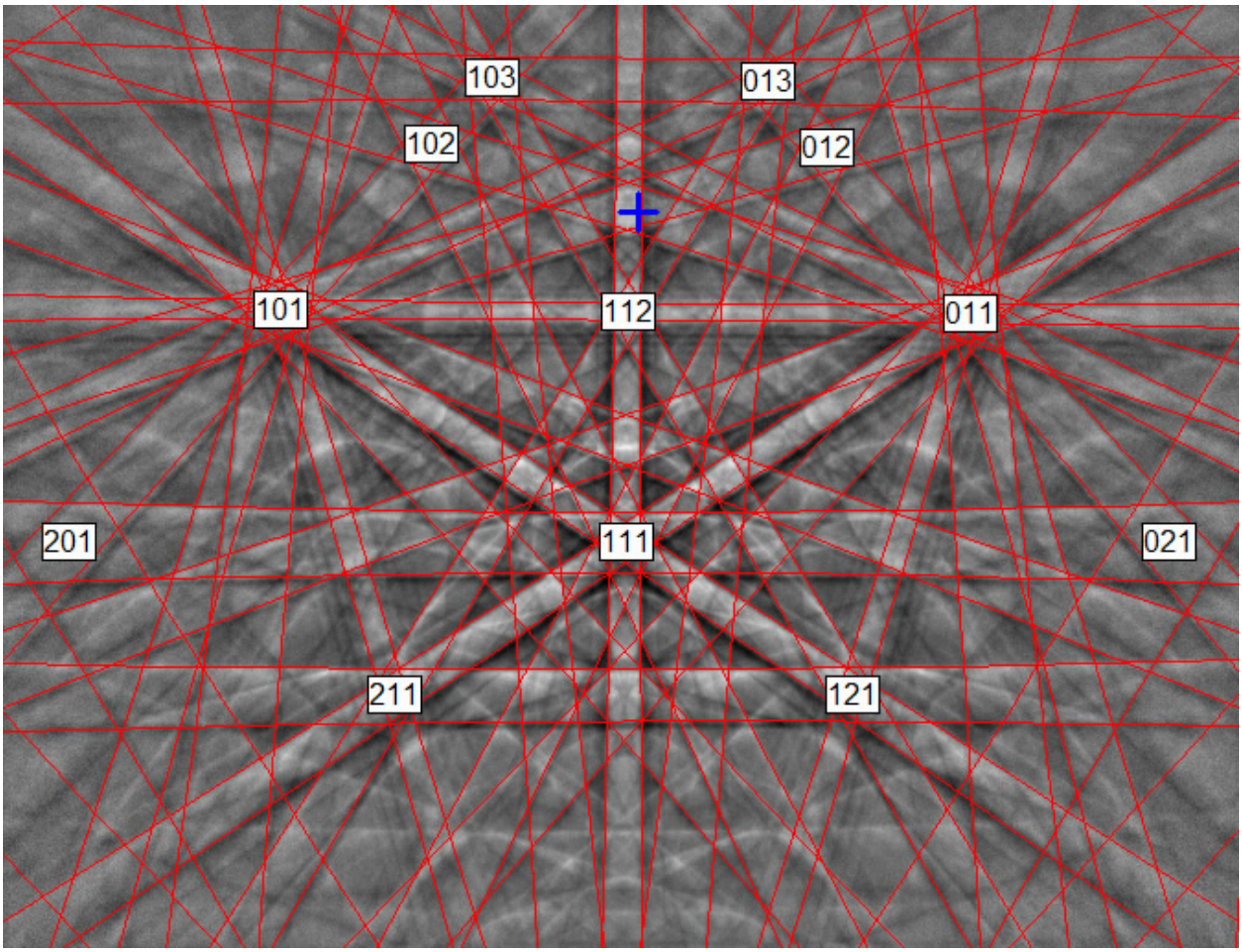

Figure 2.3: Indexed Kikuchi pattern, with Kikuchi lines identified in red and the pattern center identified by a blue cross. Zone axes are labeled. From [6].

Indexing is performed by transforming the Kikuchi pattern image to Hough space, where Kikuchi lines appear as peaks and are easier for the computer to detect. The angles between bands are then compared with known values of interplanar angles for the structure in question, and the most consistent indexing solution is saved. The electron beam is then moved to a new position so that the entire region of interest may be mapped. The software associated with our EBSD system (HKL CHANNEL 5) can perform many analyses of the resulting orientation data, including finding grain boundaries and twin boundaries, generating pole figures and inverse pole figures, and identifying different phases. Orientation data may also be exported for use in other analyses, as in Chapter 6.

2.5 References

[1] S.P. Baker, B. Hoffman, L. Timian, A. Silvernail, E. a. Ellis, Texture transformations in Ag thin films, Acta Mater. 61 (2013) 7121–7132. doi:10.1016/j.actamat.2013.07.061.

[2] R.A. Knepper, Thermomechanical behavior and microstructure evolution of tantalum thin films during the beta-alpha phase transformation, Cornell University, 2007.

[3] G.G. Stoney, The tension of metallic films deposited by electrolysis, Proc. R. Soc. London, Ser. A. 82 (1909) 172–175.

[4] R. Knepper, B. Stevens, S.P. Baker, Effect of oxygen on the thermomechanical behavior of tantalum thin films during the β–α phase transformation, J. Appl. Phys. (2006). doi:10.1063/1.2388742.

[5] D.E. Nowak, D.R. Blasini, a. M. Vodnick, B. Blank, M.W. Tate, a. Deyhim, D.-M. Smilgies, H. Abruña, S.M. Gruner, S.P. Baker, Six-circle diffractometer with atmosphere- and temperature-controlled sample stage and area and line detectors for use in the G2 experimental station at CHESS, Rev. Sci. Instrum. 77 (2006) 113301. doi:10.1063/1.2372730.

[6] EBSD Explained, Oxford Instruments. (2018).

CHAPTER 3

Effect of sputter pressure on Ta thin films: Beta phase formation, texture, and stresses

Elizabeth A. I. Ellis[1], Markus Chmielus[1,2], and Shefford P. Baker[1]

1. *Cornell University, Department of Materials Science and Engineering, Bard Hall, Ithaca, NY 14853 USA*
2. *University of Pittsburgh, Department of Mechanical Engineering & Materials Science, Benedum Hall, Pittsburgh, PA 15261 USA*

This chapter will appear in Acta Materialia, Vol. 150, pp. 317-326. My role in the work was in helping to deposit the films and perform stress and XRD measurements, performing energy calculations, and formulating the phase selection mechanism.

ABSTRACT

The metastable tetragonal beta phase of tantalum can be made in thin film form by sputter deposition and has very different properties from the stable BCC alpha phase. Both phases are important in thin film technologies. However, despite fifty years of study, the mechanism of phase selection remains unknown. To evaluate the role of energetic deposition, we prepared a series of films under varying Ar sputter pressures. Measurements of film stress as a function of sputter gas pressure allow us to unambiguously index diffraction peaks to determine phase and texture. This peak indexing allows us to confirm that β-Ta has a distorted Frank-Kasper sigma structure (P-42_1m), rather than the β-U structure ($P4_2$/mnm) that is usually assumed. We find only the beta phase in our films in the form of a dominant (002) β-Ta fiber component that becomes broader as the pressure increases. Based on calculations of the energy of incident Ta atoms and Ar neutrals, we show that resputtering could account for the changes in texture distribution. By comparing these results with a detailed review of the literature, we are able to

propose a phase selection mechanism that is consistent with the vast majority of published results, namely that β-Ta grows epitaxially on a TaO_x layer, possibly TaO_2, that forms during the initial phase of deposition. Oxygen is not required in the growing film to maintain the beta structure.

3.1. INTRODUCTION

For most of the fifty years since its discovery [1], the metastable β phase in tantalum thin films has been treated primarily as a nuisance (see, *e.g.* [2–10]). The stable α phase is widely used in thin film form; for example, as a diffusion barrier for Cu interconnects due to its low resistivity and insolubility with Cu, and as wear- and corrosion-resistant coatings due to its high ductility and passivating oxide. In contrast, the only significant technological application of the β phase has been in thin film resistors, thanks to its high resistivity and low temperature coefficient of resistivity. Accordingly, the majority of research on phase formation in Ta films has, to date, focused on obtaining the stable α phase [2,3,5,7–9,11–14]. However, discovery of a giant spin Hall effect in β-Ta, which may enable development of a new generation of magnetoresistive random access memory technologies, has revived significant interest in this phase (*e.g.* see citations to Liu *et al.* [15]).

In light of these different applications, an ability to understand and control phase formation and properties in sputtered β-Ta films is needed. However, a consensus on the conditions under which β-Ta forms, and the mechanism by which it forms, has yet to emerge. Indeed, studies of phase formation in Ta films have produced many contradictory results. We have conducted a careful review of the literature and have identified several parameters that have been reported to be important in phase selection: substrate temperature, substrate crystal structure and composition (including impurities), impurities in the sputter gas, and the energies of the species impinging on the substrate. Of these, only the effect of substrate temperature is well known: α-

Ta forms readily when deposited at high temperatures [16–18], although the temperatures required have been reported to be as low as 300˚C [18] and as high as 800˚C [17].

The substrate on which Ta is deposited is said to affect the phase that appears [19–21]. Substrates such as Nb [22,23] and Ti [3] can promote α-Ta via epitaxial growth. Ta deposited on oxides and readily-oxidized materials usually forms beta, while Ta deposited on oxide-free materials usually forms alpha [19,20,24]. Impurities may also be important, although unifying trends have not been reported. For example, α-Ta can be promoted by either preheating a substrate to remove adsorbed water [16,25], or by deliberately adding organic impurity layers [26].

The effect of impurities in the sputter gas environment has also been investigated. Some researchers concluded that oxygen in the sputter gas is required to form β-Ta [19,20]; indeed it has been suggested that β-Ta is an impurity-stabilized phase that forms when the oxygen concentration exceeds the solubility limit in α-Ta [25,27,28]. However, there is at least one report of β-Ta on oxide-free substrates in a nominally oxygen-free environment [21], while some claim that adding oxygen to the sputtering gas actually promotes α-Ta growth [29–31]. Nitrogen in the sputtering gas is associated with the formation of α-Ta [3,17,25,31,32], but the presence of unknown gas impurities, either from worse vacuum [33] or failing to presputter [16], has been said to promote the beta phase.

Still others have focused on incident particle energy during film growth, including variations in sputter power [33], bias voltage [7], sputter gas species [2], sputtering type (RF [7], HiPIMS [9], *etc.*), and sputter gas pressure [4]. It might be expected that α-Ta would form in higher-energy environments since it is the equilibrium phase, and some researchers do observe this [9,34,35]. However, others observe a "window"-like behavior, where films sputtered within some range of energies form α-Ta and those with either higher or lower energies form β-Ta [2,4,7,8,33,36]. The kinetic energy of the bombarding particles [33,37] and the particle momentum [8] have both been proposed as parameters that control phase selection. One study

claimed that both low bombarding energy and a high flux of Ar^+ ions are required for the formation of α-Ta during ion-assisted deposition [2].

Despite these efforts, no unifying theory that can explain phase selection in sputtered Ta films has been proposed. Furthermore, relatively little is known about the microstructure and properties of the β-Ta films that are produced. Indeed, even the crystal structure of β-Ta is not well established. A structure proposed in 1973 with space group $P4_2/mnm$ [38] is still widely cited, though recent work [6] suggests that a structure proposed in 2002, with space group $P\text{-}42_1m$ [39] is more likely.

The working gas pressure and substrate temperature are often considered to be the primary process variables in sputter deposition [40]. Since the effects of temperature on phase formation in Ta films have been explored [16,18,25], we investigated the effects of varying Ar sputter gas pressure, p_{Ar}, while holding temperature (and all other variables) constant and minimizing the effects of impurities arising from the base pressure gas, the sputter gas, the substrate surface, and the target. Under these conditions, p_{Ar} strongly affects the film stress and texture. However, unlike in previous studies [4,33,34,41–43], it does *not* affect phase formation—only β-Ta is seen. We show how p_{Ar} determines stresses and how understanding the stresses allows us to unambiguously interpret the phase, crystal structure, and texture. Understanding the texture, in turn, allows us to propose a model for β-Ta phase formation that accounts for virtually all previously published observations.

3.2. EXPERIMENTS

Tantalum thin films were prepared by DC magnetron sputter deposition in an ultra-high vacuum (UHV) system [44] with a base pressure of 2.7×10^{-6} Pa (2×10^{-8} Torr) or lower, taking steps to minimize impurities that might affect phase formation. The deposition system comprises separate load-lock, transfer, deposition, and stress-measurement chambers. Substrates were (001) Si with a diameter of 100 mm and thickness of 525 μm with a native oxide layer. As-received substrates

were handled minimally by the edges using only clean tools. No chemical cleaning steps, which have been reported to leave residues that affect phase formation [26], were used.

Substrates were installed into the UHV system via the load lock and stored in the transfer chamber at 2.7×10^{-6} Pa (2×10^{-8} Torr) or lower until needed. Each substrate was transferred to the deposition chamber and plasma cleaned for 1 min using a 25 W RF bias in 1.1 Pa Ar to remove adsorbed water or other impurities before deposition. Immediately after cleaning, the working gas pressure was adjusted to the desired setting and Ta was presputtered onto a closed shutter from a 99.95% pure 75 mm diameter Ta target for 5 min using a magnetron gun operated in DC mode at 400 W to clean the target. Without interruption, the shutter was opened so that Ta was sputtered onto the substrate to a nominal thickness of 500–600 nm at the same settings.

The key deposition variable was the Ar working gas pressure, p_{Ar}. Seven Ta thin films were prepared at p_{Ar} = 0.3, 0.5, 1.1, 1.6, 1.9, 2.0, and 2.2 Pa (2, 4, 8, 12, 14, 15, and 16 mTorr). To minimize impurities, the ultra-high purity (UHP) Ar (99.999%) that was used for both plasma cleaning and deposition was filtered using an indicating oxygen trap to remove oxygen and other contaminants, resulting in less than 1 ppb oxygen in the process gas. The Ta deposition rate was approximately 0.65 ± 0.1 nm/sec, independent of p_{Ar} and the substrate temperature increased to a maximum of ~90°C during deposition for all samples as measured by a thermocouple on the back of the substrate. The sputter gun was oriented 23° from the substrate normal at an average distance of 125 mm. The substrate was grounded and rotated at 5 rpm during deposition.

Film stresses were determined by measuring the curvature of the substrates before and after film deposition using a custom curvature measurement system in a different chamber in the same UHV vacuum environment, without breaking vacuum [44]. The Stoney relation [45] was used to determine the stress in each film from the change in curvature.

Following stress measurement, the substrates with films attached were cleaved into 1 × 1 cm square samples for further analysis. Sample thicknesses were obtained from cross-section images of the cleaved edges using scanning electron microscopy (SEM). For samples produced with p_{Ar} = 0.3, 0.5, and 1.1 Pa, thicknesses were also determined to within 5 nm using Rutherford

backscattered diffraction (RBS) and the RUMP analysis and simulation software. These samples were used to calibrate the thicknesses measured using SEM.

The crystal structure and texture in the Ta films were evaluated using x-ray diffraction (XRD) on a piece from the center of the substrate for each sample. Symmetric θ-2θ scans were completed using a Cu K_α source operated at 40 kV and 44 mA. For these scans, the scattering vector was set 1° off the film normal to avoid the majority of the strong (400) peak from the Si (100) substrate at $2\theta = 69.13^\circ$, which is close to the (004) β-Ta (70.89°) and (211) α-Ta (69.61°) peaks. Rocking curves were obtained using the ω geometry [46] by setting the 2θ angle to the measured maximum of the (002) β-Ta peak and scanning the scattering vector from –15° to +15° from the film normal. In-plane texture was investigated using a general area detector diffraction system (GADDS) by recording the (311) diffraction cones from the (002) β-Ta grains at 5 random in-plane (azimuthal) angles between 0° and 90°.

3.3. RESULTS & ANALYSIS

3.3.1. Stress

Figure 3.1 shows the equal-biaxial in-plane stress as well as the position of the (002) β-Ta peak *vs*. sputter pressure for all samples.

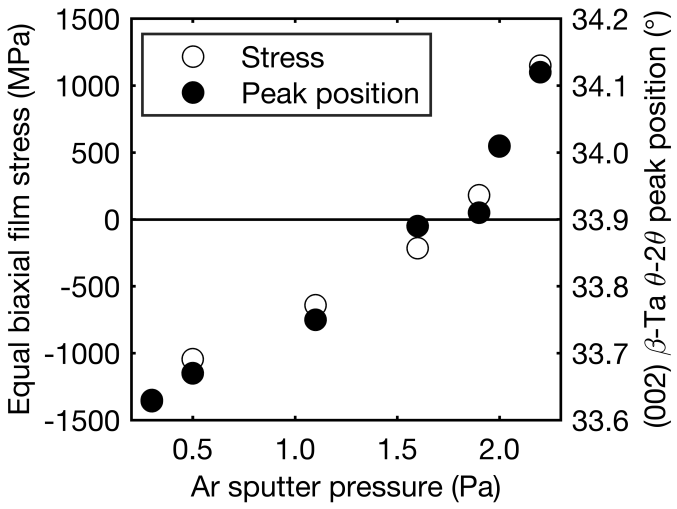

Figure 3.1: Equal biaxial in-plane stress determined from substrate curvature and position of (002) XRD peaks in as-deposited Ta films as a function of argon sputter gas pressure. Stresses go from strongly compressive to strongly tensile over the pressure range and peak shifts are consistent with measured film stresses.

The stress changes dramatically across the range, from strongly compressive (-1360 MPa at 0.3 Pa) to strongly tensile (1140 MPa at 2.2 Pa), and the peak shifts are consistent with the measured stresses.

3.3.2. Phase Analysis

XRD measurements (Figure 3.2) revealed that all films show only β-Ta peaks and have (002) texture. Fig. 3.2a shows θ-2θ scans at the same scale for all films.

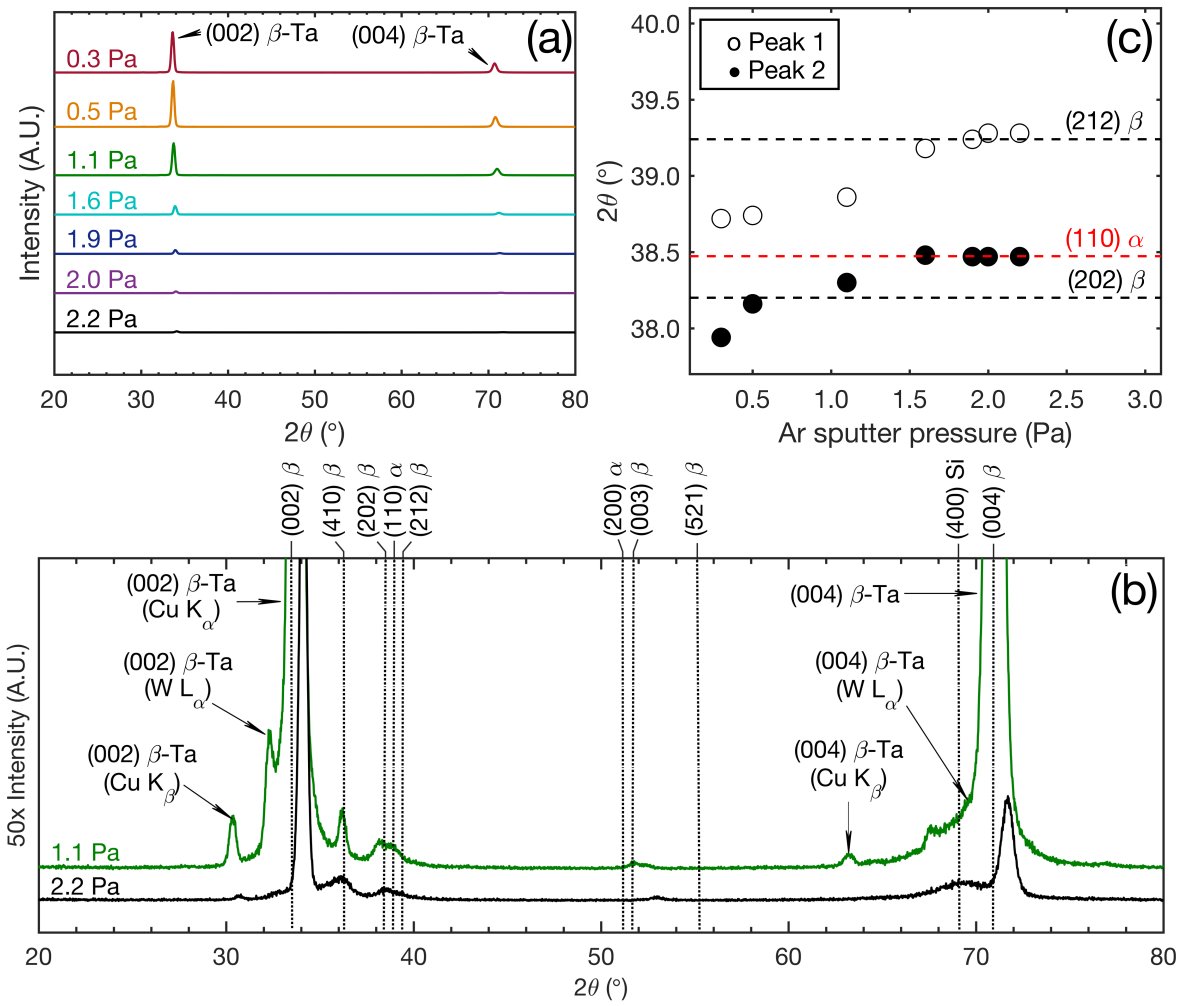

Figure 3.2: (a) X-ray diffraction θ-2θ scans of as-deposited Ta thin films deposited at different argon sputter gas pressures. Only (002) and (004) β-Ta peaks are visible at this scale, both decreasing with increasing p_{Ar}. (b) θ-2θ scans from the 1.1 and 2.2 Pa films expanded 50x (from (a)) show many smaller peaks. All peaks can be unambiguously attributed to β-Ta. (c) Peak position vs. Ar sputter pressure for two peaks, as well as nominal positions of the (202) β, (212) β, and (110) α-Ta peaks. Because they must cross the nominal position over the pressure range, these peaks can be identified as the (202) β and (212) β peaks.

Only β-Ta (002) and (004) peaks are visible at this scale, and the intensity of both decreases by a factor of 40 as p_{Ar} increases from 0.3 to 2.2 Pa. Magnifying by 50x (Fig. 3.2b) reveals several small peaks, whose intensities are nearly constant with p_{Ar}. Also shown in Fig. 3.2b are the locations of the α- and β-Ta peaks from the powder diffraction files (Inorganic Crystal Structure Database Collection Codes 53793 and 280872) that are in close enough proximity to be candidates for indexing of our XRD scans. There are many such peaks; however, our knowledge of film stresses enables us to identify these peaks unambiguously.

As shown in Fig. 3.1, the position of the (002) peak shifts from 33.63° to 34.12° across the pressure range, and this shift tracks the change in stress. Calculating the change in strain, $\Delta\varepsilon_z$, in the film normal direction from this 2θ shift, and the corresponding change in in-plane film stress from $\Delta\sigma_f = -Y\frac{1-\upsilon}{2\upsilon}\Delta\varepsilon_z$, where Y = 170 GPa [47] is the biaxial modulus and using ν = 0.3 as the Poisson ratio, we find $\Delta\sigma_f$ = 2.5 GPa, in excellent agreement with the change in stresses (2.5 GPa) determined from substrate curvature (Fig. 3.1). This indicates that peak shifts can be attributed completely to stress variations across the pressure range. Because the in-plane stresses vary from compressive to tensile, each peak must shift from a 2θ angle below to one above the nominal (ICSD table) angle as p_{Ar} increases.

Using this logic allows us to unambiguously assign the small peaks in Fig. 3.2b as follows: (002) and (004) β-Ta peaks caused by Cu K_β and W L_α radiation are labeled in the figure. Peaks near 36.3˚ and 38.2˚ can be identified as (410) and (202) β-Ta based on IUPAC tables since they are sufficiently far below the only α-Ta peak in the region (the (110) peak at nominal 38.47°) at all p_{Ar}. However, the peak that shifts from 38.72° to 39.28° is near both the (212) β-Ta and (110) α-Ta peaks at nominally 39.24° and 38.47°, respectively. The position of this peak (labelled as "Peak 1") is shown as a function of p_{Ar} in Fig. 3.2c. At low p_{Ar}, it is close to the nominal (110) α-Ta 2θ position, but over the sputter pressure range, this peak shifts to higher 2θ values that ultimately include the nominal (212) β-Ta position at 39.2˚. We therefore assign this peak to (212) β-Ta. Similarly, the position of the peak that varies from 37.94˚ to 38.47˚ ("Peak 2" in Fig. 3.2c) starts below the nominal (202) β-Ta position and moves to the nominal (110) α-Ta position with increasing p_{Ar}. Because the actual peak must cross the nominal value as p_{Ar} increases, we assign peak 2 to (202) β-Ta. It is evident that, if we only had films prepared at high or low pressures in this range, these peaks would have been misassigned.

The small peak that shifts from 2θ = 51.5° (0.3 Pa) and 2θ = 53.0° (2.2 Pa) is clearly distinct from (200) α-Ta (2θ = 55.5°) or (521) β-Ta (2θ = 51.1°) since this peak is always at higher and lower 2θ positions, respectively. We therefore assign this peak to (003) β-Ta, as predicted by Arakcheeva *et al*. [39] for the P-42$_1$m structure and observed by Jiang *et al*. [6]. This peak would

not be visible if these films had the more commonly reported $P4_2/mnm$ [38] structure. We therefore conclude that all of the peaks in our XRD scans are unambiguously attributable to β-Ta. We see no evidence of α-Ta at any sputter pressure.

3.3.3. Texture Analysis

Figures 3.3a and b show the (002) β-Ta rocking curves and the full width at half maximum (FWHM) values of those curves, respectively, from each film.

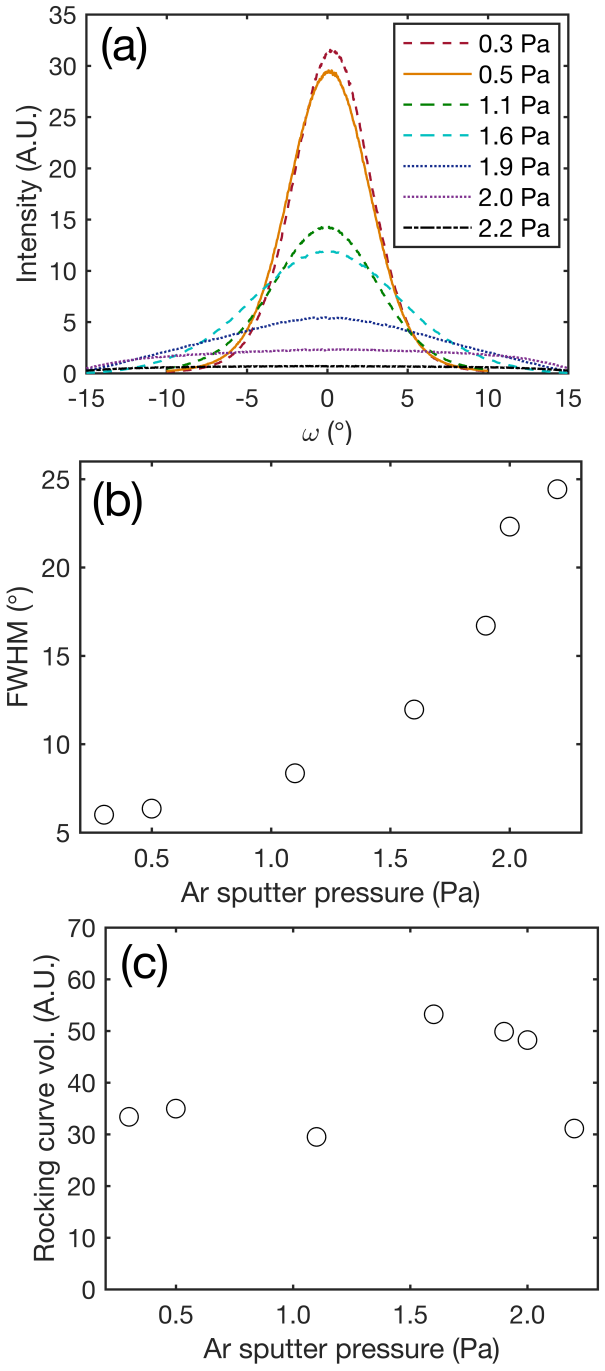

Figure 3.3: (a) Rocking curves from as-deposited Ta thin films deposited at different p_{Ar}. (b) FWHM of rocking curves vs. p_{Ar}. Peak width increases as peak height decreases with p_{Ar}. (c) Modeled 3D rocking curve used to estimate total amount of near-(002)–material. (d) Volume under 3D rocking curve vs. sputter pressure. No trend is apparent, indicating that the volume fraction of (002) oriented grains is approximately constant, although the distribution of the (002) poles about the film normal increases with p_{Ar}.

The FWHM increases from 6° to > 30° across the pressure range. Note that the widths for the 2.0 and 2.2 Pa samples are underestimated due to the constraints of the ω geometry. The texture scans (not shown) showed that the in-plane orientation distributions were random, precluding any epitaxial orientation relationship between film and substrate. Thus, all films have (002) fiber texture.

As p_{Ar} increases, rocking curve height decreases, width increases, and the area under the rocking curves decreases by a factor of 6. To determine whether this is the result of a continual broadening of an essentially (002) fiber texture or the rise of an unrelated randomly-oriented component, we conduct the following analysis: For a continually broadening (002) fiber texture, the area under a single rocking curve does not represent the fraction of the film that belongs to the (002) texture component because the rocking curve detects peaks at only one azimuthal angle, while grains oriented with <002> axes near, but not parallel to, the film normal can occur at any azimuthal angle. A single rocking curve therefore underestimates the total population of near-(002) grains. However, because of the fiber texture, the rocking curves must be independent of azimuthal angle. Thus, a good representation of the population of near-(002)–oriented grains in each film can be obtained by rotating the measured rocking curve (Fig. 3.3a) about the film normal to construct a simple model 3-D rocking curve. A relative measure of the total population of near-(002)-oriented grains in each film may then be obtained by calculating the volume under the 3-D curves generated in this way.

The results of this analysis are shown in Figure 3.3c. There is no evidence of a decrease in the amount of near-(002)-oriented material with Ar sputter pressure, suggesting that all films have (002) fiber texture that becomes less sharp—*i.e.* the width of the distribution of angles between crystal <002> directions and the film normal increases—with increasing sputter pressure.

3.4. DISCUSSION

Surprisingly, p_{Ar} has a dramatic effect on nearly all aspects of film structure *except phase*. Below, we analyze how p_{Ar} determines the energy and incident angle of the species arriving at the substrate during deposition, and how these, in turn, determine stresses and texture. Finally, we use these results to propose a model for β-Ta phase formation that is consistent with our results and with the majority of the published literature.

3.4.1. Phase identification and crystal structure of the β-Ta phase

In XRD θ-2θ scans, β-Ta has many small peaks, several of which are near to α-Ta peaks. Some of these are shown in Fig. 3.2b. As is evident in Fig. 3.2c, the strains that arise during deposition are enough to shift the measured peaks fully to the nominal (unstrained) positions of other peaks. For example, had we simply deposited films at 1.6–2.2 Pa (12–16 mTorr), we would have misassigned the (202) β peak to (110) α and concluded that we had mixed texture. Indeed, since (110) is the most common orientation seen in α-Ta films, there would scarcely have been a reason to doubt this assignment. Only by tracking the positions of these peaks with p_{Ar}, and thereby stress, over a wide enough range were we able to correctly assign them. Given that the stresses we measure (Fig. 3.1) are similar to those reported by others [48], it is possible that such misassignments have occurred in previously published results.

This unambiguous peak assignment also makes it possible to comment on the crystal structure of β-Ta. Upon its discovery in 1965, the beta phase was recognized to have a tetragonal structure [1]. In 1972, Moseley and Seabrook's powder diffraction work led them to propose that β-Ta is isomorphous with β-U, with space group $P4_2/mnm$ (Frank-Kasper sigma structure, [49]) [38]. In 2002, an alternate structure—a distorted Frank-Kasper sigma structure with space group $P\text{-}42_1m$—was proposed by Arakcheeva *et al*. based on the results of single crystal diffraction experiments [39]. The two structures are very similar but the (001) and (003) peaks are expected to be extinguished for the sigma structure, while they should be present, though small, for the structure proposed by Arakcheeva. The (001) and (003) peaks were clearly identified by Jiang *et*

al. [6], and Lee *et al*. [50] agreed that the Arakcheeva structure provides a better fit to their data. However, the Moseley and Seabrook sigma structure is still widely cited [7,18,51,52]. Thanks to the strong texture of our β-Ta films, the (003) diffraction peak is clearly visible in our data, providing additional evidence that the structure proposed by Arakcheeva is correct.

3.4.2. Effect of working gas pressure in sputter deposition

In sputter deposition, p_{Ar} plays an important role in determining the distributions of both the energy [40] and incident angle [53] of incoming species at the substrate. By understanding these relationships, we can understand the variations in stress (Fig. 3.1) and texture (Fig's 3.2 and 3.3) in our β-Ta films.

In sputtering, a plasma is ignited between a target and a substrate, and plasma ions are accelerated into the target. Some of those ions are neutralized and are "reflected" back across the plasma towards the substrate. Others cause atoms to be ejected, or "sputtered" from the target. Some of these sputtered target atoms then travel across the plasma and are deposited on the substrate. The sputter gas pressure affects the path of sputtered atoms as shown in Figure 3.4.

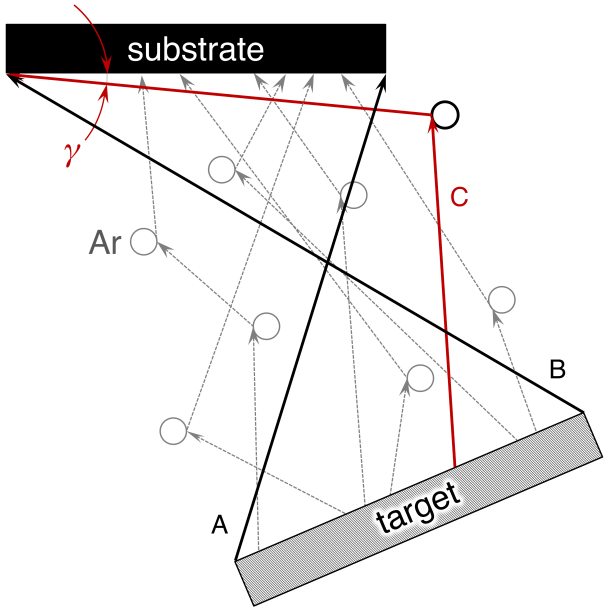

Figure 3.4: Schematic showing how increasing sputter gas pressure broadens the distribution of incident angles of Ta adatoms and reflected Ar neutrals at the substrate. (a) In a perfect vacuum, these species travel along line-of-sight paths and approach the substrate at a limited range of incident angles, γ. (b) At low sputter pressures, few collisions occur and most atoms approach the substrate at higher incident angles, although lower angles are possible. (c) At higher sputter pressures, incoming atoms collide with many more sputter gas atoms and more frequently approach the substrate at lower incident angles.

When p_{Ar} is low enough that the mean free path (average distance between collisions of either sputtered atoms or reflected neutrals with sputter gas species) is larger than the target-substrate distance, most sputtered atoms and reflected neutrals reach the substrate without colliding with sputter gas atoms. They travel in straight lines and the range of incident angles, γ, at the substrate is determined by target/substrate geometry. As pressure increases, collisions occur more frequently and the energy of the incident species decreases [40] while the range of possible incident angles increases [53]. Both the energy and incident angle distributions of species arriving at the growing film surface are thus determined by p_{Ar}. The mean free path, λ, for Ta atoms sputtered using Ar can be calculated from [54]

$$\lambda = \frac{k_B T}{\sqrt{2}\pi a_0^2 p_{Ar}}, \tag{3.1}$$

where k_B is the Boltzmann constant, T the temperature (298 K), and a_0 the diameter of a tantalum atom (0.292 nm). Using this formula, the expected number of collisions between target and substrate varies from about 3 to more than 25 over our experimental pressure range.

To estimate the energies of the species incident at the substrate, we combine two different models by Drüsedau *et al.*: one in which the initial energies of sputtered and reflected species at the target are calculated based on empirical rules [55], and another which describes energy loss as a function of sputter pressure [56]. The average energy per incorporated Ta atom $\langle E_t \rangle$ may be written as

$$\langle E_t \rangle = U_0 + \langle E_{at} \rangle \exp(-c_{Ta} p_{Ar} d) + \langle E_{Ar} \rangle \exp(-c_{Ar} p_{Ar} d) + \langle E_p \rangle, \tag{3.2}$$

where U_0 is the surface binding energy of the target material (8.1 eV [57]), $\langle E_{at} \rangle$ the average atomic energy of Ta atoms at the target, $\langle E_{Ar} \rangle$ the average energy of reflected Ar neutrals at the target, $\langle E_p \rangle$ the average contribution of irradiation by electrons near the cathode, d the distance from target to substrate, and c_{Ta} and c_{Ar} are constants which describe the rate of energy loss for Ta and Ar atoms, respectively, as they travel from the target to the substrate. The exponential terms account for energy loss due to collisions with the sputter gas. Drüsedau *et al.* performed these calculations for Ge and Mo; we combine these analyses to estimate results for Ta.

We begin by expanding the atomic energy term,

$$\langle E_{at} \rangle = U_0^{2/3} + E_{\max}^{1/3}. \tag{3.3}$$

Here, E_{max} is the maximum transferred energy per incorporated Ta atom, given by

$$E_{\max} = k E_0 \frac{4 m_{Ar} m_{Ta}}{(m_{Ar} + m_{Ta})^2} - U_0, \tag{3.4}$$

where E_0 is the kinetic energy of the ions (400 eV for this experiment), m_{Ar} and m_{Ta} are the atomic masses of argon and tantalum, respectively, and k is a fitting parameter representing the energy dissipation during the collision cascade at the target. Drüsedau *et al.* found this parameter to vary between 0.1 and 0.4; we chose $k = 0.25$ as an estimate for our system.

The energy of the reflected neutrals can be expressed as:

$$\langle E_{Ar} \rangle = E_0 \frac{R_E}{y}, \tag{3.5}$$

where y is the sputtering yield in tantalum atoms per ion (≈ 0.48 at $E_0 = 400$ eV [58]). R_E, the reflection coefficient, represents the fraction of incident energy that is carried by reflected neutrals to the substrate and is given by

$$R_E = \frac{\left(m_{Ta} - m_{Ar}\right)^{\eta}}{m_E^{\eta}} \quad , \tag{3.6}$$

where m_E and η are fitting parameters determined by Drüsedau *et al*. to be 208 a.m.u. and 1.26 respectively. Finally, the average energy contribution due to irradiation by the electrons near the cathode can be estimated from

$$\langle E_p \rangle = \frac{5.33}{y} \text{ eV}. \tag{3.7}$$

Using the above values, we estimate that the total average energy per incorporated Ta atom varies from approximately 363 eV for the film deposited at 0.3 Pa to 38.8 eV for the film deposited at 2.2 Pa, as shown in Figure 3.5.

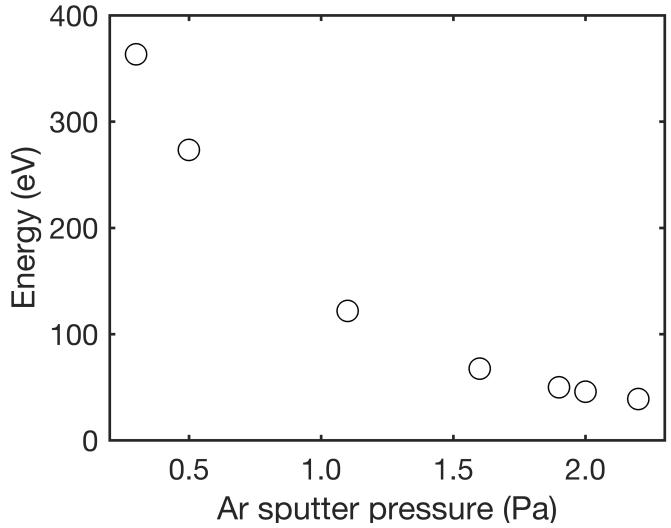

Figure 3.5: Total average energy added to film per incorporated Ta atom vs. p_{Ar}, calculated using empirical rules developed by Drüsedau et al [59,60]. Energy decreases from approximately 363 eV for the film deposited at 0.3 Pa to 38.8 eV for the film deposited at 2.2 Pa.

These values are comparable to experimental values measured by other researchers at similar pressures [55,59,60]. The energy due to bombardment by reflected Ar neutrals contributes the largest part, accounting for 93% in the case of the 0.3 Pa film and 50% for the 2.2 Pa film.

Despite the large change in the energy of incident species during deposition, we see no change in phase over our entire sputter pressure range. This is surprising, as p_{Ar} has been said to affect the phase of Ta films [4,33,34,41–43] by controlling particle energy. The results of those studies are contradictory, however. Fig. 3.6 shows the phases identified by several different researchers as a function of p_{Ar}, along with our results.

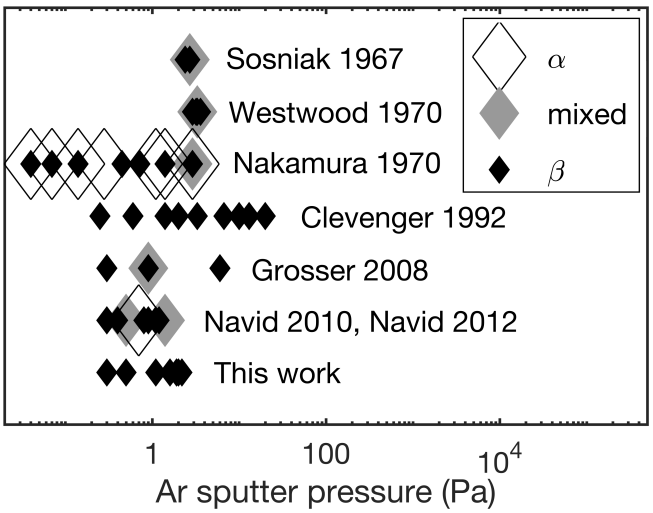

Figure 3.6: Summary of literature on the effect of sputter pressure on phase selection in Ta films. All works cited in this figure report films deposited on unheated Si or SiO_2 using DC sputtering in Ar. No clear pattern is apparent. [4,35,44,46,47,66,70]

All films were deposited on Si or SiO_2 below 300˚C using DC magnetron sputtering, with minimal variation in other parameters. Yet, no clear pattern emerges. Like us, Clevenger [61] found β-Ta over a wide range of p_{Ar}. All of the others reported some combination of α, β, and mixed phases, but the pressures at which each phase appears do not follow any consistent pattern. Possible XRD peak misindexing aside, p_{Ar} alone clearly cannot explain phase selection in Ta. The variations in energy and incident angle do, however, account for the variations in stress and texture we observe, and allow us to propose a model for β-phase selection that accounts for virtually all results published to date.

3.4.3. Stresses

The effect of sputter pressure on film stress is well understood in terms of the energies of the incident species at the growing film surface. At higher energies, bombarding particles create self-interstitial defects below the film surface, leading to compressive stresses [62]. Reducing the energy reduces the number of self-interstitials and the film approaches the behavior seen in the absence of energetic particle bombardment, commonly a tensile stress state attributed to island coalescence [63]. As evident in Figure 3.7, our films show this typical behavior: films sputtered at low pressure (high incident energy) show large compressive stresses, and as sputter pressure increases, stresses become more tensile as the energy of the bombarding particles decreases. Our results agree with previously published data for Ta films [48].

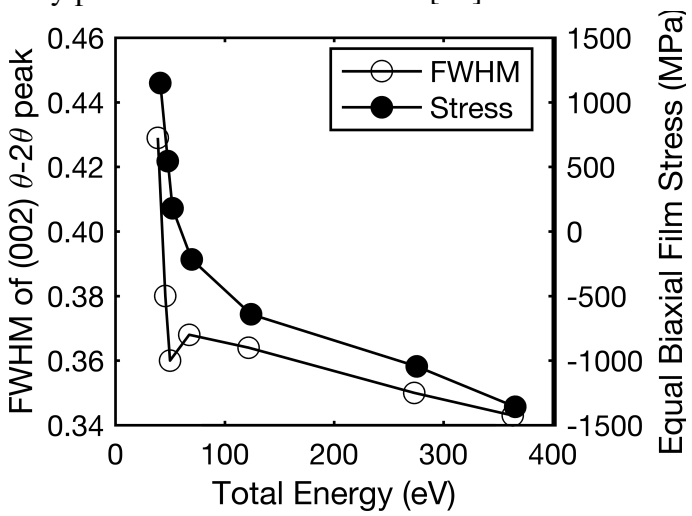

Figure 3.7: FWHM of (002) β-Ta θ-2θ peak and average equal-biaxial film stress vs. total energy added to film per Ta atom. Peak width decreases as energy increases due to the corresponding increase in the sharpness of the (002) fiber texture. As the breadth of the orientation distribution decreases, less strain transfer occurs at grain boundaries and the stress field becomes more homogeneous.

In addition, Fig. 3.7 shows that the width of the (002) β-Ta θ-2θ peak also decreases as energy increases. In films of anisotropic crystals, grains with different orientations have different in-plane elastic properties and must therefore transfer strain from grain to grain to maintain stress continuity [64]. As the orientation distribution broadens with increasing p_{Ar}, the strain must become more inhomogeneous due to strain transfer. This is reflected in the broader θ-2θ peak widths observed in films deposited under higher p_{Ar}. Peak broadening due to this mechanism also

depends on the stress. As the average film stress approaches zero, the broadening effect should diminish as the average strain in each grain approaches zero. This may explain the trough in peak width at the film deposited at 1.9 Pa, which corresponds to the lowest average film stress.

3.4.4. Texture

Most researchers have estimated texture in β-Ta films by simply comparing peak heights in symmetric θ-2θ scans to powder diffraction peak height data. This approach has shown that some degree of (002) texture is common [1,3,9,20,21,33,41,65,66]. A small (202) component has also been reported [3,27,41,66]. However, symmetric θ-2θ scans do not provide a complete description of texture. This method says nothing about in-plane texture, can miss texture components that are present but are either weak or have no out of plane reflections, and cannot distinguish between broad texture distributions and weak texture.

Fig. 3.3c shows that the volume fraction of grains having [002] near (within about 25˚) the film normal does not decrease as p_{Ar} increases. This analysis thus reveals an important finding that would not be detected in a simple θ-2θ scan; namely, that these films exhibit a single, continuously broadening, near-(002) fiber texture, and not an (002) fiber texture component with a fixed angular distribution that is gradually replaced by randomly-textured grains as p_{Ar} increases. In the latter case we would have rocking curves of fixed width that shrink with increasing p_{Ar}, and the volume under the rotated rocking curve (Fig. 3.3c) would also decrease. We will call the former *texture broadening* and the latter *texture weakening*. The type of texture broadening shown in Fig. 3.3 has been described only once before, to our knowledge, in Co-Cr alloy films [67], but no mechanistic explanations were proposed. We propose a mechanism based on selective resputtering of less well-aligned grains with increasing incident particle energy, by analogy with a well-known process in ion beam assisted deposition (IBAD).

In IBAD, a collimated ion beam directed towards the surface of a growing film causes certain orientations to be favored. With IBAD, it is possible to improve film texture and even to grow films with textures that are otherwise uncommon [68,69]. Two mechanisms have been proposed

to explain this phenomenon: first, that bombarding ions selectively resputter unfavorably-oriented grains [70], and second, that bombarding ions preferentially damage unfavorably-oriented grains, which then recrystallize [69,71]. Both mechanisms rely on the principle that ions are less likely to interact with a crystal when travelling along the relatively open channeling directions, with the result that crystals with their channeling directions parallel to the ion flux are preserved at the expense of other orientations.

While sputtering is not identical to ion assisted deposition, there are clear similarities in that both processes involve a flux of energetic particles bombarding a growing film. The most important difference is that sputtering features bombarding particles with a distribution of incident angles, while a collimated beam is typical in IBAD. However, IBAD experiments that involve a distribution of angles by rotating the substrate under an obliquely directed ion beam can produce fiber textures [72]. As the substrate rotates, each grain experiences bombardment from different angles depending on its position, equivalent to a distribution of incident angles. This is nevertheless effective in promoting fiber texture since grains that have their channeling directions parallel to the ion flux at some point in the rotation are preferentially preserved because they experience less resputtering than grains that are never preferentially oriented [72]. Similarly, our growing films experience a bombarding flux with a distribution of incident angles that is approximately Gaussian with its peak parallel to the film normal (simulations not shown). Thus, grains having preferential channeling directions parallel to the substrate normal would experience less resputtering than others and be preferentially preserved. While channeling directions have not been reported for β-Ta, the crystal structure features well-defined open channels along the [002] direction [39]. Thus, (002) fiber texture could be promoted in energetic sputtering by a mechanism analogous to texturing in IBAD.

This model is consistent with the broadening (002) texture component that we observe since both the decreasing bombardment energy and the broadening distribution of incident angles that occur with increasing p_{Ar} would decrease the effectiveness of the proposed texturing mechanism. Reduced energy would lead to a lower resputtering rate [73,74] and less damage to unfavorably-

oriented crystals [69], and would therefore decrease the removal rate of poorly-aligned grains, while a broadening incident angle distribution would mean that the range of angles over which (002) nuclei are preferentially preserved increases, even if the energy were constant. Either way, the texture distribution would become broader with increasing sputter pressure.

The calculations in section 4.2 suggest that our energies are within or near the range needed to cause resputtering or other damage [58,68]. Sputtering is typically considered to require at least ten times the surface binding energy [75]. Using values from section 4.2, we find a threshold energy for sputtering in Ta of approximately 81 eV/atom, while the bombarding energies in our experiments range from 363 eV/atom at 0.3 Pa to 38.8 eV/atom at 2.2 Pa. While these are average values, it is clear that our energy range includes a regime where the resputtering mechanism should be very effective as well as a regime where little, if any, resputtering should occur.

The texture observed in the films deposited under high p_{Ar}, is therefore likely to be representative of the orientation distribution of the initial grain nuclei; *i.e.* the texture that would develop in the absence of the resputtering mechanism. In other words, (002) nuclei (over some range in ω) are not only favored by the resputtering mechanism, but are virtually the only nuclei present. If, instead, nuclei formed with random orientations, we would expect to observe texture weakening rather than texture broadening as the resputtering mechanism became less effective with increasing p_{Ar}. The (002) texture broadening and the very small fraction of non-(002) oriented grains we observe indicates that the initial nuclei must consist of almost exclusively near-(002)-oriented grains at all p_{Ar}. As p_{Ar} decreases, resputtering preserves those whose [002] directions are closer and closer to the substrate normal, leading to the peak width variations that we see (Fig. 3.3).

This explanation does not account for all of the small XRD peaks that are not part of the (002) texture component. Fig 3.2b shows β peaks corresponding to (202), (212), and (410). As the [202] and [212] directions are relatively close to [002] (27.5° and 13.4° respectively), these texture components can be considered part of the of the broadening (002) texture component.

(Note that reports of secondary (202) texture components in literature [3,27,41,66] may also represent misidentified α–Ta since the (202)-β peak is very near the (110)-α peak.) This leaves only the (410) component (approximately 0.1% of the film according to a comparison of XRD peak intensities), which cannot be a part of the (002) component as [410] is 90° from [002]. Further work is required to discover how this minor texture component forms.

3.4.5. Phase Selection

The finding that virtually all of the grain nuclei have (002) orientations (over a range in ω) leads to the critical realization that the (002) orientation may in fact be *required* for beta formation. By combining this conclusion with reported effects of surface chemistry and impurities during deposition, we are able to propose a phase selection mechanism that is consistent with the majority of published results, as well as those presented here.

As mentioned in the Introduction, oxygen seems to play an important role in the stabilization of the β phase: oxide layers tend to promote β-Ta [20], oxygen impurities in the sputter gas are often associated with β-Ta [76], and β-Ta films with higher oxygen content require a higher annealing temperature to transform to the stable α phase [77]. The (002) orientation relationship and close affiliation with oxygen spurred us to look more closely at Mills' 1966 [19] suggestion that a metastable TaO_2 layer may play an important role in stabilizing β-Ta. Mills noted that Ta sputtered on oxide substrates usually forms the β phase while Ta sputtered on gold or carbon produces the α phase, and speculated that arriving Ta atoms may reduce the oxide at a substrate surface to produce TaO_2, which has a tetragonal structure, so that tetragonal β-Ta could then grow epitaxially on this layer.

Our analysis suggests that this mechanism is plausible. Basic oxidation potential calculations show that Ta readily reduces SiO_2. Schonberg [78] notes that TaO_2 can be prepared by oxidation or reduction, and reports that this phase, which he calls δ-TaO_2, has the rutile structure, with a = 4.709 Å and c = 3.065 Å. This structure has not received much study and these values are not well known. Nevertheless, we can use these values as a starting point to explore possible

epitaxial relationships. The β-Ta structure is a layered structure with an ABAC stacking, and the Ta atoms in the δ-TaO_2 structure occupy a single plane as well. Matching the Ta layer of four unit cells of the δ-TaO_2 structure using the above values of a and c to the A layer of one unit cell of the Arakcheeva β-Ta structure as shown in Figure 3.8 would require about 8% compressive strain in the growing film.

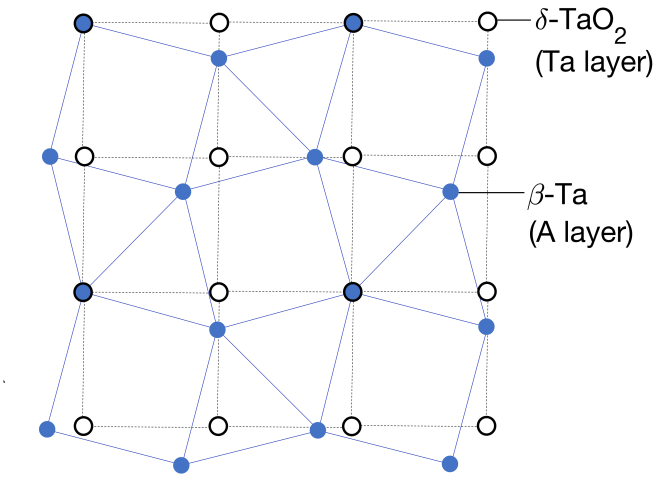

Figure 3.8: Proposed epitaxial match by growth of β-Ta on a layer of TaO_2. a) Detail of the A layer of β-Ta and the Ta layer of TaO_2 with approximately 8% strain.

This arrangement does not permit a perfect match for every atom, but it is plausible that the oxide serves as a template for β-Ta. Atoms in the strained β-Ta layer that are not associated with a corresponding site in the TaO_2 layer may appear instead as vacancies, diffuse into the TaO_2 layer, or appear as additional atoms in the channels of the structure. Indeed, studies of the β-Ta structure have shown evidence of such interstitial defects [39].

This mechanism can explain much of the confusion surrounding phase formation in the Ta film literature. Below are several phenomena reported in that literature, and the explanations provided by our proposed mechanism.

- **β-Ta generally forms on oxide substrates, while α generally forms on oxide-free substrates** ([19–21,24,79]). If incoming Ta at the substrate surface can reduce the oxide to form TaO_2, β-Ta could form on this surface.

- **Oxygen impurities in the sputtering gas promote the formation of the β phase** ([25,27]). If sufficient oxygen is initially available in the sputtering gas to form TaO_2, β-Ta could form even in cases where oxygen is not available on the substrate.
- **Preheating substrates promotes α-Ta** ([16,20,25]). Adsorbed water provides another source of oxygen [28], so preheating substrates to remove adsorbed water promotes α-Ta.
- **Organic impurities on the substrate surface promote α-Ta** ([14,26]). An organic layer could prevent depositing Ta from interacting with oxygen on the substrate to form TaO_2.
- **In some cases, increasing incident particle energy promotes α-Ta** ([2,4,7,8,36]). If an oxide layer were removed by plasma cleaning, depositing Ta atoms would form α-Ta.
- **In other cases, increasing incident particle energy promotes β-Ta** ([2,4,7–9,11,36]). If, instead of removing oxides, incident particles instead knock off impurity atoms, Ta atoms will then be able to interact with substrate oxygen to form TaO_2 and hence β-Ta.
- **Poor vacuum can promote β-Ta** ([33]). If the oxygen content of the deposition environment is high, depositing Ta might getter sufficient oxygen to form TaO_2 during the initial stages and hence β-Ta.
- **(002) texture is very common in β-Ta** ([1,3,9,20,21,33,65,66,76]). A mechanism that depends on an orientation relationship would naturally lead to preferred texture.

This model can also explain the disparate literature results summarized in Fig. 3.6. All of the films in this figure were deposited on oxidized Si or SiO_2 at low-temperature, so we expect only β-Ta based on our model; yet, several there are several reports of both α- and β-Ta deposited at the same sputter pressures. However, all of the films that contain α-Ta were deposited in circumstances likely to result in surface impurities; some were deposited after shorter or no presputtering [34,42], with lower-grade argon [41], or for longer deposition times [43] than other films in the series. These results are consistent with the effects of impurities such as nitrogen or organic compounds (*e.g.* pump oil). In particular, variations in phase reported by Navid *et al.* [4,33] may be due to the substrate cleaning procedure used, which included a rinse in isopropyl alcohol, a procedure likely to result in different amounts of organic residue on different

substrates, which could lead to variable amounts of α-Ta in each film. For the present films, organic solvents that could leave surface residues were avoided. A gentle plasma clean removed adsorbed water and other adatoms without being aggressive enough to remove the native oxide (as evidenced by the lack of in-plane texture in the films). Thus, an initial TaO_2 layer could be formed on all samples leading to formation of β-Ta films.

There is an important distinction to be made about the role of oxygen in stabilizing the β phase: While some amount of oxygen is, according to this hypothesis, required to form β-Ta (by forming a TaO_2 template layer), the β phase itself does not require stabilization by impurities as claimed by some (*e.g.* [25,41]). Oxygen is required only for the first few layers of growth as it has been established that β-Ta may be grown in a nominally oxygen-free state [26,77].

3.5. SUMMARY AND CONCLUSIONS

Many factors affect phase selection in Ta thin films. We eliminated substrate effects (all films are deposited on (100) Si with native oxide), impurity effects (all films are deposited under UHV in UHP Ar with additional O_2 filtration), and heating effects (all substrates were unheated) so that we could examine the effects of sputter pressure (from 0.3 to 2.2 Pa) in isolation.

Stresses were found to vary from -1360 to 1140 MPa, consistent with existing stress generation models. XRD returned many small peaks, but the shifts in their positions induced by the stresses made it possible to unambiguously identify them. We found only β-Ta over the entire pressure range, and in addition, could confirm that the structure of β-Ta is consistent with the P-42_1m structure proposed by Arakcheeva *et al*. [39] and not the more commonly reported $P4_2$/mnm [38] structure. Calculations showed that the energy per incorporated Ta atom varied from 363 to 38.8 eV with increasing p_{Ar}.

The vast majority of grains in the film were part of an (002) texture component that broadened with p_{Ar}. This texture broadening could be explained by an initial orientation distribution of (002) nuclei that was subsequently sharpened by resputtering due to the high energy of species impinging on the growing film surface at low pressures, but grew without

resputtering at higher pressures as the incident energies decreased and range of incident angles increased. The fact that the texture broadened rather than weakened with p_{Ar} suggests that the beta phase forms as the result of an orientation relationship with the substrate.

Based on these results, we propose a mechanism to explain phase selection in Ta films that is consistent with our results as well as the vast majority of previously published results—to wit, that β-Ta is formed preferentially in systems where oxygen is present such that a TaO_2 layer can be formed at the substrate/film interface and that the (002) orientation grows on this oxide layer. We propose a possible epitaxial relationship and show that this mechanism can help to explain essentially all effects reported in the Ta film phase selection literature, including effects of substrate material [19–21,24], oxygen in the base pressure or sputter gas [25,27], adsorbed water [16,20,25], organic impurities [14,26], and incident particle energy [2,4,7–9,11,36]. This model may make it possible to develop methods to reliably produce either α or β-Ta films as desired.

3.6. ACKNOWLEDGMENTS

Support for this work was provided by the National Science Foundation (DMR 0706507). This work also made use of the facilities of the Cornell Center for Materials Research with support from the National Science Foundation Materials Research Science and Engineering Centers program (DMR 1120296). We also thank Yong Qiang Wang at Los Alamos National Laboratory for assistance with RBS measurements.

3.7. REFERENCES

[1] M.H. Read, C. Altman, A new structure in tantalum thin films, Appl. Phys. Lett. (1965).

[2] K. Ino, T. Shinohara, T. Ushiki, T. Ohmi, Ion energy , ion flux , and ion species effects on crystallographic and electrical properties of sputter-deposited Ta thin films, J. Vac. Sci. Technol. A. 15 (1997) 2627–2635.

[3] G.S. Chen, P.Y. Lee, S.T. Chen, Phase formation behavior and diffusion barrier property of reactively sputtered tantalum-based thin films used in semiconductor metallization, Thin Solid Films. 353 (1999) 264–273. doi:10.1016/S0040-6090(99)00431-9.

[4] A.A. Navid, A.M. Hodge, Controllable residual stresses in sputtered nanostructured alpha-tantalum, Scr. Mater. 63 (2010) 867–870. doi:10.1016/j.scriptamat.2010.06.037.

[5] L. Gladczuk, A. Patel, J.D. Demaree, M. Sosnowski, Sputter deposition of bcc tantalum films with TaN underlayers for protection of steel, Thin Solid Films. 476 (2005) 295–302. doi:10.1016/j.tsf.2004.10.020.

[6] A. Jiang, T.A. Tyson, L. Axe, L. Gladczuk, M. Sosnowski, P. Cote, The structure and stability of beta-Ta thin films, Thin Solid Films. 479 (2005) 166–173. doi:10.1016/j.tsf.2004.12.006.

[7] H. Ren, M. Sosnowski, Tantalum thin films deposited by ion assisted magnetron sputtering, Thin Solid Films. 516 (2008) 1898–1905. doi:10.1016/j.tsf.2007.10.127.

[8] R.A. Roy, Role of energetic atoms and ions in Ta films grown by different physical vapor deposition methods, J. Vac. Sci. Technol. B Microelectron. Nanom. Struct. 11 (1993) 1921. doi:10.1116/1.586523.

[9] K. Valleti, A. Subrahmanyam, S. V. Joshi, Growth of nano crystalline near α phase tantalum thin films at room temperature using cylindrical magnetron cathode, Surf. Coatings Technol. 202 (2008) 3325–3331. doi:10.1016/j.surfcoat.2007.12.019.

[10] Y.M. Zhou, Z. Xie, H.N. Xiao, P.F. Hu, J. He, Effects of deposition parameters on tantalum films deposited by direct current magnetron sputtering in Ar-O2 mixture, Appl. Surf. Sci. 83 (2008) 286–291. doi:10.1016/j.apsusc.2011.10.012.

[11] P. Catania, R.A. Roy, J.J. Cuomo, Phase formation and microstructure changes in tantalum thin films induced by bias sputtering, J. Appl. Phys. (1993).

[12] J. Zhang, Y. Huai, L. Chen, J. Zhang, Formation of low resistivity alpha Ta by ion beam sputtering, J. Vac. Sci. Technol. B Microelectron. Nanom. Struct. 21 (2003) 237. doi:10.1116/1.1535931.

[13] M. Shiojiri, S. Shinkai, K. Sasaki, H. Yanagisawa, Y. Abe, Preparation of low-Rresistivity α -Ta thin films on (001) Si by conventional DC magnetron sputtering, Jpn. J. Appl. Phys. 42 (2003) 4499–4500. doi:10.1143/JJAP.42.4499.

[14] J.J. Senkevich, T. Karabacak, D.-L. Bae, T.S. Cale, Formation of body-centered-cubic tantalum via sputtering on low-ϰ dielectrics at low temperatures, J. Vac. Sci. Technol. B Microelectron. Nanom. Struct. 24 (2006) 534. doi:10.1116/1.2166860.

[15] L. Liu, C.-F. Pai, Y. Li, H.W. Tseng, D.C. Ralph, R.A. Buhrman, Spin-Torque Switching with the Giant Spin Hall Effect of Tantalum, Science (80-.). 336 (2012).

[16] C.S. Whitman, Effect of various sputtering parameters on Ta phase formation using an I-Optimal experimental design, J. Vac. Sci. Technol. B Microelectron. Nanom. Struct. (2000). doi:10.1116/1.1319701.

[17] N. Schwartz, W.A. Reed, P. Polash, M.H. Read, Temperature coefficient of resistance of beta-tantalum films and mixtures with b.c.c.-tantalum, Thin Solid Films. 14 (1972) 333–347. doi:10.1038/467S2a.

[18] L. Gladczuk, A. Patel, C.S. Paur, M. Sosnowski, Tantalum films for protective coatings of steel, Thin Solid Films. 467 (2004) 150–157. doi:10.1016/j.tsf.2004.04.041.

[19] D. Mills, The Structure of Sputtered Tantalum, J. Can. Ceram. Soc. 35 (1966) 48.

[20] L.G. Feinstein, R.D. Huttemann, Factors controlling the structure of sputtered Ta films, Thin Solid Films. 16 (1973) 129–145.

[21] S. Sato, Nucleation properties of magnetron-sputtered tantalum, Thin Solid Films. 94 (1982) 321–329. doi:10.1016/0040-6090(82)90493-X.

[22] D.W. Face, Nucleation of body-centered-cubic tantalum films with a thin niobium underlayer, J. Vac. Sci. Technol. A Vacuum, Surfaces, Film. 5 (1987) 3408. doi:10.1116/1.574203.
[23] F. Sajovec, P. Meuffels, T. Schober, Structural and electrical properties of ion beam sputter deposited tantalum films, Thin Solid Films. 219 (1992) 206–209. doi:10.1016/0040-6090(92)90744-V.
[24] L.G. Feinstein, R.D. Huttemann, Short Communication Role of surface hydroxyls in the nucleation of sputtered tantalum films The surfaces of reactively sputtered TazN thin films have been oxidized by, 12 (1972) 47–49.
[25] A. Schauer, M. Roschy, R.F. sputtered β-tantalum and b.c.c. tantalum films, Thin Solid Films. 12 (1972) 313–317. doi:10.1016/0040-6090(72)90095-8.
[26] N. Schwartz, E.D. Feit, Impurity Effects in the Nucleation of Alpha (bcc)-Tantalum or Beta-Tantalum Films, J. Electrochem. Soc. 124 (1977) 123–131. doi:10.1149/1.2133224.
[27] N. Waterhouse, P.S. Wilcox, D.J. Willmott, Effect of oxygen on the electrical and structural properties of triode-sputtered tantalum films, J. Appl. Phys. 42 (1971) 5649. doi:10.1063/1.1659995.
[28] W.D. Westwood, D.J. Willmott, P.S. Wilcox, Tantalum Films Triode-Sputtered in Mixtures of Argon and Water Vapor, J. Vac. Sci. Technol. 9 (1972) 987. doi:10.1116/1.1317843.
[29] L.G. Feinstein, Phases Observed in Oxygen-Reactive Sputtering of Tantalum Phases Observed in Oxygen-Reactive Sputtering of Tantalum, 137 (1971) 5–7. doi:10.1063/1.1653857.
[30] P.N. Baker, R.F. sputtered tantalum films deposited in an oxygen doped atmosphere, Thin Solid Films. 6 (1970) R57–R60.
[31] R.D. Huttemann, J.M. Morabito, C.A. Steidel, D. Gerstenberg, Effect of light elements nitrogen, carbon and oxygen on physical properties of sputtered tantalum films, Jpn. J. Appl. Phys. 2 (1974) 513–526.
[32] C.R. Aita, Glow discharge mass spectrometry of sputtered tantalum nitride, J. Vac. Sci. Technol. 18 (1981) 324. doi:10.1116/1.570751.
[33] A.A. Navid, A.M. Hodge, Nanostructured alpha and beta tantalum formation—Relationship between plasma parameters and microstructure, Mater. Sci. Eng. A. 536 (2012) 49–56. doi:10.1016/j.msea.2011.12.017.
[34] J. Sosniak, W.J. Polito, G.A. Rozgonyi, Effect of Background-Gas Impurities on the Formation of Sputtered β-Tantalum Films, J. Appl. Phys. (1967). doi:10.1063/1.1710059.
[35] S.L. Lee, J. Mueller, D. Windover, Real-time XRD characterization of growth of sputtered tantalum films, Mater. Res. Soc. Symp. Proc. 840 (2005) 1–6.
[36] J. Alami, P. Eklund, J.M. Andersson, M. Lattemann, E. Wallin, J. Bohlmark, P. Persson, U. Helmersson, Phase tailoring of Ta thin films by highly ionized pulsed magnetron sputtering, Thin Solid Films. 515 (2007) 3434–3438. doi:10.1016/j.tsf.2006.10.013.
[37] D. Collobert, Y. Chouan, A new hypothesis about sputtered tantalum, Thin Solid Films. 55 (1978) 15–16.
[38] P.T. Moseley, C.J. Seabrook, The crystal structure of beta-tantalum., Acta Cryst. (1973).
[39] A. Arakcheeva, C. Gervais, V. Grinevitch, The self-hosting structure of b -Ta, Acta Crystallogr. Sect. B. B58 (2002) 1–7.
[40] J.A. Thornton, High rate thick film growth, Annu. Rev. Mater. Sci. 7 (1977) 239–260. doi:10.1146/annurev.ms.07.080177.001323.
[41] W.D. Westwood, F.C. Livermore, Phase composition and conductivity of sputtered tantalum, Thin Solid Films. (1970). doi:10.1016/0040-6090(70)90112-4.
[42] M. Nakamura, F. Fujimori, N. Nishimura, Phase forming processes in tantalum films through sputtering, Jpn. J. Appl. Phys. 9 (1970) 557.
[43] M. Grosser, U. Schmid, The impact of sputter conditions on the microstructure and on the resistivity of tantalum thin films, Thin Solid Films. 517 (2009) 4493–4496. doi:10.1016/j.tsf.2008.12.009.
[44] J.B. Shu, S.S. Clyburn, T.E. Mates, S.P. Baker, Effect of oxygen on the thermomechanical

behavior of passivated Cu thin films, J. Mater. Res. 18 (2003) 2122.
[45] G.G. Stoney, The tension of metallic films deposited by electrolysis, Proc. R. Soc. London, Ser. A. 82 (1909) 172–175.
[46] G.J. McIntyre, The geometry of X-ray diffraction from extended face single crystals, Acta Crystallogr. Sect. A. A37 (1981) 105–119.
[47] R. Knepper, S.P. Baker, Coefficient of thermal expansion and biaxial elastic modulus of β phase tantalum thin films, Appl. Phys. Lett. 90 (2007) 181908. doi:10.1063/1.2734468.
[48] J.A. Thornton, D.W. Hoffman, Internal stresses in titanium, nickel, molybdenum, and tantalum films deposited by cylindrical magnetron sputtering, J. Vac. Sci. Technol. 14 (1977) 164–169.
[49] F.C. Frank, J.S. Kasper, Complex alloy structures regarded as sphere packings. II. Analysis and classification of representative structures, Acta Crystallogr. 12 (1959) 483–499. doi:10.1107/S0365110X59001499.
[50] S.L. Lee, M. Doxbeck, J. Mueller, M. Cipollo, P. Cote, Texture, structure and phase transformation in sputter beta tantalum coating, Surf. Coatings Technol. 177-178 (2004) 44–51. doi:10.1016/j.surfcoat.2003.06.008.
[51] M.T. Janish, W.M. Mook, C.B. Carter, Nucleation of fcc Ta when heating thin films, Scr. Mater. 96 (2015) 21–24. doi:10.1016/j.scriptamat.2014.10.010.
[52] D. Dorranian, E. Solati, M. Hantezadeh, M. Ghoranneviss, A. Sari, Effects of low temperature on the characteristics of tantalum thin films, Vacuum. 86 (2011) 51–55. doi:10.1016/j.vacuum.2011.04.012.
[53] D.W. Hoffman, J.A. Thornton, Effects of substrate orientation and rotation on internal stresses in sputtered metal films, J. Vac. Sci. Technol. 16 (1979) 134. doi:10.1116/1.569886.
[54] A. Roth, Vacuum Technology, 3rd ed., Elsevier Science B.V, Amsterdam, 1990.
[55] T.P. Drüsedau, M. Löhmann, F. Klabunde, T.-M. John, Investigations on energy fluxes in magnetron sputter-deposition : implications for texturing and nanoporosity of metals, Surf. Coatings Technol. 133-134 (2000) 126–130.
[56] T.P. Drüsedau, F. Klabunde, P. Veit, T. Hempel, Investigations on microstructure, surface topography, and growth process of sputtered molybdenum showing texture turnover, Phys. Status Solidi A. 161 (1997) 167.
[57] L. Kotis, M. Menyhard, A. Sulyok, G. Sáfrán, A. Zalar, J. Kovač, P. Panjan, Determination of the relative sputtering yield of carbon to tantalum by means of Auger electron spectroscopy depth profiling, Surf. Interface Anal. 41 (2009) 799–803. doi:10.1002/sia.3101.
[58] K. Wasa, S. Hayakawa, Handbook of Sputter Deposition Technology: Principles, Technology, and Applications, Park Ridge, NJ, 1992.
[59] O.K. Donaldson, K. Hattar, J.R. Trelewicz, E.I.C. Johnson, Metastable Tantalum Oxide Formation During the Devitrification of Amorphous Tantalum Thin Films, J. Am. Ceram. Soc. 99 (2016) 3775–3783. doi:10.1111/jace.14384.
[60] J.A. Thornton, Substrate Heating in Cylindrical Magnetron Sputtering Sources., Thin Solid Film. Pap Present. Int Conf Met. Coat San Fr. Calif Apr 3-7 1978. 54 (1978) 23–31. doi:10.1016/0040-6090(78)90273-0.
[61] L.A. Clevenger, A. Mutscheller, J.M.E. Harper, C. Cabral, K. Barmak, The relationship between deposition conditions, the beta to alpha phase transformation, and stress relaxation in tantalum thin films, J. Appl. Phys. 72 (1992) 4918. doi:10.1063/1.352059.
[62] F. D'Heurle, L. Berenbaum, R. Rosenberg, ., Trans. Met. Soc. AIME. 242 (1968) 502.
[63] E. Chason, A kinetic analysis of residual stress evolution in polycrystalline thin films, Thin Solid Films. 526 (2012) 1–14. doi:10.1016/j.tsf.2012.11.001.
[64] A.M. Vodnick, Stress Partitioning in FCC Thin Metal Films with Mixed Texture, (2010).
[65] D. Bernoulli, U. Müller, M. Schwarzenberger, R. Hauert, R. Spolenak, Magnetron sputter deposited tantalum and tantalum nitride thin films: An analysis of phase, hardness and composition, Thin Solid Films. 548 (2013) 157–161. doi:10.1016/j.tsf.2013.09.055.
[66] R. Saha, J.A. Barnard, Effect of structure on the mechanical properties of Ta and Ta(N)

thin films prepared by reactive DC magnetron sputtering, J. Cryst. Growth. 174 (1997) 495–500. doi:10.1016/S0022-0248(96)01148-7.
[67] Z. Zhou, Structural analysis of Co, Thin Solid Films. 339 (1999) 95–101. doi:10.1016/S0040-6090(98)01155-9.
[68] W. Ensinger, Ion bombardment effects during deposition of nitride and metal films, Surf. Coatings Technol. 99 (1998) 1–13. doi:10.1016/S0257-8972(97)00410-6.
[69] D. Dobrev, Ion-beam induced texture formation in vacuum condensed thin metal films, Thin Solid Films. 92 (1982) 41–53.
[70] R.M. Bradley, J.M.E. Harper, D.A. Smith, Theory of thin-film orientation by ion bombardment during deposition, J. Appl. Phys. 60 (1986) 4160–4164. doi:10.1063/1.337499.
[71] G.N. Van Wyk, H.J. Smith, Crystalline reorientation due to ion bombardment, Nucl. Instruments Methods. 170 (1980) 433–439. doi:10.1007/s10787-012-0152-6.
[72] H. Ma, Y. Zou, A.S. Sologubenko, R. Spolenak, Copper thin films by ion beam assisted deposition: Strong texture, superior thermal stability and enhanced hardness, Acta Mater. 98 (2015) 17–28. doi:10.1016/j.actamat.2015.07.013.
[73] Y. Yamamura, M. Ishida, Monte Carlo simulation of the thermalization of sputtered atoms and reflected atoms in the magnetron sputtering discharge, J. Vac. Sci. Technol. A Vacuum, Surfaces, Film. 13 (1995) 101. doi:10.1116/1.579874.
[74] R. Behrisch, W. Eckstein, Sputtering Yields, (2007).
[75] P. Sigmund, Elements of Sputtering Theory, in: PSP Rev., 2011: p. 4.
[76] W.D. Westwood, F.C. Livermore, Phase composition and conductivity of sputtered tantalum, Thin Solid Films. 5 (1970) 407–420. doi:10.1016/0040-6090(70)90112-4.
[77] R. Knepper, B. Stevens, S.P. Baker, Effect of oxygen on the thermomechanical behavior of tantalum thin films during the β–α phase transformation, J. Appl. Phys. (2006). doi:10.1063/1.2388742.
[78] N. Schonberg, An X-Ray Investigation of the Tantalum Oxygen System, Acta Chem. Scand. 8 (1954) 240–245. doi:10.3891/acta.chem.scand.08-0240.
[79] C.C. Huang, Y.L. Wang, S.C. Chang, G.J. Hwang, J.L. Huang, Phase transformation of tantalum on different dielectric films with plasma treatment, Thin Solid Films. 498 (2006) 286–288. doi:10.1016/j.tsf.2005.07.128.

CHAPTER 4

Effect of sputter pressure on microstructure and properties of β-Ta thin films:

Elizabeth A. I. Ellis[1], Markus Chmielus[2,3], Shangchen Han[2] and Shefford P. Baker[1,2]

1. *Cornell University, Sibley School of Mechanical and Aerospace Engineering, Upson Hall, Ithaca, NY 14853 USA*
2. *Cornell University, Department of Materials Science and Engineering, Bard Hall, Ithaca, NY 14853 USA*
2. *University of Pittsburgh, Department of Mechanical Engineering & Materials Science, Benedum Hall, Pittsburgh, PA 15261 USA*

This chapter is a draft of a paper being prepared for publication. My contribution to the work was in helping to deposit the films, taking SEM images, and analyzing results.

ABSTRACT

Tantalum thin films may be deposited in two phases. The stable bulk alpha phase is well known, but the metastable tetragonal beta phase is still relatively poorly understood. In a previous article we reported on a series of 100% β-Ta films deposited under varying sputter pressures in a low-oxygen environment, and discussed texture, stresses and phase selection in β-Ta. Here, we discuss the microstructure, morphology, and properties of these same β-Ta films. Grain size, as measured from SEM images, increases with increasing sputter pressure. Mechanical properties were measured by nanoindentation, and we found that hardness decreases with increasing grain size in accordance with the Hall-Petch relation. Comparison of indentation modulus with biaxial modulus measurements indicates that the elastic modulus of the β phase is anisotropic, and likely to be higher in the [002] direction. Finally, a representative resistivity value of 169 ± 5 $\mu\Omega$cm is reported for the first time for virtually oxygen-free, 100% β-Ta films.

4.1. INTRODUCTION

Tantalum thin films are widely used in industry and therefore widely studied in literature (e.g. [1–10]). Until recently, however, there has been greater interest in the stable BCC form of tantalum than in the metastable β phase that appears only in thin films. The two phases are quite different, and are therefore suited to different applications. While α-Ta films are widely used in applications such as wear-resistant coatings and diffusion barriers for Cu-Si interconnects, β-Ta has generally been desired only for Ta thin film resistors. However, the recent discovery of a giant spin Hall effect in β-Ta may be important for the development of next-generation magnetoresistive memory technologies [11], and has renewed interest in this phase.

Because α-Ta has been the preferred phase for many years, relatively little is known about the structure and properties of β-Ta films. It is well-known that β-Ta has a high electrical resistivity compared to the conductive α phase, but reported values vary widely, from 112 $\mu\Omega$cm [9] to 1500 $\mu\Omega$cm [8]. The origins of these variations are unknown, but they have been attributed to included α-Ta [10], grain size [8], and oxygen content [12] in the films. Similarly, hardness has been reported to vary from ~12 GPa [3] to ~20 GPa [6] with variations attributed to stresses [3], strain rate [4,6] and grain size [5]. While there are few reports of elastic properties, Young's modulus has been reported to be as high as 194 GPa [5] or, improbably, to vary with grain size and texture over the range 166-183 GPa [4]. Of course, properties are expected to depend intimately on structure and composition, but because systematic studies of pure β-Ta films are rare, the literature on these β-Ta properties remains fragmentary and the actual correlations between composition, structure, and properties are unknown. One reason for this is that Ta films have been produced on a variety of different substrates, using a wide range of deposition parameters, and including a number of different impurities.

To explore synthesis-structure-properties relationships more systematically, we prepared a set of β-Ta thin films by sputtering in an ultra-high-vacuum system with sputter gas pressure, p_{Ar}, ranging from 0.3 to 2.2 Pa while holding other deposition parameters constant and taking steps to minimize impurites. In a previous article [13], we reported that the stresses varied dramatically,

from -1360 to 1140 GPa over this pressure range and that the resulting x-ray diffraction (XRD) peak shifts allowed us to show that the films were virtually 100% β-Ta with a single (002) fiber texture component that broadens significantly with p_{Ar}. These results, combined with an analysis of the distributions of energy and incident angle of species arriving at the substrate allowed us to propose a new model for phase selection in Ta films that explains virtually all findings to date.

In the present article, we report on the microstructure, morphology, and properties of these films. By carefully controlling the deposition environment to ensure that all films are pure β Ta, we are able to provide a more thorough understanding of the mechanical properties of the β phase, and to provide, for the first time, a representative value of the resistivity of β-Ta films with neither α-Ta content nor oxygen contamination.

4.2. EXPERIMENTS AND RESULTS

A series of seven β-Ta films were deposited under a range of sputter pressures from 0.3 to 2.2 Pa. Microstructure was characterized using SEM, mechanical properties were measured using nanoindentation, and resistivity was measured using a four-point probe.

4.2.1. Film deposition, stresses, phase, and texture

Film deposition, phase, and texture are described in detail elsewhere [13]. Briefly, β-Ta thin films were produced by DC magnetron sputtering from a 99.95% pure Ta target in a custom ultra-high vacuum deposition chamber [14] at each of 7 selected Ar sputter gas pressures, p_{Ar}, from 0.3 to 2.2 Pa (2 to 16 mTorr). Substrates were (100) Si wafers with native oxide, 100 mm in diameter and 525 μm thick. Efforts were made to minimize the effects of impurities, particularly oxygen content. The base pressure was 2.7×10^{-6} Pa (2×10^{-8} Torr) or better. The working gas was 99.999% pure Ar that was additionally filtered to reduce oxygen content to less than 1 ppb. Before deposition, substrates were plasma cleaned for 1 min using a 25 W RF bias in 1.1 Pa Ar to remove adsorbed water or other impurities. p_{Ar} was then set to the desired value and the target was cleaned by presputtering using a magnetron gun operated in DC mode at 400 W for 5 min

onto a closed shutter. The shutter was then opened to deposit a Ta film to a nominal thickness of 500–600 nm.

Stresses in the as-deposited films were calculated from measurements of substrate curvature and were found to vary from -1360 to 1140 MPa as p_{Ar} increased [12]. Phase and texture were characterized using x-ray diffraction [13] with x-rays from a conventional Cu K_α source. Symmetric θ-2θ scans were conducted over the range $20^\circ \leq 2\theta \leq 80^\circ$. Many small peaks close to the nominal locations in the powder diffraction files (Inorganic Crystal Structure Database Collection Codes 53793 and 280872) were found, but by tracking their positions with p_{Ar}, and therefore stress, it was possible to assign all of them unambiguously to β-Ta [1]. Rocking curves of the (002) β-Ta peak were performed in the ω geometry by setting the diffractometer to the 2θ angle of the (002) β-Ta peak and rotating the scattering vector from -15° to +15° from the substrate normal in the diffraction plane. The full width at half maximum (FWHM) of the rocking curves increases from 6° to > 30° as the peak height drops across the pressure range. Analysis of these curves [1] showed that nearly all grains are oriented with [002] near the surface normal while the orientation distribution widens with p_{Ar}, i.e. films have broadening (002) fiber texture. A very minor fraction (≈ 0.1 vol%) of (410) is the only orientation detected that could not be attributed to the (002) texture component.

4.2.2. Film geometry and structure

For the present study, high-resolution micrographs of the sample surfaces and cross sections were produced using scanning electron microscopy (SEM). Cross section images were obtained by viewing the fractured film surface created when cleaving samples into smaller pieces for analysis. Sample thicknesses were obtained from the cross-section images. For samples produced with $p_{Ar} = 0.3$, 0.5, and 1.1 Pa, thicknesses were also determined using Rutherford backscattered spectrometry (RBS) and the RUMP analysis and simulation software. These samples were used to calibrate the SEM thicknesses.

Figure 4.1 shows SEM micrographs of film surfaces (left) and cross sections (right). Film thicknesses range from 485 to 644 nm (see Table 1). Distinct domed features are visible at the film surface, and the size of these features (in plan view) increases with p_{Ar}. At low p_{Ar} (*e.g.* 0.5 and 1.1 Pa), these surface features appear long and worm-like, while at higher p_{Ar} (e.g. 2.0 and 2.2 Pa) the features appear only slightly elongated. Film cross-sections show that the grain structure is columnar.

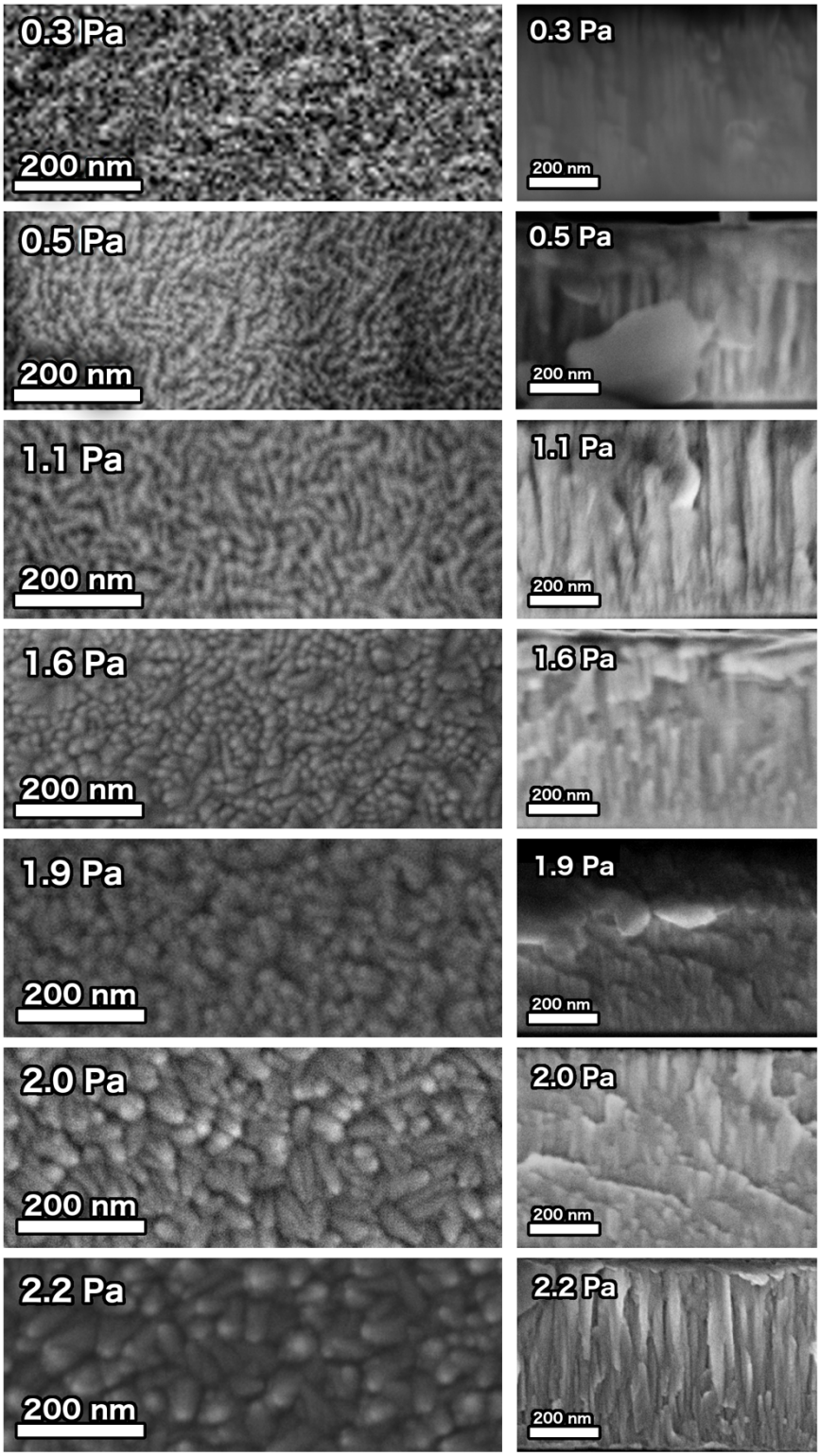

Figure 4.1: SEM micrographs of β-Ta films deposited at different sputter pressures. Left: plan view surface images. Right: cross sections of films made by viewing side of cleaved samples.

We used a modified intercept method (based on ASTM E112) to calculate feature size from the plan view SEM images. We counted intercepts (boundaries between features) along 20 randomly oriented lines for each film, with about 20 intercepts per line, using lines of different orientations to average out feature anisotropy. Figure 4.2 shows this estimate of feature size *vs.* p_{Ar}. As discussed below, the feature size can be assumed to correspond to the grain size. By this measure, grain size increases from 22.5 ± 3.5 nm to 49.2 ± 9.7 nm with increasing sputter pressure. Structural features of the films are summarized in Table 1.

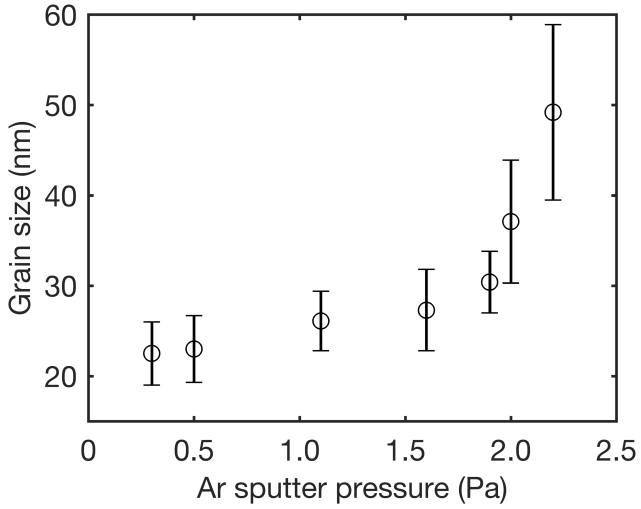

Figure 4.2: Grain size (as determined by line intercept method) of β-Ta films vs. Ar sputter pressure.

4.2.2 Resistivity

Sheet resistivity was measured 30 mm from the edge of the substrate using a four-point probe with an inner probe spacing of 1.6 mm and an outer probe spacing of 4.8 mm. Film resistivity was then calculated by multiplying by the measured film thickness. The results are shown in Figure 4.3 The average resistivity value is 169 ± 5$\mu\Omega$cm and does not vary with p_{Ar}.

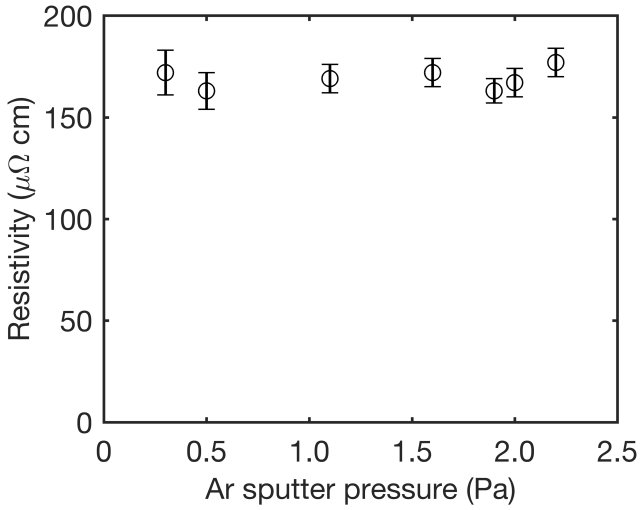

Figure 4.3: Resistivity (mean and standard deviation of 7 measurements) of β-Ta films vs. sputter pressure. Resistivity is not sensitive to p_{Ar} over this range.

4.2.3. Mechanical Properties

A scanning nanoindenter (Hysitron TriboIndenter 900) with a Berkovich tip was used to determine the mechanical properties of the films. Before testing, tip shape and machine compliance calibrations were made using a vitreous silica sample following the Oliver and Pharr (O&P) method [3]. To find a range where indentations were large enough to avoid surface effects such as roughness, yet small enough to avoid effects due to the substrate, 64 indentations were made with peak loads distributed from 1 to 10 mN so as to produce roughly equal indentation depth spacings. For each indentation, the load was ramped up linearly over 5 s, held constant for 10 s, and then removed in 5 s. The hardness, H, and the indentation modulus, E_{ind}, nominally representing $E/(1-\nu^2)$, where E and ν are the Young modulus and Poisson ratio of the tested material, were extracted from the load-depth data from each indentation using the Oliver & Pharr method [15]. After correcting for machine compliance, a power law was fitted to the unloading data from 20 to 95% of the maximum load, P_{max}, and the slope of the fit at P_{max} was taken to be the contact stiffness, S. The contact depth, h_c, which is the distance along the indenter axis that the film material was in contact with the indenter at P_{max} is then given by

$$h_c = h_{max} - 0.72(P_{max}/S) \quad (1)$$

where h_{max} is the depth at maximum load.

Figure 4.4 shows the calculated hardness and indentation modulus of the film made at 0.3 Pa *vs*. contact depth. Surface effects are visible in the hardness below about 25 nm, but hardness is roughly constant above 25 nm. The elastically deformed region is much larger than the plastic region [16], so E_{ind} decreases as $\underline{h_c}$ increases due to the influence of the substrate (E_{ind} for Si is ≈ 178.6 GPa [17]). To avoid surface effects and minimize the influence of the substrate, we averaged properties from measurements with contact depths of 40 - 60 nm from each sample to obtain an average hardness and indentation modulus value for each sample.

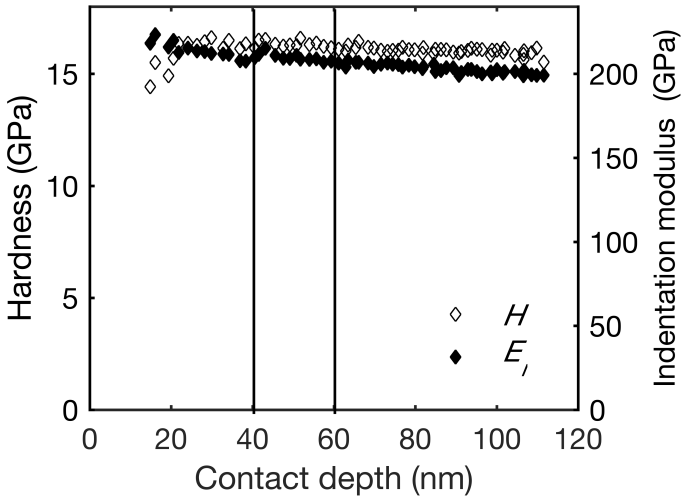

Figure 4.4: Hardness and indentation modulus vs. contact depth for the film deposited at 0.3 Pa. Indentations with 40 ≤ h_c ≤ 60 nm were large enough to avoid surface effects while minimizing the influence of the substrate.

Figures 4.5a and 4.5b show the averaged H and E_{ind} values, respectively, of the Ta thin films as a function of p_{Ar}. The hardness decreases continuously with increasing sputter pressure from 16.4 GPa to 11.3 GPa, while the indentation modulus is ~209 GPa independent of p_{Ar} for samples deposited at lower pressures, but decreases with increasing p_{Ar} above p_{Ar} ≈ 1.6 Pa. Scatter in both H and E_{ind} increases with p_{Ar}.

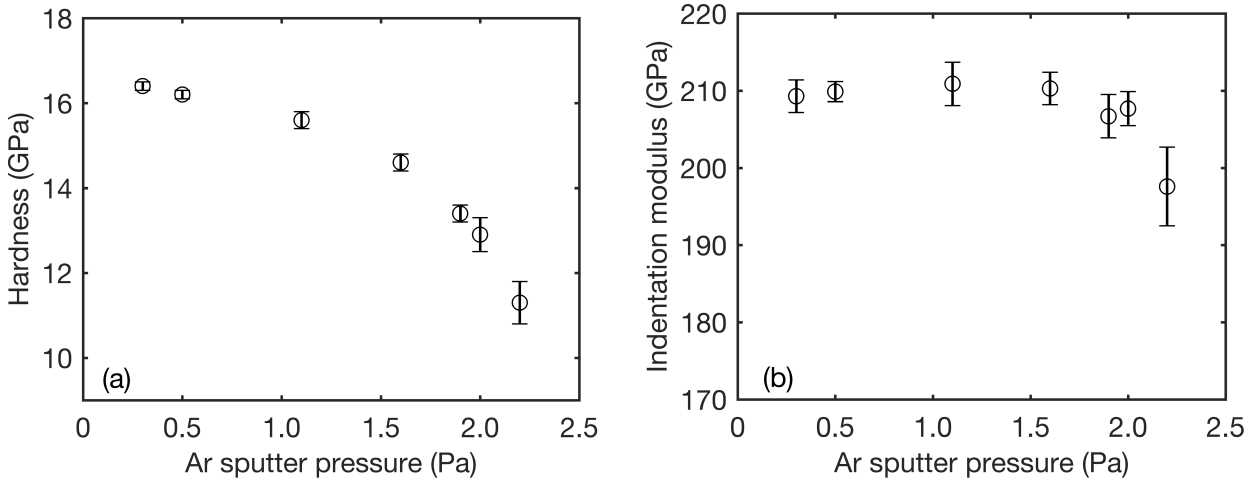

Figure 4.5: (a) Hardness and (b) indentation modulus (mean and standard deviation of ≈ 10 measurements with contact depths between 40 nm and 60 nm for each value in each sample) vs. sputter pressure. H decreases with increasing p_{Ar}, while E_{ind} is insensitive to p_{Ar} at low pressures, but drops slightly for the films deposited with p > 1.6 Pa.

The indenter was also used as an imaging probe in surface force microscopy mode with an imaging force of 2 μN to obtain the surface topography of the 0.3 and 2.2 Pa samples to investigate possible pile-up around the edges of the indentations. Pileup height scaled with indentation load and was difficult to measure for small indentations. However, for indentations made to 160 nm depth, pileup height was ~8 and ~9 nm for the films deposited at 0.3 and 2.2 Pa, respectively. Since the resolution of these measurements is ~1 nm, so pileup height may be considered to be independent of p_{Ar}.

To test for strain rate sensitivity effects, indentions were made to 10 mN at rates that varied from 0.5 to 20 mN/s. This load was held until the indenter stopped moving (displacement rate approached measured drift rate) and the indenter was then unloaded at 2 mN/s. Unloading data were analyzed using the O&P method as described above. No variations in hardness or modulus with load rate could be detected.

Table 5.1: Summary of film deposition parameters and properties.

p_{Ar}		Thickness	FWHM rocking	Stress	Grain size	Hardness	E_{ind}	ϱ
[Pa]	[mTorr]	[nm]	[°]	[MPa]	[nm]	[GPa]	[GPa]	[$\mu\ \Omega$cm]
0.3	2	485	5.43	-1358	22.5±3.5	16.4±0.1	209.3±2.1	172±11
0.5	4	505	5.73	-1045	23.0±3.7	16.2±0.1	209.9±1.3	163±9
1.1	8	601	7.61	-641	26.1±3.3	15.6±0.2	210.9±2.8	169±7
1.6	12	611	11.27	-216	27.3±4.5	14.6±0.2	210.3±2.1	172±7
1.9	14	616	16.09	179	30.4±3.4	13.4±0.2	206.7±2.8	163±6
2.0	15	644	24.66	544	37.1±6.8	12.9±0.4	207.7±2.2	167±7
2.2	16	638	30.26	1149	49.2±9.7	11.3±0.5	197.6±5.1	177±7

4.3. DISCUSSION

By varying p_{Ar} while carefully minimizing other sources of variation we obtain a series of virtually 100% β-Ta films with systematic variations in microstructure, allowing us to provide accurate and representative measurements of the properties of the β-Ta phase.

4.3.1 Effect of sputter pressure on microstructure

As is evident in Fig. 4.1, the grain structure in all of these β-Ta films is columnar. In principle, the elongated surface features at low p_{Ar} could represent either the tops of elongated grains or clusters of small equiaxed (in the film plane) grains. Such elongated features in as-deposited β-Ta films have been reported [18], however, plan view TEM images of β-Ta films invariably show that the grains are equiaxed in the film plane [4–6,19,20], suggesting that each elongated feature is comprised of several individual grains. This is supported by the film deposited at p_{Ar} = 1.6 Pa where roughly equiaxed features, which we take to be grains, are arranged into rows reminiscent of the worm-like surface features in films made at lower p_{Ar}. At higher pressures, it is clear that the surface features represent individual grains. For this reason, we treat the feature size as the grain size in Fig. 4.2. While the fracture surfaces in Fig. 4.1 are too uneven for statistical analysis, the widths of the measurable columnar features in the high sputter pressure films agree with the grain sizes (Fig. 4.2) obtained from the surface features. We therefore assume that at all pressures we have columnar, (002)-oriented grains that are approximately

equiaxed in the plane of the film. As p_{Ar} increases, the grain size increases and the (002) texture distribution widens somewhat.

The primary means by which p_{Ar} affects thin film structure and properties is through changes in the energies and incident angles of bombarding particles at the substrate caused by collisions with inert gas atoms [1]. These effects are well described by "structure zone models," [21] in which the resulting microstructures are mapped out in terms of sputter pressure and homologous substrate temperature, T/T_M, where T_M is the melting point of the film material. These microstructures are divided into four "zones." Zone 1, at low T/T_M and high p_{Ar}, is dominated by atomic shadowing processes, in which surface features prevent material from reaching certain areas of the growing film, and features crystals with high dislocation densities, domed tops, and open, voided, or low-density grain boundaries. Zone 2, at moderate T/T_M and all p_{Ar}, features columnar grains without voids at grain boundaries. Zone 3, at high T/T_M and all p_{Ar}, is dominated by diffusion and features equiaxed grains. Zone T is a transition zone between zones 1 and 2, especially prominent at low sputter pressure, and features highly dislocated crystals with dense boundaries.

According to this model [21], the effects of pressure should be observed primarily in the low-temperature regime, in the transition from Zone 1 to Zone T. As β-Ta is a metastable phase, its melting temperature is not defined, but our deposition temperature of 90°C is low compared to the melting point of α-Ta (3017°C), so we therefore expect our microstructures to be in this regime. Indeed, the columnar grains and domed tops in Figure 4.1 are consistent with this model. The model also predicts that at sufficiently high p_{Ar}, sputtered films may start to incorporate voids at grain boundaries [21]. Indeed, such voids have been seen in Cr films sputtered under similar conditions [22]. We have no evidence that such voids are present in our films, but cannot rule them out completely.

We see an additional effect of sputter pressure that has not been identified in structure zone models: Namely, that grain size increases with sputter pressure. Similar grain size effects have been observed in Cr [22], but no explanation was proposed. We attribute the grain size increase

to the decrease in energy of the species incident at the substrate due to increasingly frequent collisions with inert gas atoms [1], which leads to a decrease in nucleation rate since higher-energy adatoms are better able to rearrange previously deposited material into stable, favorably oriented nuclei [23]. Previously [13] we proposed a resputtering mechanism to explain the texture broadening that occurs with increasing sputter pressure, wherein less well-oriented grains are preferentially resputtered at lower sputter pressures. These two energy effects—increased nucleation and increased resputtering—are similar in that both result in more favorably-oriented nuclei. Both of these processes are therefore consistent with our observation of increased grain size and increased texture broadening with increasing sputter pressure.

4.3.2 Resistivity

We observe essentially no change in resistivity over the entire sputter pressure range, despite significant differences in film microstructure. This indicates that the electron mean free path is shorter than the smallest grain size [24]. A simple estimate of the electron mean free path may be calculated from the measured resistivity, atomic mass, and density of the material [25], and for these films is approximately 3.8 Å, on the same order as the interatomic spacing in β-Ta [26] and considerably shorter than the shortest apparent grain diameter.

Other researchers, however, have found that increasing sputter pressure leads to an increase in resistivity [27–29], with a threshold pressure between ~1 Pa [27] and ~2.6 Pa [29]. This resistivity increase is attributed to the increase in grain boundary voids predicted by the structure zone model, and open spaces between grain boundaries are indeed visible in some of the high-pressure films reported in these works [27]. The insensitivity of our film resistivities to sputter pressure may therefore indicate that void density is negligible in the films reported here, though it is possible for voids to be configured so as to have negligible effect on resistivity [30].

As noted in the Introduction, reported resistivity values for the β phase vary widely. We attribute this variation to two main sources of error: mixed phase and oxygen impurities. In reviewing the resistivity literature, we find that very low resistivity values tend to be associated

with mixed phase, as films with mixed α and β phase are common, but it can be quite difficult to determine this using only symmetric θ-2θ XRD scans [13]. As the resistivity of the α phase is much lower, a small amount of α-Ta in a film can dramatically reduce its measured resistivity. For example, Sosniak *et al*. observed up to 15% alpha Ta in some samples, but still report resistivities for "β-Ta films" of 112 $\mu\Omega$cm [9]. Similarly, Senkevich *et al*. report resistivities of 130-160 $\mu\Omega$cm for β-Ta despite the acknowledged presence of small α peaks visible in XRD of films identified as β [31].

Extremely high resistivity values, on the other hand, are associated with oxygen contamination. Tantalum reacts readily with oxygen, and small amounts of incorporated oxygen can have dramatic effects on film properties [32]. Specifically, oxygen-contaminated Ta has much higher resistivity than either α-Ta or β-Ta [33]. While it is difficult to demonstrate conclusively that a particular film reported in literature contains oxygen, there are nonetheless several indications that oxygen effects are present. For example, Clevenger *et al*. report resistivities of 225-250 $\mu\Omega$cm [7], but also observe that their films do not begin to transform to the stable α phase until about 700°C. This transformation behavior looks remarkably like the behavior of β-Ta films with significant oxygen content [32]. Similarly, Solati et. al report resistivities of 600-1500 $\mu\Omega$cm, but used a base pressure only 4×10^{-4} Torr [8]. Assuming oxygen is present in a similar ratio as in the atmosphere, this leaves an oxygen partial pressure of about 8×10^{-5} Torr, well within the range shown to affect resistivity [33].

By performing careful phase identification [13] and exercising special care to avoid oxygen, we are able to avoid both of these pitfalls in resistivity measurement. Our resistivity value is higher than those of films known to contain α-Ta, and lower than those likely to contain significant oxygen. It is of course possible to obtain resistivity values near ours by having both α-Ta content and oxygen contamination, but we believe we have provided the first representative resistivity value for β-Ta that contains neither α-Ta nor significant oxygen contamination.

4.3.3 Mechanical Properties

The hardness and modulus behavior shown in Fig. 4.5 can be explained in terms of the variation in microstructure of the β-Ta films with p_{Ar}.

4.3.3.1 Hardness

As shown in Fig. 4.5a, the hardness of the β-Ta films ranges from 16.4 to 11.3 GPa over the sputter pressure range tested. In comparison, hardness values for α-Ta films are typically in the range of 10.2 GPa to 11.6 GPa [18,34,35]. Similarly, other BCC metal films show hardnesses of about 8 to 12 GPa [34]. Some of the increased hardness we observe in β-Ta may be due to the small grain sizes in the films deposited at low sputter pressures. Figure 4.6 shows hardness plotted *vs*. the reciprocal square root grain size (from Fig. 4.2), *i.e*. a modified Hall-Petch plot featuring hardness rather than strength. The values fall on a straight line, in accord with the Hall-Petch relationship,

$$H = H_0 + \frac{k_{HP}}{\sqrt{d}} \quad , \tag{2}$$

where k_{HP} = 76 GPa nm$^{1/2}$ is the Hall-Petch coefficient and H_0 = 0.33 GPa is the strength in the absence of grain boundaries. There do not appear to be any measurements of Hall-Petch constants for β-Ta or similar metals such as β-U or β-W, but we are able to compare with α-Ta and other BCC metals. Cordero *et al*. [36] compiled grain boundary strengthening data from V, Nb, Ta, Cr, Mo, W and Fe, measured using both hardness testing and tension/compression testing, and used a Tabor factor of 3 to convert between hardness and yield strength measurements. They then fit these data to a Hall-Petch plot, and report coefficients between 310 (Fe) and 1000 (W) MPa μm$^{1/2}$ (9.8 – 31.6 GPa nm$^{1/2}$). A-Ta has a coefficient of 760 MPa μm$^{1/2}$ (24.1 GPa nm$^{1/2}$). Using the same Tabor factor of 3 to convert our hardness values, we find a Hall-Petch coefficient of 800 MPa μm$^{1/2}$ (25 GPa nm$^{1/2}$) for our β-Ta films, higher than the α-Ta coefficient but within the range of similar metals.

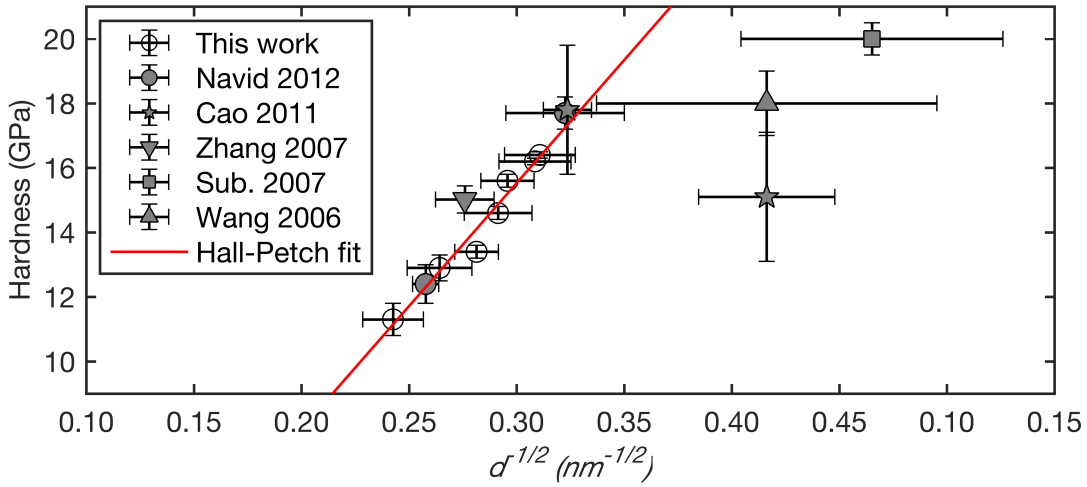

Figure 4.6: Hall-Petch analysis of hardness data from Fig. 4. 4: hardness increases linearly with reciprocal of the square root of grain size with slope 76 GPa nm$^{1/2}$ (Hall-Petch coefficient), intercept 0.33 GPa (single crystal strength), and coefficient of determination R^2 = 0.97. Also shown: hardness vs. grain size data from Navid et al. [18], Cao et al. [4], Zhang et al. [5], Subrahmanyam et al. [35], and Wang et al. [6].

In Fig. 4.6, we have also included data from other studies where films were reported to consist of the β phase and for which both hardness and grain size were reported. Navid *et al.* [18] reported hardnesses from Ta films deposited using sputter gas pressures p_{Ar} from 0.3 to 1.4 Pa. The phase composition of their films varied (a feature attributed to impurities [13]) resulting in a nonmonotonic variation of H with p_{Ar}. Only the films deposited at 0.3 and 0.4 Pa were found to be 100% β-Ta. We recalculated the grain sizes for these two films from their data using the method described in Section 2.1, as their reported grain sizes seem to have been mismeasured [18]. Their corrected results agree very well with ours (Fig. 4.6). Zhang *et al.* [5] also report hardness and grain size for a film that is very close to, but slightly above, our Hall-Petch fit.

Others' results do not fall on the same Hall-Petch line. Wang *et al.* [6] and Cao *et al.* [4,19,20] conducted nanoindentation experiments in which hardness values were calculated from load-displacement data obtained at different load rates and reported that load rate significantly affected hardness [4,6]. For example, Cao *et al.* [4] made indentations in which load was ramped up to and back down from a maximum load of 9.8 μN at fixed rates between 0.098 μN/s and 9.8 μN/s *without any hold* at the maximum load. In previous work [19], they had shown that if the indenter were simply held at the maximum load, a significant amount of time-dependent plastic

deformation would occur. It is well known that in such cases, unloading before ongoing plastic deformation is complete can cause significant errors in both hardness and modulus values obtained from an Oliver and Pharr analysis [37], and the variations reported by both groups [4,6] are consistent with such artifacts. In our experiments, with a 10 s hold at maximum load, we did not see any evidence of rate effects on hardness. Wang *et al*. [6] provide no details of their nanoindentation experiments, so it is difficult to evaluate their results.

To include data from Wang *et al*. [6] and Cao *et al*. [4] in Fig 4.6, we averaged their results from measurements with loading rates between 0.2 and 50 mN/s. Most of these data do not fall on our Hall-Petch curve. Indeed, Cao *et al*. [4] show increasing hardness with grain size. Such reverse Hall-Petch behavior has been reported to occur at small grain sizes in other metals [38] and may be a factor here. Subrahmanyam *et al*. [35] report a hardness of about 20 GPa (no reported error) in a film with very small grains. However, no details of their nanoindentation measurements are given, so these values are difficult to interpret.

Interestingly, Wang *et al*. [6] conducted post-mortem TEM analysis and reported that some of the material in the plastic zone immediately under the indenter had transformed from the beta phase to the alpha phase, in the film indented at 5000 μN/s. Since the phase transformation has been shown to be diffusional in nature [32], such a phase transformation could be responsible for the time dependent behavior reported by Cao *et al*. [4]. This suggests that the β-α phase transformation may play a role in all of the reported hardnesses. Further study of this would be worthwhile.

In principle, there are three other factors that could contribute to the variation in H with p_{Ar}: stresses, anisotropy, and grain boundary voids. Stresses are known to affect hardness and modulus values calculated using the O&P method [39], and the measured stress changes across the pressure range in our films are enormous (Table 1). However, it has also been convincingly demonstrated that such stress-related hardness and modulus variations are artifacts resulting from pileup [40,41]. Since the measured pileup in our films did not change with p_{Ar}, we assume that the changes in hardness with p_{Ar} (Fig. 4.5a) are not caused by stress.

Cursory inspection of the crystal structure of β-Ta (space group P-42_1m) suggests that the (002) planes might be the only candidates for low-Peierls-stress slip systems, leading to high plastic anisotropy. Since the orientation distribution broadens with p_{Ar}, one could imagine this anisotropy contributing to the variations in H with p_{Ar}. However, we doubt this explanation because indentation deformation is well averaged over all directions [42] and, except for special cases where slip systems and indentation faces are well aligned [43], even significant plastic anisotropy leads to small variations in hardness—for example the maximum variation with orientation in Berkovich indentation of HCP Zn is ~ 20% [42]. Furthermore, it is not evident why variations in H with p_{Ar} due to anisotropy should follow a $1/\sqrt{}$(grain size) dependence.

Finally, we note that voids at grain boundaries, if present, could affect mechanical properties. An increasing void fraction could lower hardness and modulus without significantly affecting resistivity [30] —qualitatively consistent with our results in Fig's 4.3 and 4.5. While we can't rule out such effects entirely, we note that we have no direct evidence for the existence of such voids, nor an argument why variations in H with p_{Ar} due to voids should follow a $1/\sqrt{}$(grain size) dependence.

The scatter in the hardness values (and in E_{ind}) increases systematically with p_{Ar}. Since, even for the largest grain sizes, the indenter is in direct contact with a few dozen grains at maximum load, this seems unlikely to be associated with any inhomogeneity in the sample. Rather, we attribute this to the surface topography. Although the load series results (*e.g.* Fig. 4.4) show that the peak to peak roughness does not change significantly with p_{Ar}, the in-plane spacing of the roughness changes with the grain size. As is evident in the film made at p_{Ar} = 2.2 Pa in Fig. 4.1, although the average grain size is much smaller, there are regions where the spacing between the highest points on the tops of the domed grains is 100-200 nm. This corresponds well with the tip radius of ~ 120 nm. Thus, indentations that land on/between groups of grain peaks will have contact areas that are slightly lower/higher than average, leading to increasing scatter.

3.3.2 Indentation Modulus

The variations in indentation modulus shown in Fig. 4.5b are smaller than the variations in hardness (6% *vs*. 30%) and affect only the samples deposited at higher p_{Ar}. As with hardness, we rule out stress effects because pileup is constant across the sputter pressure range [40,41]. We also continue to neglect the possibility of grain boundary voids at higher p_{Ar} [21], both because we have no direct evidence of their existence and because the excellent Hall-Petch correlation (Fig 4.6) restricts their configurations to those consistent with a 1/√(grain size) dependence. Instead, we focus on anisotropy effects as a possible cause of these variations.

We can assess anisotropy effects by comparing the indentation modulus of our films to the biaxial modulus of nominally identical films measured by substrate curvature as reported by Knepper *et al*. [44]. Knepper *et al's* films were deposited in the same system using the same procedure described in Section 2, with a sputter pressure of 1.1 Pa Ar. When measured by substrate curvature, those films had a biaxial modulus $Y = 175 \pm 20$ GPa. For an isotropic material $Y = E/(1 - \nu)$ and $E_{ind} = E/(1 - \nu^2)$, so $Y = E_{ind}(1 - \nu^2)/(1 - \nu)$. Using $E_{ind} = 210.9$ GPa (the value for our 1.1 Pa film) and $\nu = 0.3$, we find that if the material were isotropic, we would expect to find $Y = 274$ GPa based on our nanoindenter results. Since the microstructure and composition of these two films are unlikely to be different, we conclude the difference is the result of anisotropy. Since Y represents in-plane stiffness components while E_{ind} represents some average over all directions [16], and because these films have strong (002) texture, this discrepancy in modulus values suggests that stiffness along the [002] direction is considerably higher than in the (002) plane. This is consistent with the findings of Arakcheeva, who reports that interatomic distances are approximately 7% shorter in the [002] direction than in any other direction, due to the position of Ta atoms along the [002] channels of the structure [26]. As interatomic spacing is a strong indicator of stiffness [45], this decreased interatomic spacing could contribute to increased stiffness along the [002] direction. The decrease in E_{ind} with p_{Ar} would reflect this anisotropy because of the pronounced texture broadening that occurs with

increased p_{Ar}, (Table 1). As explained above, hardness is not affected by anisotropy to the same degree as modulus.

Modulus is rarely reported for β-Ta. Zhang reports Young's modulus = 193.87 ± 7.40 GPa [5], but without specifying the Poisson ratio or indenter properties used to calculate this value. If we assume $\nu = 0.3$ and calculate Young's modulus from our E_{ind} value, we find $E = 189 \pm 2$ GPa, in good agreement with Zhang. Both values are from films with some degree of (002) texture, so high E compared to biaxial modulus in both cases is consistent with our assertion that the [002] direction in β-Ta is stiffer than other directions. Saha *et al*. [46] report Young's moduli between about 140 GPa and 250 GPa for β-Ta, but their results seem dominated by substrate effects. In comparison, nanoindentation modulus data of α-Ta films shows Young's moduli between 205 and 220 GPa [47], noticeably higher than our calculated Young's modulus value for β-Ta. This is consistent with a past study of biaxial moduli in α- and β-Ta, which reported that the biaxial modulus of α-Ta films was more than 50% higher than that of β-Ta films [48]. Similarly, the average interatomic spacing is significantly longer in β-Ta (average 2.93 Å [26]) than in α-Ta (2.33 Å, calculated from [49]), which should correspond to a decrease in stiffness [45].

4.3.4 The nature of the β-Ta phase

A summary of the properties of β-Ta reveals a number of seemingly non-metallic features: The β phase has high resistivity, a negative temperature coefficient of resistance [50], which is not typically associated with metals [51], a complex crystal structure, is brittle, and has a high Hall-Petch constant. We might therefore think of β-Ta as a metalloid, rather than a metallic phase. This would be similar to the case of grey and white tin, where both are allotropes of pure tin, but white tin is metallic while grey tin is a metalloid [52]. This calls for further investigation into the nature of bonding in β-Ta, and whether there may be covalent character present in the atomic bonding of β-Ta that may be responsible for its unusual metalloid-like properties.

4.4. SUMMARY AND CONCLUSIONS

A series of β-Ta films were deposited under sputter pressures from 0.3 to 2.2 Pa. By carefully controlling the deposition environment, we were able to produce a range of virtually 100% β-Ta films with wide variations in microstructure and properties. Grain size increases from 22.5 ± 3.5 nm to 49.2 ± 9.7 nm with increasing sputter pressure.

We used nanoindentation to measure mechanical properties and found hardnesses vary from 16.4 to 11.3 GPa, and that, when data from others are included, the variation in hardness is consistent with Hall-Petch behavior. In broad terms, the structures, stresses, grain sizes, and hardnesses are similar across many studies, and show that beta is significantly harder than alpha.

Indentation modulus is about 209 GPa and is anisotropic, with the modulus in the [002] direction considerably higher than on other directions. We have obtained a representative value for the resistivity of pure β-Ta of 169 ± 5 $\mu\Omega$cm. We also suggest that the unusual metalloid-like properties of the β phase might indicate some degree of covalent bonding in the β-Ta structure.

4.5. ACKNOWLEDGMENTS

Support for this work was provided by the National Science Foundation (DMR 0706507 and DMR 1106223). This work also made use of the facilities of the Cornell Center for Materials Research with support from the National Science Foundation Materials Research Science and Engineering Centers program (DMR 1120296). We also thank Hysitron, Inc. for providing the nanoindenter used in these experiments.

4.6. REFERENCES

[1] M.H. Read, C. Altman, A new structure in tantalum thin films, Appl. Phys. Lett. (1965).
[2] W.D. Westwood, F.C. Livermore, Phase composition and conductivity of sputtered tantalum, Thin Solid Films. (1970). doi:10.1016/0040-6090(70)90112-4.
[3] A.A. Navid, A.M. Hodge, Nanostructured alpha and beta tantalum formation—Relationship between plasma parameters and microstructure, Mater. Sci. Eng. A. 536 (2012) 49–56. doi:10.1016/j.msea.2011.12.017.
[4] Z. Cao, Q. She, Y. Huang, X. Meng, The rate sensitivity and plastic deformation of nanocrystalline tantalum films at nanoscale, Nanoscale Res. Lett. 6 (2011) 2–7. doi:10.1186/1556-276X-6-186.
[5] M. Zhang, Y.F. Zhang, P.D. Rack, M.K. Miller, T.G. Nieh, Nanocrystalline tetragonal tantalum thin films, Scr. Mater. 57 (2007) 1032–1035. doi:10.1016/j.scriptamat.2007.07.041.
[6] Y.M. Wang, A.M. Hodge, P.M. Bythrow, T.W. Barbee, A. V. Hamza, Negative strain rate sensitivity in ultrahigh-strength nanocrystalline tantalum, Appl. Phys. Lett. 89 (2006) 2004–2007. doi:10.1063/1.2338006.
[7] L.A. Clevenger, A. Mutscheller, J.M.E. Harper, C. Cabral, K. Barmak, The relationship between deposition conditions, the beta to alpha phase transformation, and stress relaxation in tantalum thin films, J. Appl. Phys. 72 (1992) 4918. doi:10.1063/1.352059.
[8] E. Solati, D. Dorranian, Investigation of the Structure and Properties of Nanoscale Grain-Size β-Tantalum Thin Films, Mol. Cryst. Liq. Cryst. 571 (2013) 67–76. doi:10.1080/15421406.2012.741347.
[9] J. Sosniak, W.J. Polito, G.A. Rozgonyi, Effect of Background-Gas Impurities on the Formation of Sputtered β-Tantalum Films, J. Appl. Phys. (1967). doi:10.1063/1.1710059.
[10] J.J. Senkevich, T. Karabacak, D.-L. Bae, T.S. Cale, Formation of body-centered-cubic tantalum via sputtering on low-$\varkappa$ dielectrics at low temperatures, J. Vac. Sci. Technol. B Microelectron. Nanom. Struct. 24 (2006) 534. doi:10.1116/1.2166860.
[11] L. Liu, C.-F. Pai, Y. Li, H.W. Tseng, D.C. Ralph, R.A. Buhrman, Spin-Torque Switching with the Giant Spin Hall Effect of Tantalum, Science (80-.). 336 (2012) 555–558. doi:10.1126/science.1218197.
[12] W.D. Westwood, N. Waterhouse, Structural and Electrical Properties of Tantalum Films Sputtered in Oxygen-Argon Mixtures, J. Appl. Phys. 42 (1971) 2946–2952.
[13] E.A.I. Ellis, M. Chmielus, S.P. Baker, Effect of sputter pressure on Ta thin films: Beta phase selection, texture, and stress, Acta Mater. 150 (2018) 317–326.
[14] J.B. Shu, S.S. Clyburn, T.E. Mates, S.P. Baker, Effect of oxygen on the thermomechanical behavior of passivated Cu thin films, J. Mater. Res. 18 (2003) 2122.
[15] W.C. Oliver, G.M. Pharr, An improved technique for determining hardness and elastic modulus using load and displacement sensing indentation experiments, J. Mater. Res. 7 (1992) 1564–1583. doi:10.1557/JMR.1992.1564.
[16] R.P. Vinci, J.J. Vlassak, MECHANICAL BEHAVIOR OF, Annu. Rev. Mater. Sci. 26 (1996) 431–462.
[17] H. Li, J.J. Vlassak, Determining the elastic modulus and hardness of an ultra-thin film on a substrate using nanoindentation, J. Mater. Res. 24 (2009) 1114–1126. doi:10.1557/jmr.2009.0144.
[18] A.A. Navid, A.M. Hodge, Nanostructured alpha and beta tantalum formation—Relationship between plasma parameters and microstructure, Mater. Sci. Eng. A. (2012). doi:10.1016/j.msea.2011.12.017.
[19] Z.H. Cao, P.Y. Li, H.M. Lu, Y.L. Huang, Y.C. Zhou, X.K. Meng, Indentation size effects on the creep behavior of nanocrystalline tetragonal Ta films, Scr. Mater. 60 (2009) 415–418. doi:10.1016/j.scriptamat.2008.11.016.
[20] Z.H. Cao, P.Y. Li, X.K. Meng, Nanoindentation creep behaviors of amorphous, tetragonal, and bcc Ta films, Mater. Sci. Eng. A. 516 (2009) 253–258. doi:10.1016/j.msea.2009.03.019.

[21] J.A. Thornton, High rate thick film growth, Annu. Rev. Mater. Sci. 7 (1977) 239–260. doi:10.1146/annurev.ms.07.080177.001323.
[22] S.Y. Grachev, F.D. Tichelaar, G.C. a. M. Janssen, Stress in sputter-deposited Cr films: Influence of Ar pressure, J. Appl. Phys. 97 (2005) 73508. doi:10.1063/1.1876579.
[23] I. Petrov, P.B. Barna, L. Hultman, J.E. Greene, Microstructural evolution during film growth, J. Vac. Sci. Technol. A Vacuum, Surfaces, Film. 21 (2003) S117–S128. doi:10.1116/1.1601610.
[24] S. Kasap, P. Capper, Electrical Conduction in Metals and Semiconductors, in: Springer Handb. Electron. Photonic Mater., Springer, Boston,MA, 2007: pp. 19–45.
[25] U. Mizutani, Introduction to the Electron Theory of Metals, Cambridge University Press, 2001.
[26] A. Arakcheeva, C. Gervais, V. Grinevitch, The self-hosting structure of b -Ta, Acta Crystallogr. Sect. B. B58 (2002) 1–7.
[27] M. Grosser, U. Schmid, The impact of sputter conditions on the microstructure and on the resistivity of tantalum thin films, Thin Solid Films. 517 (2009) 4493–4496. doi:10.1016/j.tsf.2008.12.009.
[28] W.D. Westwood, R.J. Boynton, P.S. Wilcox, The Effects of Argon Pressure on the Properties of Sputtered Tantalum Films, Thin Solid Films. 16 (1973) 1–25.
[29] J.A. Thornton, D.W. Hoffman, Internal stresses in titanium, nickel, molybdenum, and tantalum films deposited by cylindrical magnetron sputtering, J. Vac. Sci. Technol. 14 (1977) 164–169.
[30] T. Sun, B. Yao, A.P. Warren, K. Barmak, M.F. Toney, R.E. Peale, K.R. Coffey, Surface and grain-boundary scattering in nanometric Cu films, Phys. Rev. B - Condens. Matter Mater. Phys. 81 (2010) 1–12. doi:10.1103/PhysRevB.81.155454.
[31] J.J. Senkevich, T. Karabacak, D.-L. Bae, T.S. Cale, Formation of body-centered-cubic tantalum via sputtering on low-$\varkappa$ dielectrics at low temperatures, J. Vac. Sci. Technol. B Microelectron. Nanom. Struct. 24 (2006) 534. doi:10.1116/1.2166860.
[32] R. Knepper, B. Stevens, S.P. Baker, Effect of oxygen on the thermomechanical behavior of tantalum thin films during the β–α phase transformation, J. Appl. Phys. (2006). doi:10.1063/1.2388742.
[33] A. Schauer, M. Roschy, R.F. sputtered β-tantalum and b.c.c. tantalum films, Thin Solid Films. 12 (1972) 313–317. doi:10.1016/0040-6090(72)90095-8.
[34] M. Zhang, B. Yang, J. Chu, T. Nieh, Hardness enhancement in nanocrystalline tantalum thin films, Scr. Mater. 54 (2006) 1227–1230. doi:10.1016/j.scriptamat.2005.12.027.
[35] A. Subrahmanyam, K. Valleti, S. V Joshi, G. Sundararajan, Effect of arc suppression on the physical properties of low temperature dc magnetron sputtered tantalum thin films, J. Vac. Sci. Technol. A Vacuum, Surfaces, Film. 25 (2007) 378. doi:10.1116/1.2699296.
[36] Z.C. Cordero, B.E. Knight, C.A. Schuh, Six decades of the Hall – Petch effect – a survey of grain- size strengthening studies on pure metals, Int. Mater. Rev. 61 (2016) 495–512.
[37] S.P. Baker, Between nanoindentation and scanning force microscopy: measuring mechanical properties in the nanometer regime, Thin Solid Films. 308–309 (1997) 289–296. doi:10.1016/S0040-6090(97)00556-7.
[38] C.E. Carlton, P.J. Ferreira, What is behind the inverse Hall – Petch effect in nanocrystalline materials ?, 55 (2007) 3749–3756. doi:10.1016/j.actamat.2007.02.021.
[39] W.C. Oliver, G.M. Pharr, An improved technique for determining hardness and elastic modulus using load and displacement sensing indentation experiments, J. Mater. Res. 7 (1992) 1564–1583.
[40] T.Y. Tsui, W.C. Oliver, G.M. Pharr, Influences of stress on the measurement of mechanical properties using nanoindentation: Part I. Experimental studies in an aluminum alloy, J. Mater. Res. 11 (1996) 752–759. doi:10.1557/JMR.1996.0091.
[41] A. Bolshakov, W.C. Oliver, G.M. Pharr, Influences of stress on the measurement of mechanical properties using nanoindentation : Part II . Finite element simulations, J. Mater. Res. 11 (1996) 760–768.
[42] J.J. Vlassak, W.D. Nix, MEASURING THE ELASTIC PROPERTIES OF MATERIALS

BY MEANS OF INDENTATION, J. Mech. Phys. Solids. 42 (1994) 1223–1245.
[43] J. Carloni, Mechanical Deformation and Strengthening Mechanisms in Calcite Single Crystals, Cornell University, 2017.
[44] R. Knepper, S.P. Baker, Coefficient of thermal expansion and biaxial elastic modulus of β phase tantalum thin films, Appl. Phys. Lett. (2007). doi:10.1063/1.2734468.
[45] W.D.J. Callister, D.G. Rethwisch, Materials Science and Engineering, 9th ed., John Wiley & Sons, Inc., Hoboken, N.J., 2014.
[46] R. Saha, J.A. Barnard, Effect of structure on the mechanical properties of Ta and Ta(N) thin films prepared by reactive DC magnetron sputtering, J. Cryst. Growth. 174 (1997) 495–500. doi:10.1016/S0022-0248(96)01148-7.
[47] F. Ferreira, C. Sousa, A. Cavaleiro, A. Anders, J. Oliveira, Phase tailoring of tantalum thin films deposited in deep oscillation magnetron sputtering mode, Surf. Coatings Technol. 314 (2017) 97–104. doi:10.1016/j.surfcoat.2016.08.017.
[48] R. Knepper, S.P. Baker, Coefficient of thermal expansion and biaxial elastic modulus of *B* phase tantalum thin films, Appl. Phys. Lett. 90 (2007) 27–30. doi:10.1063/1.2734468.
[49] M.H. Mueller, The lattice parameter of tantalum, Scr. Metall. 11 (1977) 693. doi:10.1016/0036-9748(77)90141-7.
[50] N. Schwartz, W.A. Reed, P. Polash, M.H. Read, Temperature coefficient of resistance of beta-tantalum films and mixtures with b.c.c.-tantalum, Thin Solid Films. 14 (1972) 333–347. doi:10.1038/467S2a.
[51] N.N. Kovaleva, D. Chvostova, A. V Bagdinov, M.G. Petrova, E.I. Demikhov, F.A. Pudonin, A. Dejneka, Interplay of electron correlations and localization in disordered b - tantalum films : Evidence from dc transport and spectroscopic ellipsometry study, Appl. Phys. Lett. 51907 (2015). doi:10.1063/1.4907862.
[52] L. Pauling, Metallic Valence, in: Gen. Chem. 3rd Ed., 1970: p. 586.

CHAPTER 5

Influence of initial β-Ta microstructure on texture patterning in phase transformed α-Ta thin films

Elizabeth A. I. Ellis[1], Marissa A. Linne[2], Markus Chmielus[2], and Shefford P. Baker[1,2]

1. *Cornell University, Sibley School of Mechanical and Aerospace Engineering, Upson Hall, Ithaca, NY 14853*
2. *Cornell University, Department of Materials Science and Engineering, Bard Hall, Ithaca, NY 14853*

This chapter is a draft of a paper being prepared for publication. My contribution to the work was in helping to deposit films and take EBSD data, in interpreting the data and formulating the growth mechanism, and in co-advising Marissa Linne.

ABSTRACT

Recent work has shown that tantalum films deposited in the beta phase and annealed to transform to the alpha phase show an unusual microstructure featuring long-range orientation gradients and discontinuous grain boundaries. In this article, we show that that variations in the initial beta film structure created by depositing under different argon sputter pressures have dramatic effects on the magnitude of the resulting orientation gradients and associated texture patterns. Electron backscatter diffraction and pole figure analysis reveal many interesting features of these texture patterns, including the fact that seemingly unrelated film areas separated by large distances are actually parts of the same structure. We analyze these patterns to suggest a nucleation and growth sequence by which they might form.

5.1. INTRODUCTION

Tantalum thin films have been the focus of considerable attention over the last several years [1–5]. The stable α phase of Ta has long been used for applications such as Cu/Si diffusion barriers [6] and wear-resistant coatings [7], and the metastable β phase has received special attention since the discovery that β-Ta films show a large spin Hall effect and may be of interest for new magnetoresistive memory technologies [8].

When β-Ta is annealed at an adequate temperature, the film transforms to the stable α phase [9–12]. Baker *et al.* [13] showed an unusual structure in phase transformed α-Ta films that includes continuous long-range orientation gradients and a discontinuous orientation boundary structure. An example of this unusual microstructure is reproduced in Figure 5.1, below.

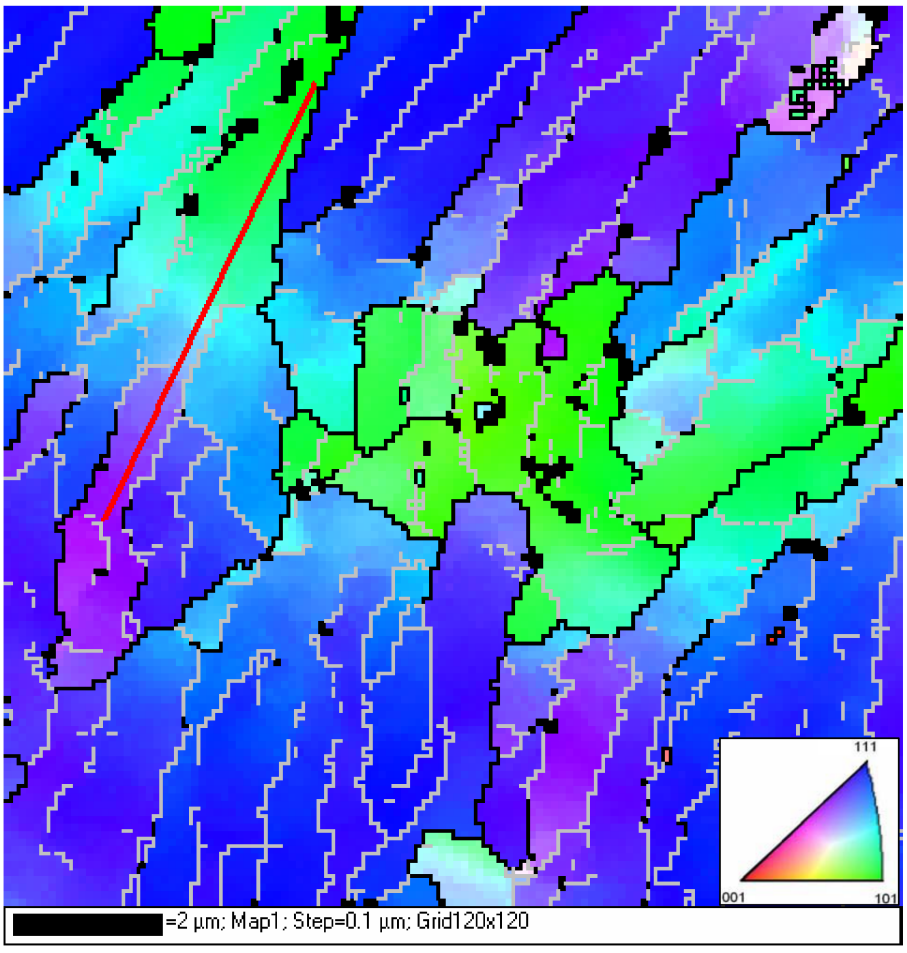

Figure 5.1: EBSD map showing out-of-plane orientation in a phase-transformed α-Ta film. Color indicates out-of-plane orientation according to the stereographic triangle. The microstructure features orientation gradients and discontinuous orientation boundaries. Orientation rotates smoothly from (110) to (211) along redline. From [14].

Figure 5.1 shows the orientation map of a phase-transformed α-Ta film as measured by EBSD. Color indicates out-of-plane orientation according to the stereographic triangle, and grey and black lines indicate orientation boundaries of greater than 4° and greater than 8°, respectively. The smooth transitions in color without boundary crossings indicate that the orientation of the film rotates smoothly through large angles over large distances. For example, the orientation along the red line in Figure 5.1 begins at the lower left with a near-(211) out-of-plane orientation and continues through a (221) orientation to a (110) orientation, all without crossing a single orientation boundary greater than 4°. This is a rotation of about 28° over 7 μm, or about 4°/μm.

This rotation is not uniform over the entire film, however, and as a result, orientation boundaries can be discontinuous. If we begin in a single-orientation region and follow parallel paths with two different rotation rates, we will inevitably develop an orientation boundary between the two paths, beginning as a low-angle boundary and increasing to large misorientations. Several such boundaries are visible in Figure 5.1, where a boundary appears as a low-angle boundary in the middle of a seemingly single-orientation region, then becomes a high-angle boundary. Because of these discontinuous boundaries and orientation gradients, "grains" as such do not exist in these structures. For this reason, we will continue to describe the boundary between areas of different orientation as "orientation boundaries" rather than grain boundaries.

Baker *et al*. [13] also describe the microstructures in a series of films deposited under various partial pressures of oxygen, ranging from 2.5 x 10^{-6} to 8.1 x 10^{-6} Torr. These films show wide variation in microstructure: as oxygen content increases, the distance between boundaries increases, and orientation changes more slowly. In the highest-oxygen content film, only orientations near (110) and (221) appear in the sampled area, either because other orientations are not present in the film at all, or because the sampled area is too small and the rotation rate too low to capture all of the orientations that are present. These films also show repeating orientation patterns which they call "texture patterns", such as repeating stripes of (111) and (110) orientation.

Orientation gradients require an array of unpaired dislocations [15], and Baker *et al*. [13] propose a mechanism by which necessary dislocations might arise, due to kinetic limitations on diffusion at phase boundaries. Briefly, they suggest that the higher density of the α-Ta phase will lead to a surface step at the phase boundary, and that limited diffusion across this step will prevent crystal planes in the growing α-Ta grain from being completed, leading to an array of edge dislocations with their sense vectors lying in the plane of the film parallel to the α-Ta growth front. They also note that rotations about ⟨211⟩ crystal directions are common, and could indicate the presence of ⟨111⟩{110}-type dislocations. However, Baker *et al*. did not explain the origins of the texture patterns they observe, or study nucleation, and therefore could not provide a temporal or spatial sequence for how these texture patterns might form.

Meanwhile, Ellis *et al*. have conducted a detailed study of the structure [16] and properties [17] of a series of β-Ta films formed by magnetron sputtering while carefully controlling oxygen contamination at a variety of argon working gas pressures, p_{Ar}. They show that all films consist of the β-Ta phase with a (002) fiber texture, and that this (002) texture component broadens with increasing sputter pressure but is not replaced by any other texture components (See Chapter 3 of this thesis). As sputter pressure increases, stress increases from -1360 to 1140 MPa and grain size increases from 22.5 to 49.2 nm.

In the present work, we have made a duplicate set of films, deposited under identical conditions to those in Ellis *et al*. [16], and transformed them to α-Ta by thermal cycling in ultra-high vacuum (UHV). EBSD images reveal a range of texture patterns that vary systematically with the structure of the initial β-Ta film. By analyzing these texture patterns, we are able to propose a mechanism by which the orientation gradient structure might form, and gain important insights into the nature of this unusual microstructure.

5.2. EXPERIMENTS AND RESULTS

Tantalum films were deposited in the β phase at a range of sputter pressures, then annealed to transform to the α phase. The resulting films were examined using EBSD.

5.2.1. Film deposition and microstructural characterization

A series of Ta thin films were prepared and characterized using methods previously reported by Ellis *et al*. [16]. The films reported here were a duplicate set to those reported previously, made using the same parameters.

Briefly, films were deposited in a UHV deposition chamber by magnetron sputter deposition using a background pressure of 2 x 10^{-6} Pa or better. Substrates were (100) Si wafers with native oxide. The films were deposited using Ar sputter pressures of 0.3, 1.1, 1.6, 1.9, 2.0, and 2.2 Pa. Wafers were plasma cleaned to remove adsorbed impurities, and the sputtering gas was ultra-high purity Ar with additional oxygen filtration. A nominally identical set of films, made at the same time, were shown to consist solely of (002)-oriented β-Ta, and rocking curve scans show that this texture component broadens with increasing sputter pressure but that no other texture components or randomly-oriented populations appear [16]. SEM images showed that grain size increased from 22.5 to 49.2 nm [17]. We assume that the films studied in this chapter had similar initial microstructures.

5.2.2. Thermal cycling and stress measurements

While the films reported earlier [16,17] were removed from the UHV system in their as-deposited form for further characterization, the identically-prepared films presented here were transferred to another chamber within the UHV system, without breaking vacuum, where they were subjected to thermal cycles to induce a transformation to the alpha phase while the substrate curvature was measured using a laser scanning system [18] for subsequent stress analysis. The films were cycled from room temperature to 700°C at a rate of 5°C/min while measuring substrate curvature. Stresses were calculated from the measured curvatures using the Stoney relation. The results of these stress-temperature measurements are shown in Figure 5.2.

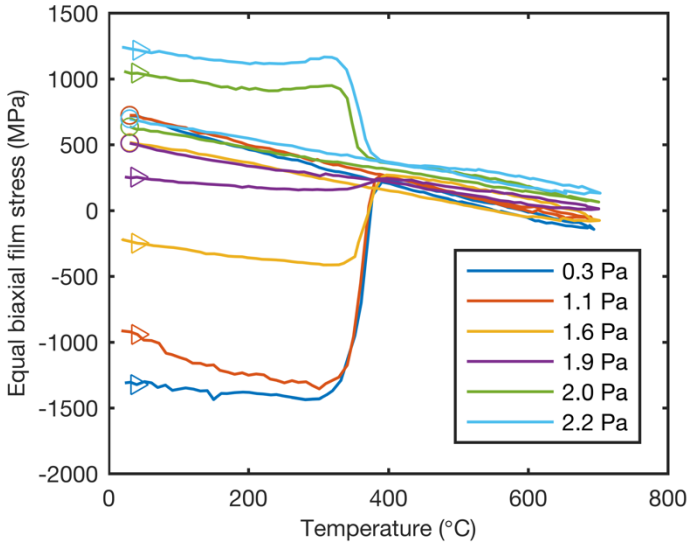

Figure 5.2: Stresses in Ta films during thermal cycles determined using a substrate curvateu method. Triangles indicate beginning of curves and final values are circled, The stress change occurring at about 350°C indicates the phase transformation.

The initial stresses in the β-Ta films vary widely, from highly compressive (-1310 MPa) in the low p_{Ar} films to highly tensile (1240 MPa) in the high p_{Ar} films. These values are similar to the initial stress values reported in [16], indicating that the structure of these films in their as-deposited state is similar as well. As the temperature approaches 350°C, a large stress change indicates that the transformation to the stable α phase has begun [11]. Past 400°, all film stresses converge and follow roughly the same path, ending with an equal biaxial stress between 500 and 700 MPa in the α phase.

5.2.3. EBSD characterization

Following stress-temperature cycles, the films were characterized using EBSD with an electron beam voltage of 25 kV and a current of 1.2 nA, and shown to be in the α phase. Sampled areas were 56 x 60 μm, with a step size of 0.4 μm. HKL CHANNEL 5 software was used to create orientation maps and pole figures from measured orientation data. Unindexed pixels (<15% of the imaged area) were interpolated using the average orientation of neighboring pixels. The resulting out-of-plane orientation maps are shown in Figure 5.3.

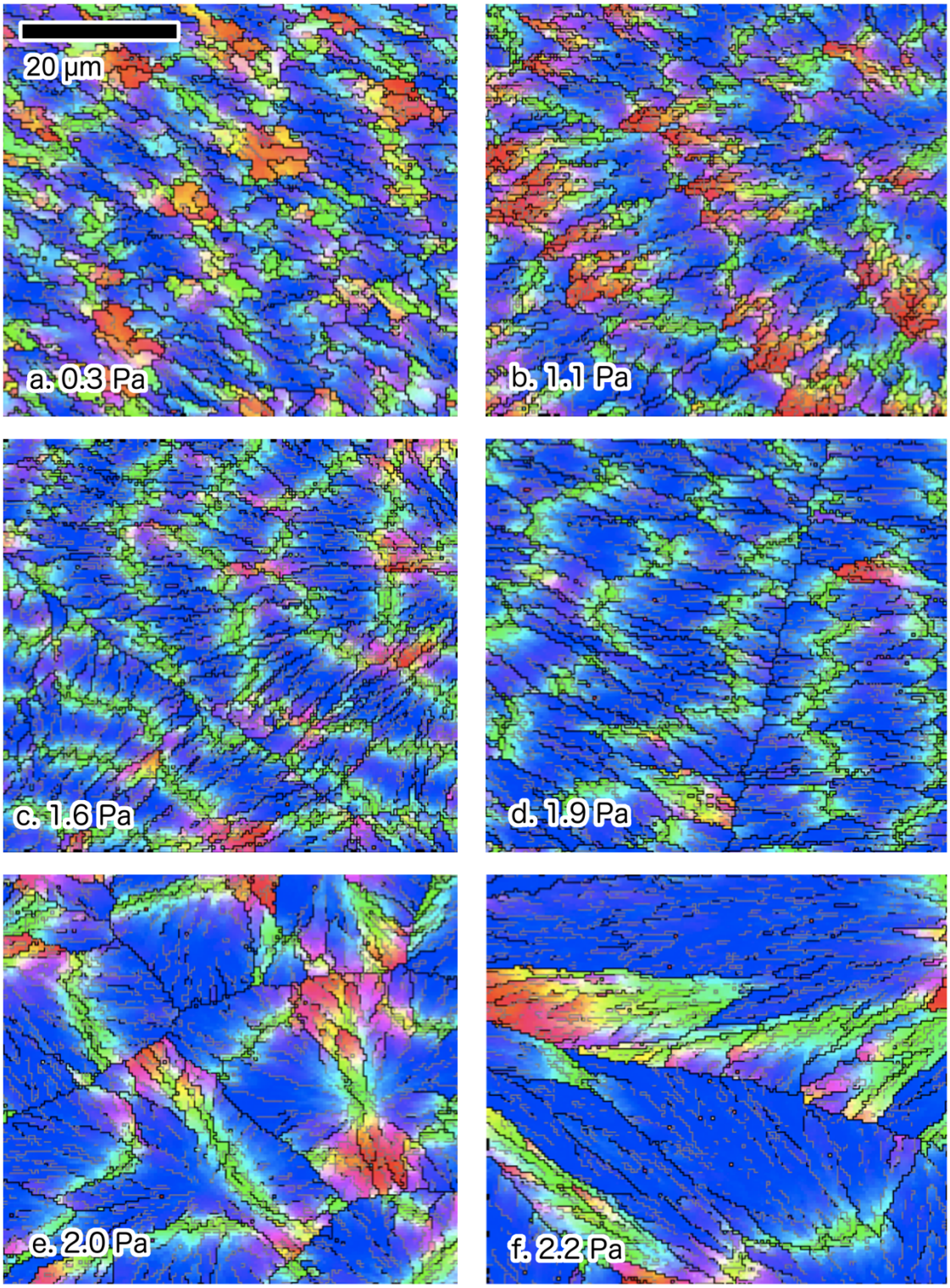

Figure 5.3: EBSD maps showing out-of-plane orientations of phase-transformed α-Ta films deposited at different sputter pressures. All images cover an area of 56 x 60 µm with a step size 0.4 µm. Color indicates orientation according to the stereographic triangle in Fig 5.1. All films have the orientation gradient structure.

Boundaries between orientations differing by more than 8° are shown in black, and those between 4 and 8° are shown in grey. All films show orientation gradients and discontinuous grain boundaries, but the magnitude of the gradients decreases, and the distance between orientation boundaries increases, with increasing sputter pressure. Figure 5.3a shows a texture pattern previously described [13] as "random", in that gradients appear but do not follow repeating patterns. In Fig 5.3b, elements of a striped pattern seem to be forming, while Fig 5.3c and d clearly show striped patterns. Fig 5.5e appears to show a "tiled" pattern, described previously [13], in which geometric patterns repeat to cover the surface of the film. Fig 5.3f is more difficult to interpret as the scale of the pattern is large in comparison to the field of view. In general, there seem to be repeating texture patterns occasionally interrupted by high-angle boundaries.

The EBSD orientation data from the α-Ta films may also be viewed as pole figures.

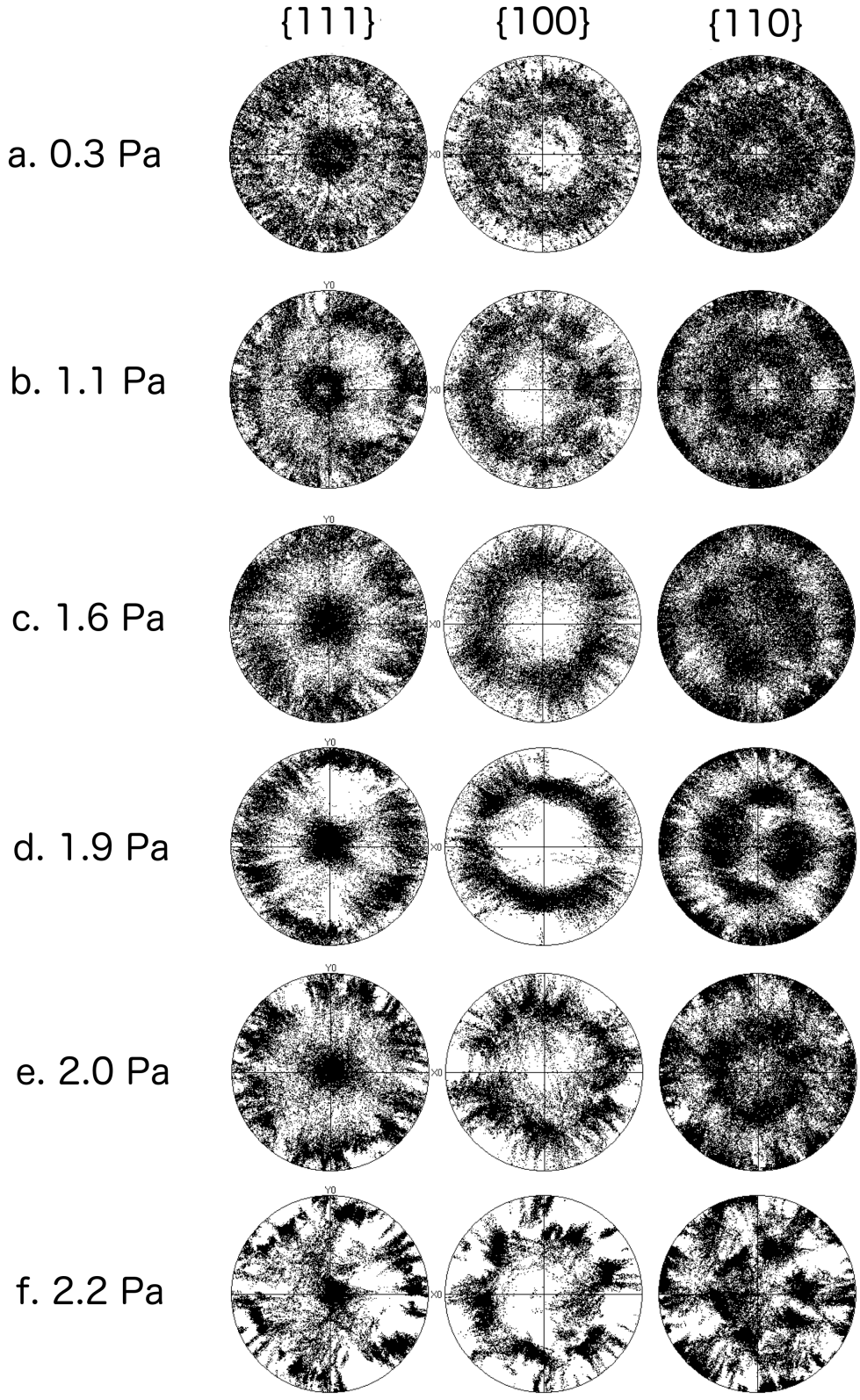

Figure 5.4: {111}, {100}, and {110} pole figures of phase transformed α-Ta films obtained from EBSD. Each image shows the distribution of poles corresponding to the images in Fig. 5.3.

Figure 5.4 shows {111}, {100}, and {110} pole figures made from the orientation data shown as orientation maps in Figure 5.3. Each pixel in the orientation maps shown in Figure 5.3 corresponds to a single set of point on the pole figure. A naïve interpretation of these pole figures suggests that all films have some degree of (111) fiber texture, based on the diffuse peak near the center of the pole figures and the apparently random azimuthal distribution (except perhaps the high p_{Ar} films). This reflects the fact that a (111) out-of-plane orientation is more common than other orientations, but the structure is considerably more complex than a simple (111) fiber texture would suggest. As sputter pressure increases, more in-plane detail becomes apparent, and (111) poles seem to follow streak-like patterns near the edge of the pole figures.

5.3. DISCUSSION

EBSD orientation maps and pole figure data reveal common features of the orientation gradient microstructures and texture patterns, and allow us to suggest a mechanism by which they might form.

5.3.1. Phase transformation and stresses

The stress-temperature curves shown in Fig. 2 indicate that while initial stresses in the β-Ta films vary widely, all film stresses converge as the film transforms to the stable α phase. In a previous work on nominally identical films made in the same deposition chamber, Knepper et al. [11] showed that the stress change occurring at about 350°C corresponds to the phase transformation. Knepper et al. explained the change in stress as arising from the differences in equilibrium density between the α and β phases—the α phase is significantly denser—as well as the removal of excess volume at grain boundaries due to grain growth during the transformation. These two effects combine to produce a change in stress in the tensile direction of 2.3 GPa [11]. However, the films discussed in this chapter undergo a more complicated behavior, in that the stresses in each film converge on a small range of values (200-400 MPa) during the transformation, then follow the expected thermoelastic slope for α-Ta [10] for the remainder of the thermal cycle,

finishing with a room-temperature equal biaxial stress of between 500 and 700 MPa in the α films. It is particularly odd that the two highest-pressure films actually experience a stress change in the compressive direction, as both of the explanations mentioned above—density differences and grain growth— should lead to changes in the tensile direction. This stress convergence behavior is unknown clearly warrants further investigation.

5.3.2. Gradient and boundary structure

Since the misorientation between the crystals on either side of a boundary changes with position along the boundary, the criterion used to define orientation boundaries can have a dramatic effect on the appearance of the structure. Figure 5.5 shows the orientation map of the film deposited at 1.6 Pa, with two different boundary criteria.

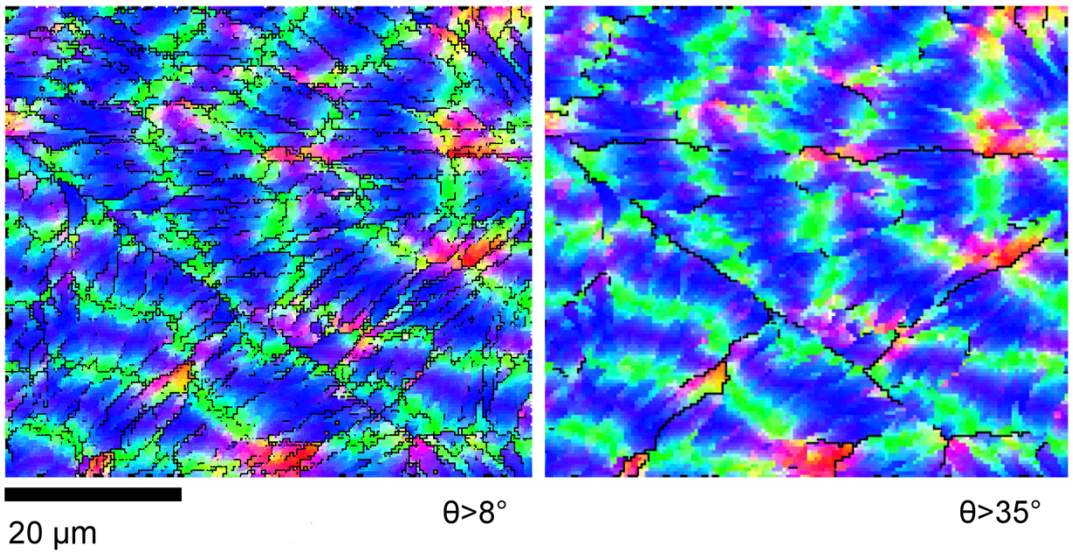

Figure 5.5: EBSD map of film deposited at 1.6 Pa, with orientation boundaries defined as >8° (left) and >35° (right) marked in black.

In the absence of well-defined grains, we analyze microstructural changes by comparing the average distance between orientation boundaries (calculated in HKL CHANNEL5 using ASTM E112 standard), shown in Figure 5.6.

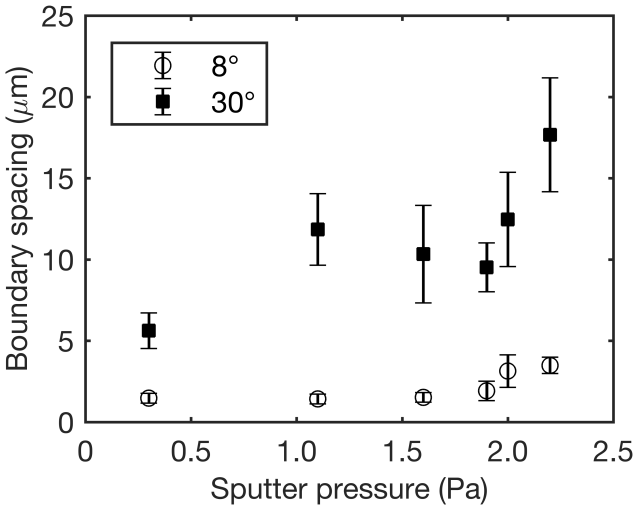

Figure 5.6: Orientation boundary spacing vs. sputter pressure as measured according to two criteria: misorientations greater than 8° and greater than 30°.

The distance between boundaries visible in Figure 5.3 increases with sputter pressure according to either definition of orientation boundary. This also means that the extent of the orientation gradients—that is, the length over which an orientation may rotate smoothly without being interrupted by an orientation boundary—increases with sputter pressure.

5.3.3. Long range correlated rotations

The EBSD orientation maps in Figure 5.3 show orientation gradients that continue over very long distances (several hundred times the film thickness) and even past high-angle orientation boundaries. To investigate how different regions of the films might be related, we return to the pole figures. Figure 5.7 shows a subsection {111} pole figure for the film deposited at 2.2 Pa and the related area of the orientation map.

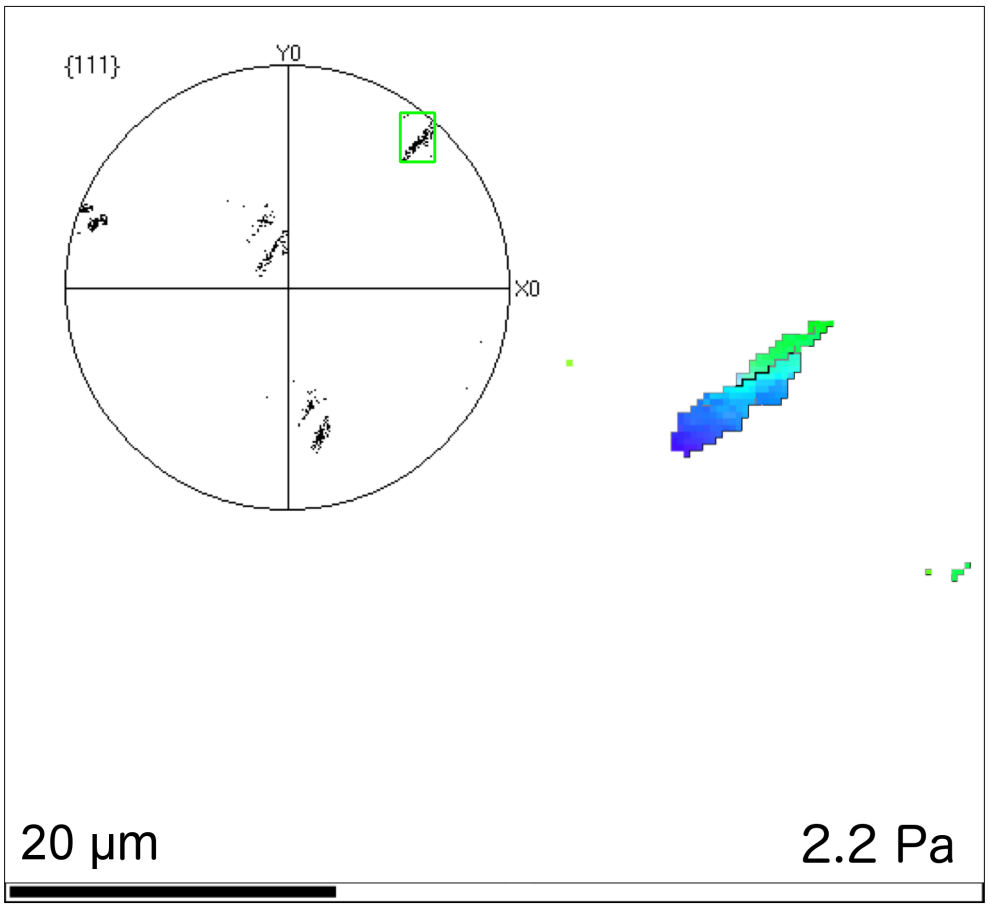

Figure 5.7: Selected area {111} pole figure for film deposited at 2.2 Pa. The areas of the film with {111} poles within the green outline are shown in the orientation map.

The selected area pole figure in Figure 5.7 is created by plotting all the {111} poles from those pixels that have a {111} pole within the region outlined in green. This region was chosen because it corresponds to a prominent streak visible in the full {111} pole figure. The corresponding pixels from the orientation map show that (with the exception of 6 random distant pixels) this streak corresponds to small related area of the film with an orientation gradient that rotates from near (111) to near (110). The pole figure shows two parallel streaks at the center and bottom right, in addition to two more equiaxed spots in the top left quadrant. The orientation of the streaks in the pole figure suggest that the orientations in this area of the film are related by rotation about an axis near these equiaxed spots. As the orientation rotates about axes lying in the plane of the film and about 15° from horizontal, the other {111} poles form streaks, one of which

defines the selected area in Figure 5.7. Each equiaxed spot creates two parallel streaks due to their slight difference in orientation. This suggests that all such streaks visible in Figure 5.4 may be the result of related film areas rotating about a single axis.

We therefore examined streak patterns in the pole figures from other films. Figure 5.8 shows a selected area pole figure from the film deposited at 2.0 Pa:

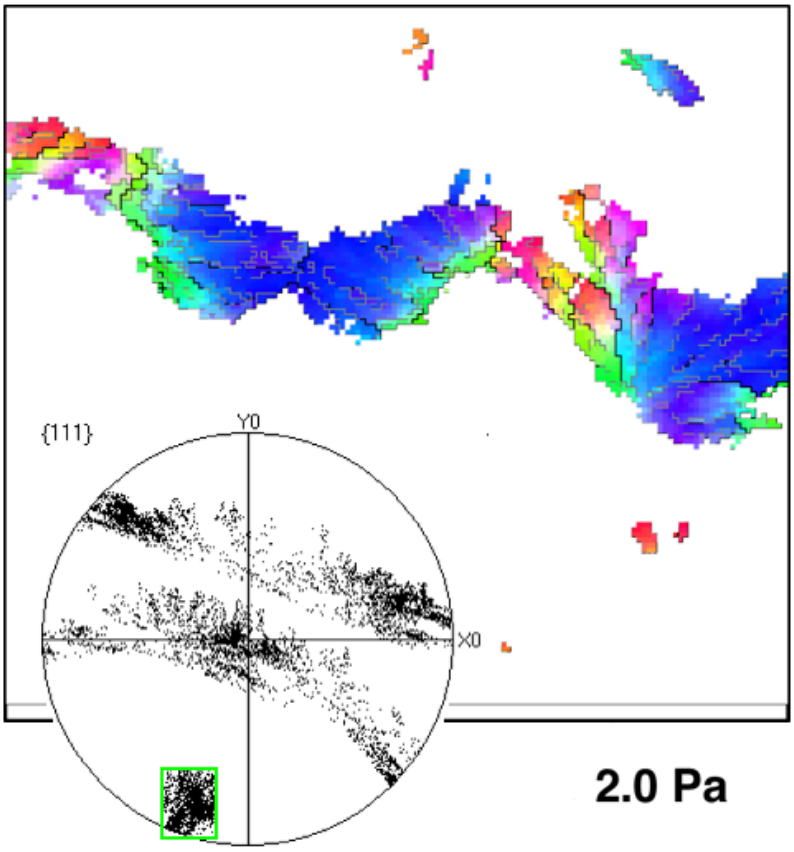

Figure 5.8: Selected area {111} pole figure from film deposited at 2.0 Pa. All portions of the film shown above have a {111} pole in the green section of the pole figure.

Again, we have plotted all the {111} poles from pixels having a {111} pole in the green box in the pole figure, and these same pixels are shown in an orientation image. This figure shows that large areas of the 2.0 Pa film are in fact related, in that all of the represented areas have a {111} pole in the same direction. The other {111} poles associated with these areas of the film sweep across the pole figure, indicating that these orientations are rotating about a pole lying in or near the green box; *i.e.* a rotation axis lying nearly in the plane of the film in sample coordinates.

More importantly, the entire region shown in Figure 5.8 represents a large region related by rotation about a single axis, and suggests that these orientation gradient structures must result from long-range growth from a small number of initial nuclei. In their as-deposited state, the films have fiber texture and grain sizes in the tens of nm—no microstructure exists in the as-deposited films on the scale of these observed orientation gradient regions. Thus, the dislocations that give rise to these orientation gradients must be introduced during the growth of new alpha phase material into the preexisting beta—i.e. motion of α/β phase boundaries.

The lowest-energy slip system in BCC Ta is the $\langle 111 \rangle \{110\}$ system [19]. Dislocations of this type would tend to produce rotations about $\langle 211 \rangle$-type crystal directions. We do not see evidence that $\langle 211 \rangle$-type rotations are more common than others, though of course, multiple dislocations might combine to form a net rotation about another axis. Nevertheless, it is clear that further analysis will be required to determine the dislocations that underlie these orientation gradients.

5.3.4. Texture pattern formation

The above results allow us to suggest a sequence of events by which these texture patterns might form. As proposed previously [13], α-Ta nucleates at a few locations in each film, and rotation is introduced as dislocations form at the moving phase boundary. As the phase boundary moves through the film, it leaves behind the texture patterns we observe.

First, we must be able to identify nuclei. This turns out to be relatively straightforward. Low-angle boundaries form when neighboring film areas rotate at different rates or about slightly different axes, and can eventually become high-angle boundaries if growth is uninterrupted. Several such boundaries are visible in Figure 5.9, showing the film deposited at 2.0 Pa.

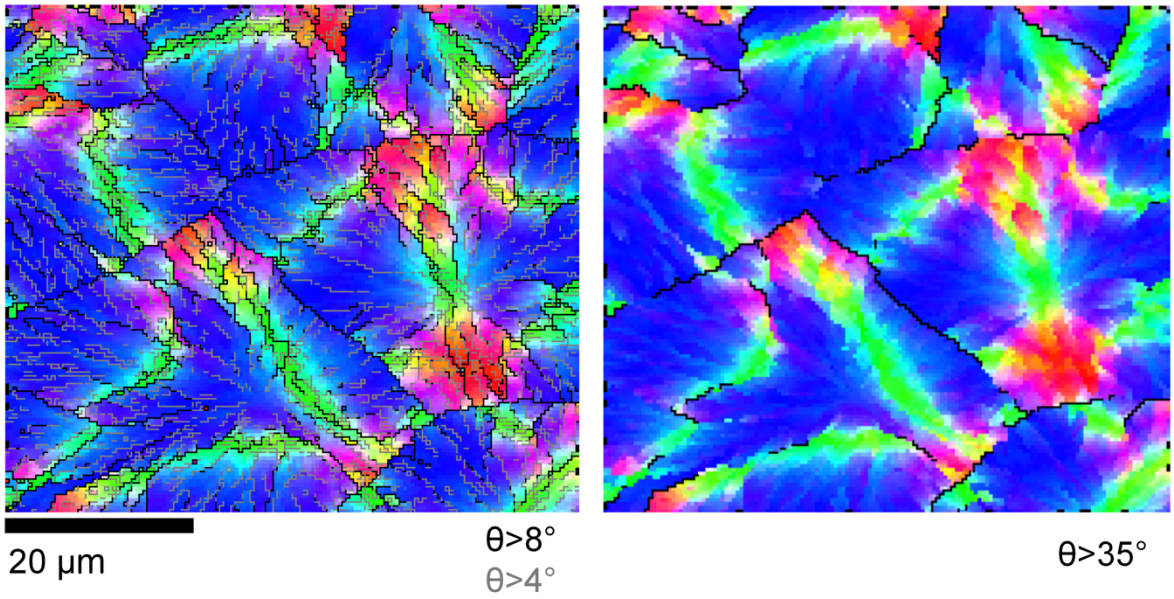

Figure 5.9: EBSD orientation maps of the film deposited at 2.0 Pa, showing two criteria for orientation boundaries. Left: Boundaries greater than 8° in black, between 4° and 8° in grey. Right: Boundaries greater than 35° in black.

On the left, boundaries greater than 8° are marked in black, and those between 4° and 8° are marked in grey. On the right, only boundaries greater than 35° are marked. The very high-angle boundaries on the right seem to mark out several distinct regions of the film, many of which feature low-angle boundaries radiating out from a central location in the left-hand image. This suggests that nucleation occurred in a few locations and growth proceeded outward until encountering another transformed region and forming a high-angle orientation boundary. The necessary rotations must form during the growth process.

The film deposited at 2.0 Pa has a prominent triangular pattern, similar to one reported previously [13], and shown in Figure 5.10.

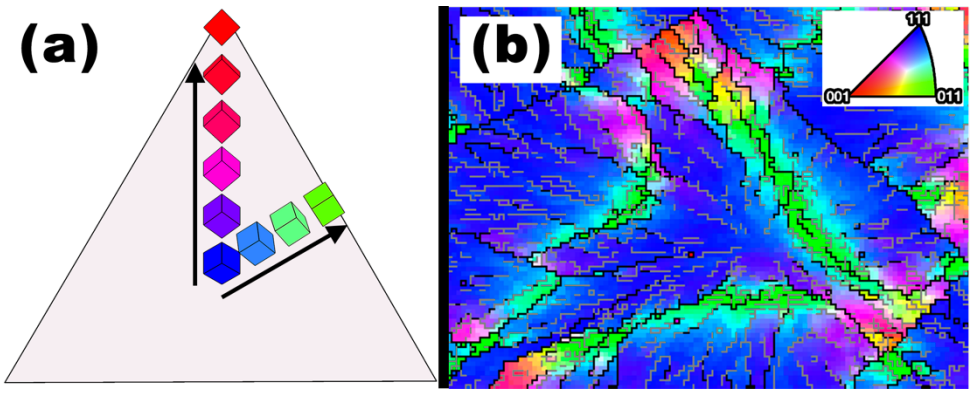

Figure 5.10: Triangular texture pattern from film deposited at 2.0 Pa, and rotation scheme by which it might form.

The triangle in Figure 5.10b consists of a (111)-oriented center, with stripes of (110)-oriented material along the edges and regions of (100)-oriented material at the corners. This orientation relationship is identical to that in a standard stereographic projection, and can easily be recreated using a simple rotation scheme, shown in Figure 5.10a. We begin in the center of the triangle with a (111) orientation, and as we move out from the center, we rotate outward about axes lying in the plane of the film, perpendicular to the direction of travel. In moving toward the vertices of the triangle we pass through a (211) orientation to a (100) orientation, and in moving toward the edges we pass through a (221) orientation to a (110) orientation. Just past these orientations, we encounter a high-angle boundary and the texture pattern is interrupted.

A similar mechanism can explain the texture patterns observed in other films in this series. According to this model, we should find low-angle boundaries radiating out from nucleation sites. Some of these low-angle boundaries may become high-angle boundaries but the orientations on either side should still be correlated even if they are not identical. In contrast, another type of high-angle boundary should form when two growing α regions collide, without any correlation between the orientations on either side. These two types of high-angle boundaries are highlighted in Figure 5.11, showing the film deposited at 2.0 Pa.

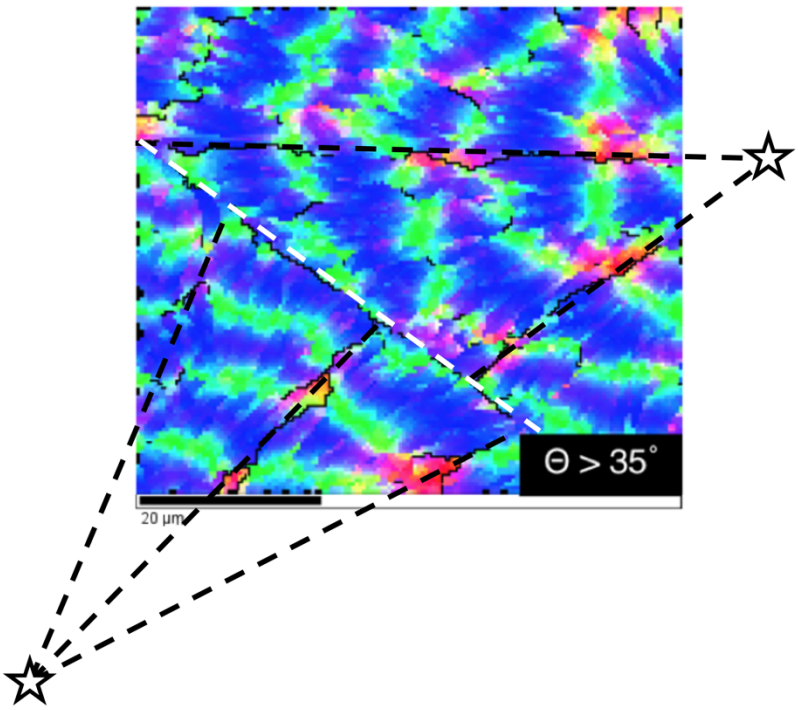

Figure 5.11: EBSD map of film deposited at 1.6 Pa, with high-angle orientation boundaries and suggested pattern centers highlighted.

Boundaries marked by black dashed lines radiate from two points, marked by stars, while the boundary marked in white runs between them. The pattern centers also seem to mark the center of several concentric circles of (110)-oriented material. The (110) stripes continue across the black boundaries, but stop at the white boundaries. The presence of these boundaries is therefore consistent with growth from two nucleation sites toward a high-angle boundary. The (110) stripes are consistent with the rotation mechanism as well. If the rotation were to continue past the boundaries of the triangle pattern in Figure 5.10, the resulting pattern should have stripes of (110)-oriented material on a (111) field, with the stripes joined at intervals by (100)-oriented areas. Each (100)-oriented area should connect four (110) stripes. These patterns are readily apparent in the film and confirm that this texture pattern is equally consistent with the simple rotation mechanism proposed above. The stripes visible in the film deposited at 1.9 Pa (Figure 5.3d) might be formed by a similar mechanism. In the films deposited at 0.3, 1.1, and 2.2 Pa, too

little of any single uninterrupted gradient is visible to discern such patterns. In the low-pressure films, this occurs because nucleation sites are closer together, while in the highest-pressure film the field of view is small in comparison to the magnitude of the orientation gradient.

5.3.5. Proposed nucleation mechanism

Based on our interpretation of the film growth sequence, we should necessarily expect the distance between high-angle boundaries (Fig 5.6) to be correlated with the number of nucleation sites, as not every high-angle boundary separates two nucleation sites, as shown in Figure 5.11. Identifying nucleation sites requires an analysis of the texture patterns and boundary structure similar to that in section 5.3.4, in order to identify individual nucleation sites and associated regions of the α-Ta film (As explained in section 5.1, these regions are not grains, as they contain multiple orientations. We will call them "daughter regions" in recognition of the fact that they descend from a single nucleus.) Unfortunately, this analysis is not really possible to do in a rigorous way for all of the film data shown in Fig 5.3. We have identified two daughter regions in the film deposited at 1.6 Pa, and the films deposited at 1.9 and 2.2 Pa seem to show two daughter regions as well. The film deposited at 2.0 Pa might have as many as five daughter regions. The other films, those deposited at 0.3 and 0.5 Pa are not as easy to interpret. Even if we were confident in the number of daughter regions identified in each EBSD image, the sampled area is too small to provide statistically significant measurement of nucleation density. The magnitude of the orientation gradients, however, does clearly decrease with sputter pressure. We might therefore expect that the magnitude of the gradients depends on the density of grain boundaries in the initial β-Ta film and occurs during the growth phase, while the nucleation density is governed by a different process.

Previous researchers [13] have suggested that the development of orientation gradients might occur due to kinetic limitations, which is consistent with our observation that the magnitude of the orientation gradients is related to the structure of the initial β-Ta films. One might instead expect that these dislocations indicate plastic deformation due to stresses that arise during the

transformation. In this case, however, we should expect to see some relationship between the magnitude of the equal biaxial film stress and the resulting patterns. The initial stress in the β-Ta films ranges from highly compressive in films deposited at low p_{Ar} to highly tensile in films deposited at high p_{Ar}, and films deposited at 1.6 and 1.9 Pa have initial stresses near zero. The magnitude of the orientation gradients in the phase-transformed films, however, seems to increase monotonically with p_{Ar}. This suggests a kinetic origin is more likely for the dislocations in these structures.

5.4. SUMMARY AND CONCLUSIONS

We prepared a series of α-Ta films with different microstructures by depositing films in the β phase under sputter pressures from 0.3 to 2.2 Pa and annealing in UHV. The resulting films have long-range orientation gradients and discontinuous orientation boundaries, and both orientation gradient magnitude and boundary spacings change with sputter pressure. These microstructures are consistent with a nucleation-and-growth process in which α-Ta nucleates and dislocations are injected at the phase boundary as the nucleus grows, leading to characteristic rotations about axes in the phase boundary [13]. A triangular pattern, observed in the 2.0 Pa film and in previous reports [13], can arise if α-Ta nucleates with a (111) orientation and rotates about axes that lie in both the phase boundary and in the plane of the film, and concentric (111)-oriented stripes, as observed in the 1.6 Pa film, may form by a similar mechanism. Nucleation of α-Ta decreases with increasing as-deposited β-Ta grain size, and the dislocations required for orientation gradients seem more likely to arise from a kinetic mechanism than by a stress-driven mechanism.

Further work will investigate the character and slip systems of the dislocations required to form these orientation gradients and texture patterns.

5.5. ACKNOWLEDGMENTS

Support for this work was provided by the National Science Foundation (DMR 0706507 and DMR 1106223). This work also made use of the facilities of the Cornell Center for Materials

Research with support from the National Science Foundation Materials Research Science and Engineering Centers program (DMR 1120296).

5.6. REFERENCES

[1] M.H. Read, C. Altman, A new structure in tantalum thin films, Appl. Phys. Lett. (1965).

[2] K. Ino, T. Shinohara, T. Ushiki, T. Ohmi, Ion energy , ion flux , and ion species effects on crystallographic and electrical properties of sputter-deposited Ta thin films, J. Vac. Sci. Technol. A. 15 (1997) 2627–2635.

[3] R.A. Roy, Role of energetic atoms and ions in Ta films grown by different physical vapor deposition methods, J. Vac. Sci. Technol. B Microelectron. Nanom. Struct. 11 (1993) 1921. doi:10.1116/1.586523.

[4] L.G. Feinstein, R.D. Huttemann, Factors controlling the structure of sputtered Ta films, Thin Solid Films. 16 (1973) 129–145.

[5] A.A. Navid, A.M. Hodge, Nanostructured alpha and beta tantalum formation—Relationship between plasma parameters and microstructure, Mater. Sci. Eng. A. (2012). doi:10.1016/j.msea.2011.12.017.

[6] K. Holloway, P.M. Fryer, Tantalum as a diffusion barrier between copper and silicon, Appl. Phys. Lett. 57 (1990) 1736. doi:10.1063/1.104051.

[7] D.W. Matson, E.D. Mcclanahan, S.L. Lee, D. Windover, Properties of thick sputtered Ta used for protective gun tube coatings, Surf. Coatings Technol. 146–147 (2001) 344–350. doi:10.1016/S0257-8972(01)01402-5.

[8] L. Liu, C.-F. Pai, Y. Li, H.W. Tseng, D.C. Ralph, R.A. Buhrman, Spin-Torque Switching with the Giant Spin Hall Effect of Tantalum, (n.d.).

[9] L.A. Clevenger, A. Mutscheller, J.M.E. Harper, C. Cabral, K. Barmak, The relationship

between deposition conditions, the beta to alpha phase transformation, and stress relaxation in tantalum thin films, J. Appl. Phys. 72 (1992) 4918. doi:10.1063/1.352059.

[10] R. Knepper, S.P. Baker, Coefficient of thermal expansion and biaxial elastic modulus of β phase tantalum thin films, Appl. Phys. Lett. 90 (2007) 181908. doi:10.1063/1.2734468.

[11] R. Knepper, B. Stevens, S.P. Baker, Effect of oxygen on the thermomechanical behavior of tantalum thin films during the β–α phase transformation, J. Appl. Phys. (2006). doi:10.1063/1.2388742.

[12] M. Croset, G. Velasco, Structure and Composition of Sputtered Tantalum Thin Films on Silicon Studied by Nuclear and X-Ray Analysis, J. Appl. Phys. 43 (1972) 1444–1448.

[13] S.P. Baker, R. Knepper, K. Jackson, Aubain, In progress, (2018).

[14] R.A. Knepper, Thermomechanical behavior and microstructure evolution of tantalum thin films during the beta-alpha phase transformation, Cornell University, 2007.

[15] J.F. Nye, Some Geometrical Relations in Dislocated Crystals, Acta Metall. 1 (1953) 153–162.

[16] E.A.I. Ellis, M. Chmielus, S.P. Baker, Effect of sputter pressure on Ta thin films: Beta phase selection, texture, and stress, Acta Mater. 150 (2018) 317–326.

[17] E.A.I. Ellis, M. Chmielus, S. Han, S.P. Baker, In Progress, (2018).

[18] J.B. Shu, S.S. Clyburn, T.E. Mates, S.P. Baker, Effect of oxygen on the thermomechanical behavior of passivated Cu thin films, J. Mater. Res. 18 (2003) 2122.

[19] M.H.A. Nawaz, B.L. Mordike, Slip Geometry of Tantalum and Tantalum Alloys, Phys. Status Solidi. 32 (1975) 449–458. doi:10.1002/pssa.2210320213.

CHAPTER 6

Genetic algorithm prediction of geometrically necessary dislocation structure in phase-transformed tantalum thin films

Ari P. Kestenbaum[1], Elizabeth A. Ellis[2], and Shefford P. Baker[1,2]

[1]*Cornell University, Department of Materials Science and Engineering, Bard Hall, Ithaca, NY 14853*

[2]*Cornell University, Sibley School of Mechanical and Aerospace Engineering, Upson Hall, Ithaca, NY 14853*

This chapter is a draft of a paper being prepared for publication. My role in the work was helping to conceive of the work, providing technical content (particularly the individual parameterization scheme and orientation math), and co-advising Ari Kestenbaum during his Senior Thesis and Master's Thesis.

ABSTRACT

Tantalum films can form in either the stable bulk α phase or the metastable β phase found only in thin films. It has recently been shown that when a tantalum thin film transforms from β to α, it can form a unique microstructure with continuous orientation gradients and discontinuous orientation boundaries. Dislocation structures must be present in order to account for the lattice curvature associated with orientation gradients. In this work, a genetic algorithm approach is used to identify dislocation structures that can account for experimentally-observed orientation gradients. First, a method of generating smooth, noise-free orientation data that match key features of the actual phase-transformed microstructure is developed and validated by comparing model microstructure data with film data. Next, a genetic algorithm is developed that consistently generates dislocation structures that produce orientation maps with an average misorientation from the smooth orientation gradient of less than 2°. Multiple runs with different initial conditions converge to very similar dislocation structures (shapes, densities, and burgers vectors). The genetic algorithm model selects dislocations with two burgers vectors ([-1, -1, 1] and [-1, 1, 1]) for rotations in the plane of the film. The dominance of these dislocation types is

consistent with a kinetically limited mechanism previously proposed to explain the formation of orientation gradients in phase-transformed Ta films.

6.1. INTRODUCTION

Tantalum thin films are used in a wide variety of applications. In thin film form, tantalum can be deposited in one of two phases, α or β. The two have very different properties, and thus are suited to different applications. The stable bulk α phase is ductile, has low resistivity, and has a BCC crystal structure [1]. α-Ta films are used as diffusion barriers between copper and silicon in microelectronics [2–5] and in high-temperature wear-resistant coatings [6]. The metastable β phase, by contrast, has a tetragonal self-hosting σ-type Frank-Kasper structure [7], and is only found in thin films. It is often used in thin-film resistors [8–10] because of its high resistivity [1,11] and low temperature coefficient of resistance [10]. It is also susceptible to reactive ion etching [12] and, because tantalum absorbs x-rays well, β tantalum is used in x-ray lithography masks [12,13].

The metastable β phase will transform to α when heated [14,15].This phase transformation has been shown to occur via a nucleation-and-growth process [16], and is very sensitive to the oxygen content of the film [17]. It begins at about 300°C in oxygen-free films, and can be accompanied by a large stress change [14,16,18]. The microstructure that arises as a result of this phase transformation is very unusual and features long-range orientation gradients and discontinuous orientation boundaries, and was first described by Baker *et al*. [16] (henceforth BKJA). Figure 6.1 shows electron backscatter diffraction (EBSD) orientation data, colored by out-of-plane (OOP) orientation according to the inset stereographic triangle, for a typical phase-transformed α-Ta film (from [19]).

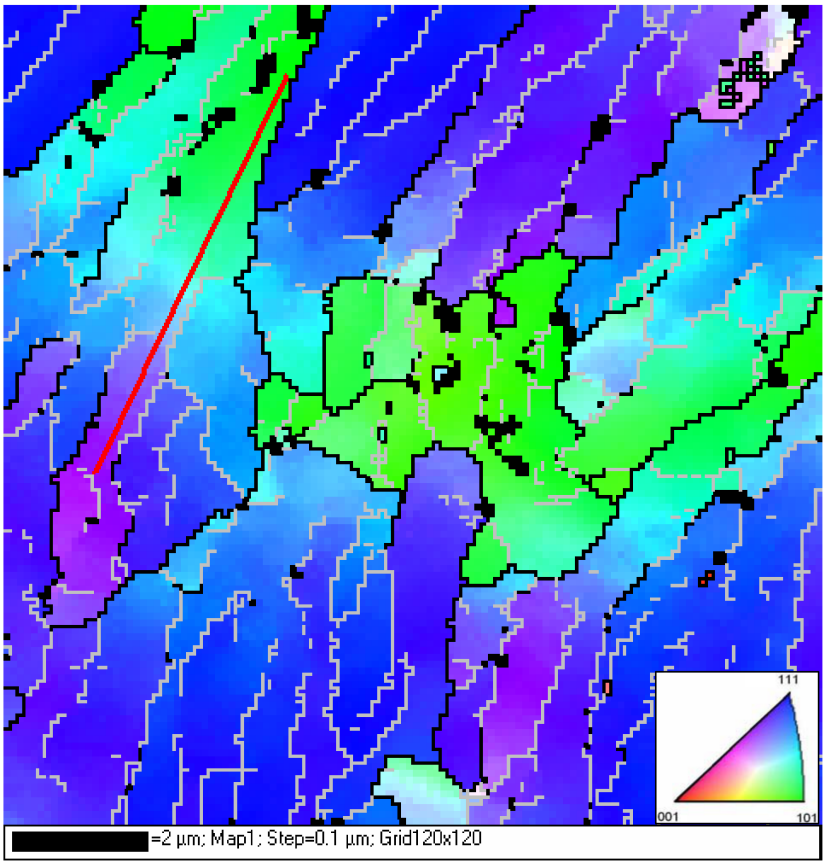

Figure 6.1: EBSD map showing out-of-plane orientation in a phase-transformed α-Ta film. The microstructure features continuous, long range orientation gradients and discontinuous orientation boundaries. From [19].

Orientation boundaries of 8° between pixels are shown in black, and those between 4° and 8° are shown in grey. Following the red line in Figure 6.1, the orientation changes gradually from an orientation near (211) to one near (110), without crossing a single misorientation boundary greater than 4°. Additionally, orientation boundaries are discontinuous, starting in the middle of the film as a low-angle boundary, transitioning to a high-angle boundary, then becoming a low-angle boundary, and ultimately ending in the middle of the film. This microstructure is quite unlike the canonical polycrystalline microstructure in which grains of a single orientation are separated by continuous high-angle boundaries.

Previous work has acknowledged that dislocations are required to form the orientation gradients observed in this unusual microstructure[16,18]. Baker *et al*. [16] have shown that dislocations in reasonable densities can produce the orientation gradients observed in phase-

transformed Ta films, and also suggest a possible mechanism by which the necessary dislocations might be introduced. Briefly, they suggest that the density difference between the β and α phases of Ta would lead to a surface step at the phase boundary, and that kinetic limitations on self-diffusion might prevent certain lattice planes in the growing α region from being completed. This would leave edge dislocations with their sense vectors parallel to the phase boundary. Observed gradients are consistent with this model, as rotation axes tend to lie in the plane of the film, and parallel to <211> crystal directions [16].

Meanwhile, Ellis et al. [18] (henceforth ELCB) studied systematic variations in the magnitude and extent of the orientation gradients in phase-transformed α-Ta microstructures caused by variations in the microstructure of the as-deposited β-Ta films induced by depositing at different sputter pressures [20,21]. In many cases, the orientation gradients form regular patterns, such as alternating stripes of (111) and (110) orientations. They propose a nucleation-and-growth sequence that could explain several of these texture patterns: α-Ta nucleates with a (111) out of plane orientation, then rotates about axes lying in the plane of the film and perpendicular to the growth direction, until this growing "daughter region" meets another daughter region and forms a high-angle boundary. However, the specific dislocations leading to the proposed rotations are unknown.

Dislocations that are required for lattice curvature are known as geometrically necessary dislocations (GNDs) and were first formulated as a tensor describing the 'state of dislocation' at a point by Nye [22]. The GND framework has been applied to both bulk materials [23–28] and thin films [29–32] as a way to understand strain gradient plasticity [33–36]. Orientation gradients are sometimes reported with GND analysis [37–40], but these works are generally concerned with the effect of GNDs on hardness and yield stress, as nearly all of these samples have been heavily deformed. The only previously observed orientation gradients that are not caused by deformation are reported by Maeder *et al.* [40], who performed laser annealing of silicon and calculate total GND densities on the order of $10^{12}/m^2$.

To understand the orientation gradient microstructure in phase-transformed α-Ta, it is necessary to find not just the total geometrically necessary dislocation density, but the specific dislocations that make up the microstructure. Kysar et al. [28] have used EBSD to identify specific slip systems in wedge-indented single-crystal Cu by parameterizing the Nye tensor in terms of a few dislocations, but the phase-transformed microstructure in Fig. 1 provides no obvious choice of slip system for parameterization. In addition, the resolution and precision of EBSD provides an a-priori constraint on this approach as the average pixel-to-pixel misorientation in some areas of the microstructure is on the same order as a typical error ($\pm$ 0.1˚) in the EBSD measurements.

In this article, we instead use a genetic algorithm approach to identify specific dislocation arrays that could be responsible for the orientation gradient microstructure seen in phase-transformed α-Ta films (e.g. Fig 1 and images in [18]). Genetic algorithms (GAs) are a subset of evolutionary computation and have been successful in a remarkable number of fields, including the design and optimization of race cars [41], satellite antennas [42], molecular geometry [43], thermal control of buildings [44], water distribution networks [45], and electromagnetic devices [46]. Materials science applications include generating grain boundary configurations in bicrystals [47], interface structure prediction in multicomponent systems [48], and finding low-energy structures of symmetric tilted grain boundaries in Si [49]. However, no GA has previously been created for dislocation structure generation.

Below, we analyze a specific texture pattern ("triangles") reported by ELCB. [18] and attempt to identify specific dislocation arrays that could lead to this pattern as an example. We first develop a model microstructure in which orientation gradients are smooth and continuous that otherwise replicates all important aspects of the experimentally observed microstructure. We then used a genetic algorithm to identify dislocation arrays that can produce this smooth model microstructure. Understanding the dislocations underlying this structure will help to inform our understanding of how this unusual structure forms.

6.2. MODEL MICROSTRUCTURE

In this article we focus on a single texture pattern in phase-transformed α-Ta films reported by ELCB [18]. To avoid problems created by data resolution and measurement error, we create a smoothed model microstructure that replicates this prominent texture pattern with arbitrarily fine orientation resolution.

The pattern that we modeled is shown in Figure 6.2b [18].

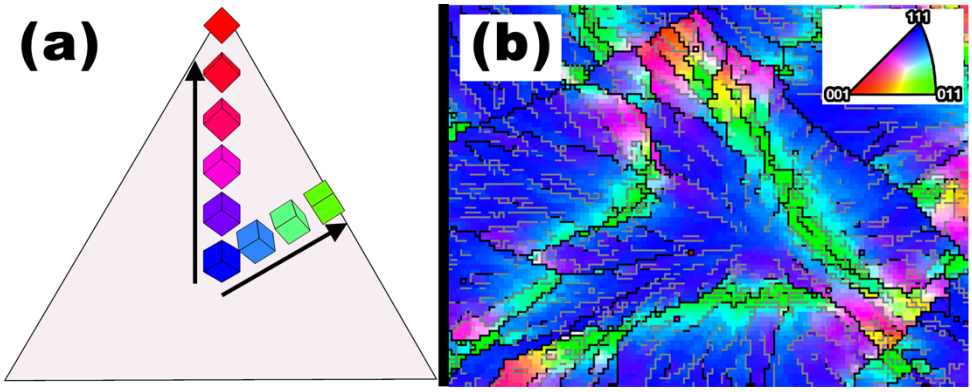

Figure 6.2: Triangular texture pattern in phase-transformed film, and rotation scheme by which it might form. From [18].

The texture pattern consists of a triangle, about 35 μm wide and 30 μm tall, with a (111) orientation in the center surrounded by (100)-oriented vertices and (110)-oriented edges. As suggested in ELCB [18], these particular orientations may be reproduced via a simple rotation mechanism, illustrated in Figure 6.2a. Beginning in the center of the triangle with a (111) out-of-plane orientation, the crystal rotates outward as we move away from the center along any radius; that is, the crystal rotates about axes lying in the plane of the film and perpendicular to the direction of travel. Moving toward the vertices, the film passes through a (211) orientation to a (100) orientation, and moving toward the edges it passes through (221) to (110).

We can generate a model microstructure using this mechanism, by following the procedure illustrated in Figure 6.3.

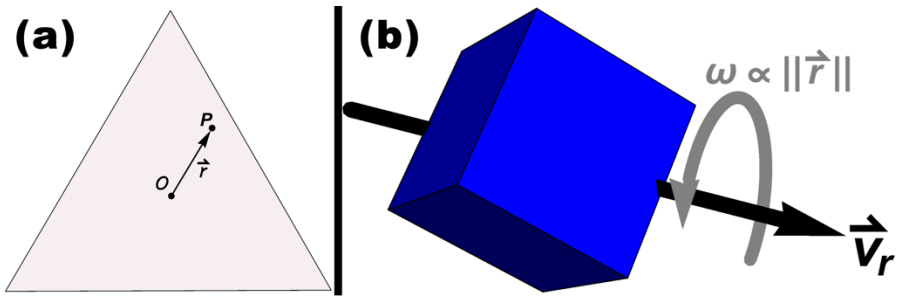

Figure 6.3: Schematic showing how orientation data are generated for the smoothed model microstructure. (a) A point P is selected at which to compute the orientation; O is the origin;and ***r*** *is the radial vector (b)The cube represents the starting orientation.* $\mathbf{v_r}$ *is the axis of rotation, which is perpendicular to* ***r*** *and lies in the plane;* ω *is the magnitude of rotation and is a function of the distance between P and O.*

Figure 6.3a shows the selection of a point *P,* in cylindrical coordinates, at which to compute the orientation, where *O* is the origin and $\vec{r}$ is the radial vector. Figure 6.3b is an illustration of the actual computation, which involves rotating the starting orientation, represented by the cube, about the axis of rotation $\vec{v}_r$ by an angle ω. The axis of rotation is perpendicular to the radial vector and lies in the plane, and the magnitude of rotation is a function of the distance between *O* and *P*. These steps are repeated for all points in the triangle.

As a simple first approximation, we make the rotation angle ω simply proportional to $|\vec{r}|$. The orientation Θ at a point P may therefore be written in axis-angle form and cylindrical coordinates:

$$\Theta(r,\theta,z) = \begin{cases} \hat{n} \\ \omega_{111} \end{cases} = \begin{cases} \frac{\bar{P}-\bar{O}}{\|\bar{P}-\bar{O}\|} \times \hat{z} \\ k\|\bar{P}-\bar{O}\| \end{cases} \tag{6.1}$$

where $\hat{n}$ is the axis of rotation, ω_{111} is the angle of rotation from the initial (111) out-of-plane orientation, and *k* is a proportionality constant.

The microstructure produced by this mechanism is shown in Figure 6.4.

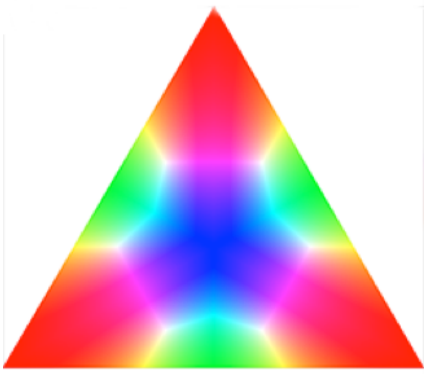

Figure 6.4: Model microstructure created by rotating outward from (111) center at constant rate.

While this constant rotation rate microstructure provides a good match to the symmetry of the experimental texture pattern in Figure 6.3b in that the vertices have a (100) orientation and the edges have a (110) orientation, the relative areas of (111)-, (110)-, and (100)-oriented material are not correct. To address these issues, we modify the rotation rate as follows.

$$\theta' = 15\cos(\theta/19) + \theta \tag{6.2}$$

$$\bar{P}'(r,\theta',z) = \begin{cases} r \\ \theta' \\ z \end{cases} \tag{6.3}$$

$$d = \frac{\tan^{-1}(\sqrt{2})}{2}\left(\sqrt{3}\sin(2\theta') + 3\cos(2\theta')\right)^{-\frac{1}{2}} \tag{6.4}$$

$$\Theta' = \begin{cases} \hat{n}' \\ \omega_{111}{}' \end{cases} = \begin{cases} \frac{\bar{P}\prime - \bar{O}}{\|\bar{P}' - \bar{O}\|} \times \hat{z} \\ \frac{d}{\sqrt{2}}\sqrt{1 + erf\left(\frac{r - 5 - 4\cos\left(30 TriangleWave\left(\theta'/240 + 1/8\right)\right)^{40}}{\frac{d + 10^{-20}}{4}} - 2\right)} \end{cases} \tag{6.5}$$

The component that modifies the magnitude of rotation at each point is a complex sigmoidal function. This allows for slow rotation rates near the center of the triangle, which is all near (111), smoothly increasing to rapidly rotate through (122), and then slow down near the edge of the triangle for a broader (011) region. A similar logic applies to rotating from (111) through (112) to (001) vertices. All functions are empirically chosen.

The microstructure produced using these equations, henceforth called the model microstructure, is shown in Figure 6.5 alongside measured orientation data from ELCB [18].

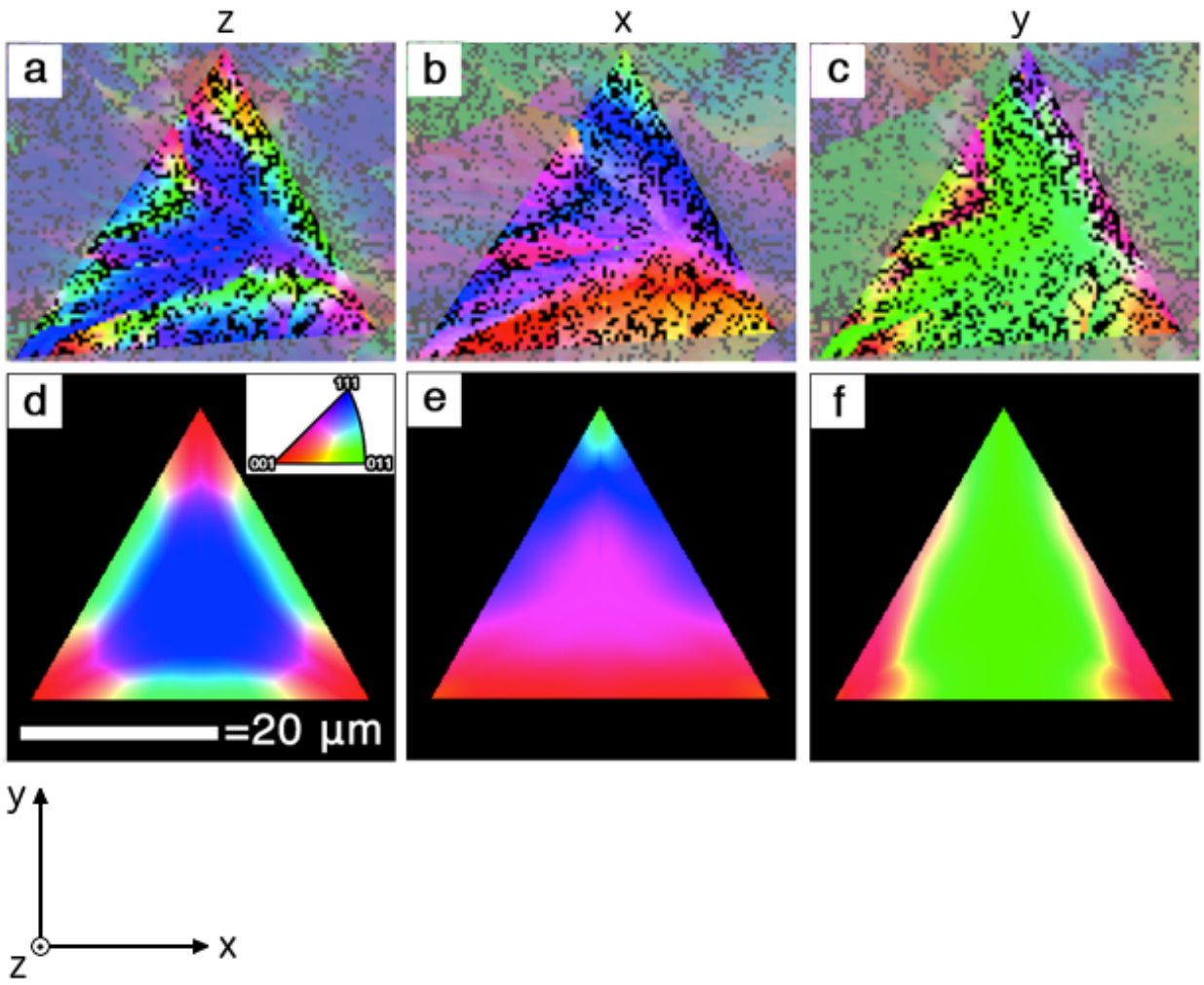

Figure 6.5: Full orientation data for measured microstructure (from ELCB [18]*) (a-c) and model microstructure (d-f). Figure 6.5 a and d show orientation in the sample z direction (OOP), b and e show orientation in the sample x direction, and c and f show the orientations in the sample y-direction.*

Figure 6.5 a-c show measured orientation data from the film, which has been replotted to show out-of-plane and in-plane orientation: that is, each column shows the crystallographic direction parallel to one of three sample coordinate axes. Fig 6.5a shows the same out-of-plane orientation (sample *z* direction) as in Figure 6.2, and Figs 6.5 b and c show the orientation at each pixel in the sample *x* and *y* directions respectively. Figure 6.5 d-f show calculated orientation data from the model microstructure, in the same three sample directions. We use the original uninterpolated orientation data from ELCB [18] to ensure that our model microstructure is tuned to match real measured orientations. The model microstructure now matches the spatial distribution of orientations as well as the triangular symmetry. This indicates both that our model microstructure

fully reproduces the orientation relationships seen in the film, and that the simple rotation mechanism proposed earlier [18] can produce this microstructure.

Both the measured microstructure and the film microstructure have three-fold symmetry. This symmetry is obvious in Figure 6.5 a and d, but not in b, c, d or e. This apparent loss of symmetry is merely the effect of representing this pattern, which has three-fold symmetry, in terms of a coordinate system with four-fold symmetry. Figure 6.6 shows the symmetry of the triangular texture pattern in the form of cubes colored by out-of-plane orientation:

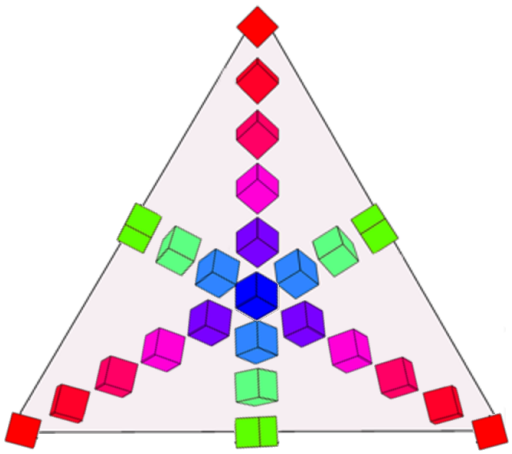

Figure 6.6: Orientation symmetry in triangular texture pattern.

Consider the orientation at each vertex: All three vertices have a (100) out-of-plane orientation, but the in-plane angle measured between the $\hat{x}$ sample direction and a (100) crystal plane are different—15°, 45°, and 75° going counter-clockwise from the bottom left. This means that a representation such as an orientation matrix, or the three EBSD images shown in Figure 6.5, show different orientations at the three vertices. If, however, we rotate the entire triangular texture pattern by 120°, the orientation at every point will be the same, regardless of how we choose to represent it. We take advantage of this symmetry by studying only one-sixth of this original triangular pattern in Sections 6.3 and 6.4. This subsection is shown in Figure 6.7.

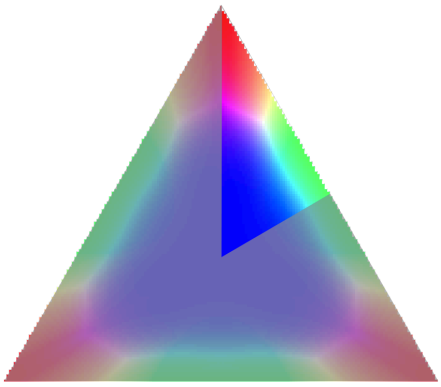

Figure 6.7: Section of triangular texture pattern used in genetic algorithm model.

The orientation data from the smooth model and the corresponding region of the film are shown as pole figures in Figure 6.8.

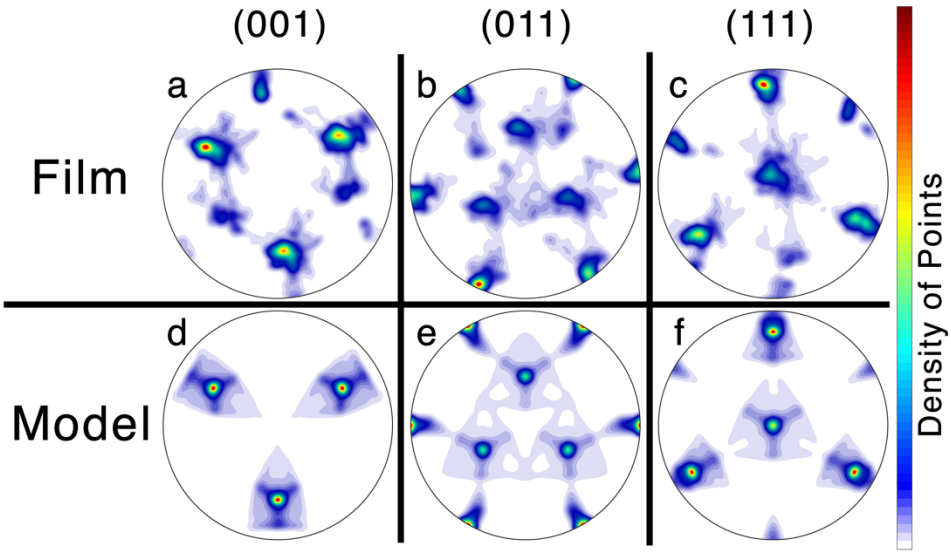

Figure 6.8: Pole figures for film and model microstructure.

Figures 6.8a–c show measured film data while Figures 6.8d–f show model microstructure data. Figures 6.8a and d show (001) pole figures, b/e show (011) pole figures, and c/f show (111) pole figures. Once again, the model microstructure orientation resembles the experimental microstructure in all important respects. The (111) pole figures in Figure 6.8c have high-density regions near the periphery of the pole figure with small low-density regions directly opposite. The model microstructure shows that this is not a separate population of (111) grains rotated 60° in the plane of the film, but rather an effect of the orientation gradient. As the orientation changes and one of the (111) poles crosses over the edge (*i.e.*, dips below the base plane of the

pole figure), another one emerges directly opposite it, and appears as a small peak on the pole figure.

6.3. GENETIC ALGORITHM MODEL

To identify dislocation structures consistent with the model microstructure, we created a genetic algorithm. Genetic algorithms (GAs) are an optimization technique that mimics evolution by incorporating the principles of natural selection, inheritance of genetic material, crossover, and mutation. Candidate solutions, called individuals, pass down their genetic material, represented as parameter encodings, to a number of offspring. Each individual is a potential solution generated by the algorithm, and all of the individuals are collectively referred to as a population. In this case, an individual will consist of an array of dislocations, with both position and character specified. Each iteration of the algorithm produces a new population, and the population from a particular iteration of the algorithm is called a generation. Each individual is evaluated according to a fitness function that determines whether the individual will pass its genetic material on to the next generation. Examples of criteria that may be used in a fitness function include cost, weight, and efficiency. It is possible to evaluate fitness based on multiple criteria, and an algorithm that does this is called a multi-objective genetic algorithm [50]. Our algorithm will evaluate fitness based on how well the individual dislocation array replicates the target orientation pattern (misorientation) and minimizes total geometrically necessary dislocation density. An individual with a high fitness will produce more offspring than one with a low fitness, and, as in evolution, this ensures that beneficial parameter encodings (genes) are more likely to be passed down from one generation to the next and spread throughout the population. The process by which individuals produce offspring involves crossover, which combines the genetic material from two individuals, and mutation, which makes small, random changes to the encoding of an individual and introduces new genetic material to the population to prevent the algorithm prematurely converging on a less-fit solution. .

GAs have several advantages over other optimization techniques for this problem. If implemented properly, GAs are unlikely to converge prematurely because they start with and maintain a diverse population, which allows them to explore a larger area of the search space, making it more likely that the algorithm will find global minima without being trapped in local minimum solutions. GAs make no restrictive assumptions about the search space of any particular problem, which is particularly useful for early attempts at solving a problem when little is known, Unlike many optimization techniques—even similar ones such as simulated annealing—GAs are easy to parallelize, because the most computationally intensive section of the algorithm (the fitness function) can be evaluated separately for each individual. Lastly, GAs often produce robust solutions in the sense that small changes to the encoding of individuals after many generations will not typically have a drastic effect on its fitness as similar solutions will have already been explored. Generating dislocation arrays consistent with the phase-transformed Ta microstructure is an early attempt at solving a problem with a large and complex solution space about which little is known, and a genetic algorithm is therefore an attractive approach.

The genetic algorithm model was written in Python, taking advantage of available software packages to improve both development time and run time. In particular, the Distributed Evolutionary Algorithms in Python, or DEAP, package [51] provides an excellent framework for creating GAs, and the Scalable COncurrent Operations in Python, or SCOOP, package [52] enables easy parallel and distributed computation. The standard NumPy [53], SciPy [54], and Matplotlib [55] packages were also used.

Each “individual” in this genetic algorithm is a dislocation array within the small triangular region shown in Figure 6.7. The fitness function, used to determine whether an individual passes its genetic material on to the next generation, includes both the total dislocation density of the individual array, as well as the average misorientation between the model microstructure orientation field and the orientation field associated with the individual dislocation array.

6.3.1. Individual Encoding

Each individual is defined by two arrays of dislocations. The first is an array of dislocations lying in the plane of the film. To avoid interactions between dislocations, we require that these dislocations do not cross one another. We achieve this by defining the dislocation lines as contours on a three-dimensional surface, i.e. level sets.. We can therefore change the position and shape of the dislocation lines by changing the shape of this three-dimensional surface. The three-dimensional surface serves only to define the paths of the dislocations in the plane of the film. The form of the three-dimensional surface was chosen to replicate certain features of the smooth orientation field, namely that the orientation changes slowly in the center and rapidly near the edges. This indicates that a higher dislocation density is required near the edges. One way to achieve this is to use a three-dimensional surface that is steep near the edges and shallow in the center, with contour lines spaced evenly along the z-direction. Conveniently, we already have such a function: the function used to define the rotation at each point in the model microstructure, given in Equations 6.2-6.5. We then modify the shape of the three-dimensional surface by adding noise in the form of three-dimensional Gaussian peaks at random locations. By changing the position and amount of noise, we allow the contour lines to move. The three-dimensional surface defining the in-plane dislocation lines is shown in Figure 6.9.

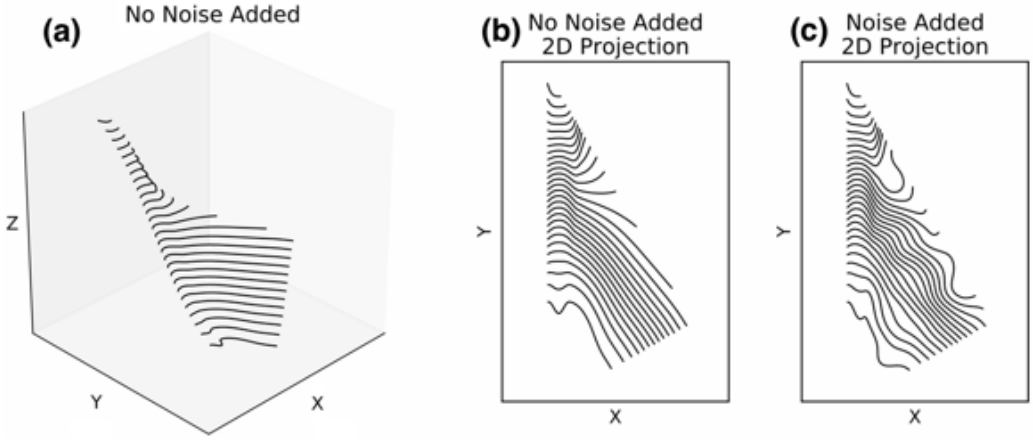

Figure 6.9: Three-dimensional function whose contours define in-plane dislocation lines. a) 3D view of base function without added noise, b) projection of noise-free contour lines into the plane of the film, c) contour lines of 3D surface with added noise.

Figure 6.9a shows the three-dimensional surface, where the *x* and *y* directions are the same *x* and *y* directions describing the surface of the film, and the *z* direction is an arbitrary height used only to define the locations of the contours. Figure 6.9b and c show the projection of these contour into the plane of the film, where they define the paths of dislocations lying in the plane of the film. Figure 6.9b shows the original contour lines without added noise, and Figure 6.9c shows how the dislocation lines move when noise is added to the three-dimensional surface. Each contour line was then assigned a ⟨111⟩-type burgers vector and considered to represent a bundle of 25 parallel dislocations to reduce computation time. The in-plane dislocations are defined by four parameters: the number of Gaussian noise peaks added to the three-dimensional surface, the location of the noise peaks, the number of contour lines on the three-dimensional surface, and the list of burgers vectors for each contour line.

The rotations associated with the in-plane dislocations will always occur about axes lying in the plane of the film. To allow for rotations about out-of-plane axes, we also include a set of out-of-plane dislocations. These always have their sense vector parallel to the film normal direction, so they are defined by only three parameters: the number of out-of-plane dislocations, their locations, and the burgers vector for each dislocation. Each entry in the out-of-plane dislocation list represented a bundle of three dislocations.

6.3.2. Fitness Function

To evaluate the success of each individual dislocation array solution, we must define a fitness function. Each individual is weighted by its total dislocation density, which should be minimized to minimize stored strain energy, and by the degree to which its associated orientation field matches the model microstructure orientation field. This requires that we calculate the orientation field associated with each dislocation array. We first assigned the orientation in the center of the original triangle to have a (111) out-of-plane orientation matching the model microstructure orientation field, and then used the Nye tensor to calculate the change in orientation associated with each dislocation bundle. We then calculated the average of the

misorientations between each point in the individual orientation field and the model microstructure orientation field. Dislocation density was calculated by summing the lengths of all dislocation lines. The final fitness function was a weighted average of the average misorientation and dislocation density.

6.3.3. Initialization, Selection, Crossover, and Mutation

Each parameter was initialized randomly within a particular range because the algorithm was observed to almost always converge on a value within that range across multiple runs, and setting the parameters to a value outside the range resulted in a longer convergence time. The initial number of IP dislocations (contour lines) was randomly selected between 75 and 150. The burgers vector for each IP dislocation was initially chosen randomly from the eight ⟨111⟩ directions during model development, but when became apparent that the algorithm was selecting only [-1,-1,1] and [-1,1,1], we restricted the algorithm to these two burgers vectors in order to reduce convergence time (see Section 6.4). The number of points of noise added to the level set function was randomly selected between 20 and 75. The locations of the noise points and OOP dislocations were randomly selected to be anywhere inside the triangle in order to allow the algorithm as much freedom to change the shape of the IP dislocations as possible. The number of OOP dislocations was randomly selected between 100 and 1000, and the burgers vectors for the OOP dislocations were randomly selected from all eight ⟨111⟩ directions.

Tournament selection [56] was used to determine which individuals would reproduce to make the next generation because it is algorithmically simple, straightforward to parallelize, and allows for easy adjustment of selection pressure.

Crossover operated on four of the seven parameters: the burgers vectors of the IP dislocations, the locations of the noise points, the locations of the OOP dislocations, and the burgers vectors of the OOP dislocations. Crossover operated by randomly selecting between 35% and 65% of the genetic material for each parameter to exchange between individuals. Where the length of a particular parameter differed between individuals, the percentage was

defined by the length of the shorter parameter. Crossover was performed separately on the list of burgers vectors of the IP dislocations and the list of noise points, but the location and burgers vector of the OOP were linked. Crossover did not change the number of IP dislocations, the number of noise points, or the number of OOP dislocations.

Mutation operated on all seven parameters, and each individual had a 25% chance of being mutated. The number of IP dislocations could randomly increase or decrease by up to 5; up to 15 IP dislocations could have their burgers vector randomly reassigned; the number of noise points could randomly increase or decrease by up to 10; up to 10% of the noise points could have their coordinates changed by up to 1 μm in the *x* or *y* direction; the number of OOP dislocations could increase or decrease by up to 50; and up to 50 OOP dislocations could have their burgers vectors randomly reassigned.

6.4. Results

Figure 6.10 shows a multi-generation statistics plot for a run of the genetic algorithm model.

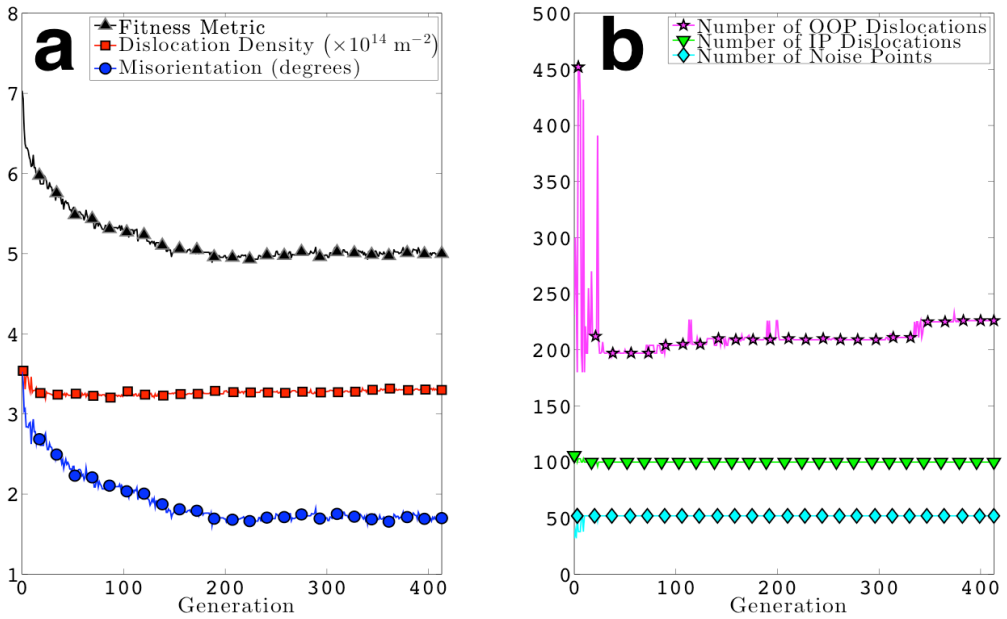

Figure 6.10: Multi-generation statistics plot for a single run of the genetic algorithm. a) fitness function, dislocation density and misorientation, b) OOP dislocations, IP dislocations, and noise points.

Figure 6.10a shows the misorientation, dislocation density, and overall fitness metric of each generation, and Figure 6.10b shows the number of IP and OOP dislocations, as well as the

number of points at which noise was added to the level set function. The misorientation in Figure 6.10a decreases rapidly during the first 40 generations, then slows, remaining steady after 250 generations, while the dislocation density decreases during the first 100 generations and then remains steady. These are typical patterns for the misorientation and dislocation density, where the number of generations to convergence varying between approximately 150 and 600. In Figure 6.10b, the number of noise points and the number of contour levels do not change significantly throughout the run, which is typical. However, the number of OOP dislocations changes substantially throughout the run.

Mutation rates and initial parameters affect only convergence time, not the fitness of the converged population. The three most important mutation parameters are the number of pole dislocations, their burgers vectors, and the locations where noise is added. The other three parameters—the number of noise points, the number of IP dislocations, and the burgers vectors of the IP dislocations—do not change very much throughout a particular run regardless of their mutation rates. Noise points tend to converge on similar locations.

Typical results of the genetic algorithm are shown in Figure 6.11.

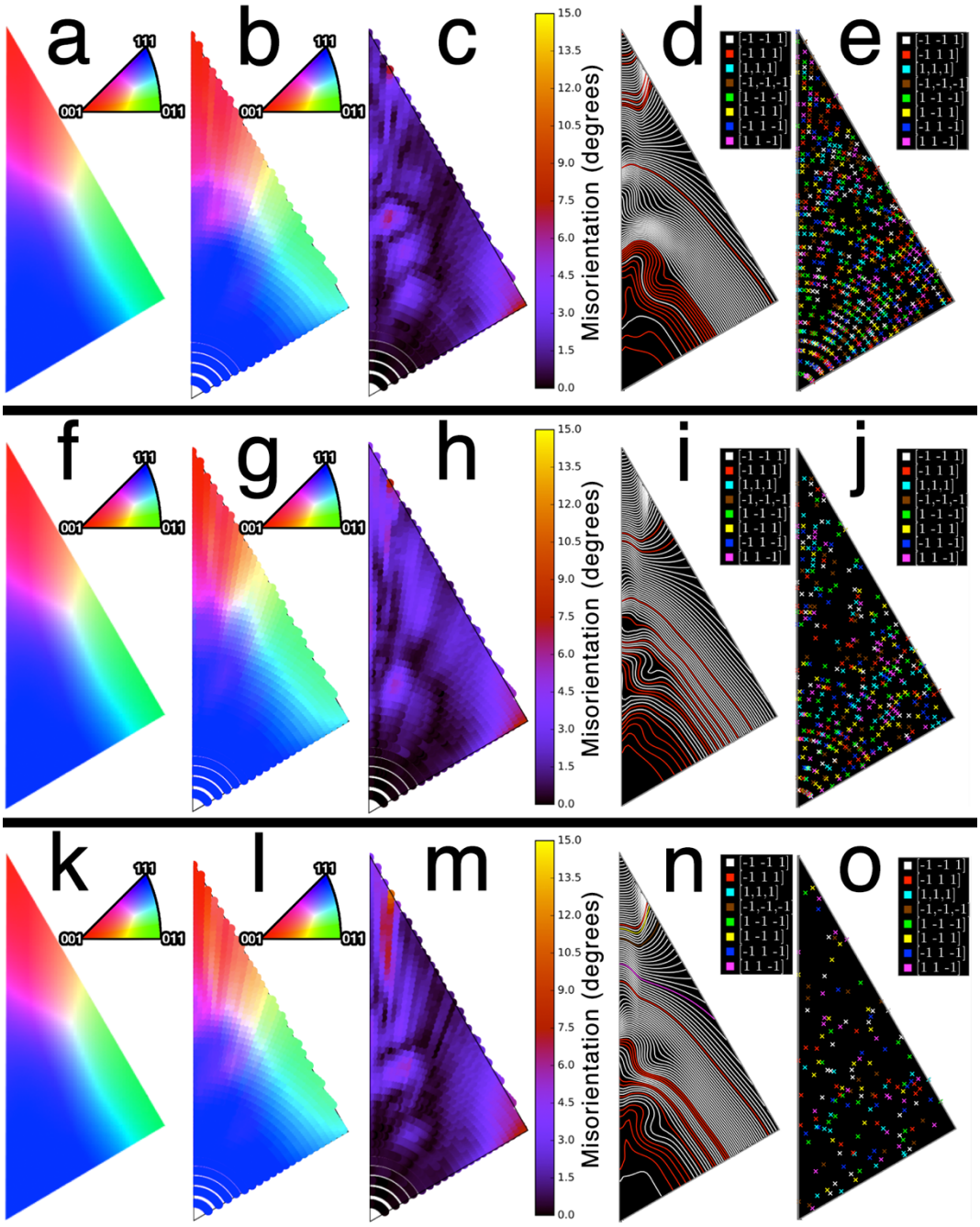

Figure 6.11: Three individuals selected by the genetic algorithm. a/f/k: Desired orientation field, b/g/l: selected orientation field, c/h/m: misorientation, d/i/n: location and burgers vectors of in-plane dislocations, e/j/o: location and burgers vectors of out-of-plane dislocations.

Each row of Figure 6.11 shows aspects of a single individual dislocation array solution. First, from left to right, is the desired out-of-plane orientation field, from the smooth model microstructure. Next is the orientation field associated with the individual dislocation array. The third column shows the point-by-point misorientation between the model microstructure

orientation and the genetic algorithm solution orientation. The fourth column shows the locations of the in-plane dislocations and the burgers vectors associated with each one, and the final column shows the locations and burgers vectors of the out-of-plane dislocations.

Across multiple runs the genetic algorithm model converges on a similar pattern of in-plane dislocations. Most of the in-plane dislocations are smooth except near the middle left side of the triangle, where several dislocations form tight curves. Two burgers vectors are selected almost exclusively: dislocations with $[\bar{1}11]$ burgers vectors are concentrated in the lower left portion of the triangle, while dislocations with $[\bar{1}\bar{1}1]$ burgers appear elsewhere. Neither the burgers vectors nor the locations of the out-of-plane dislocations show noticeable patterns. The average misorientation ranges from 1.39° to 1.61°, and the dislocation density ranges from 3.21 to 3.45 x 10^{14} m^{-2}.

The relative weight of misorientation and dislocation density in the overall fitness metric does not have a large effect on the results of the algorithm. Due to the construction of the fitness function, the relative weight of dislocation density and misorientation can change as the run progresses, because the misorientation typically has a much larger relative change throughout the duration of a run than does the dislocation density. The average misorientation typically begins near 4° for the first generation, but eventually falls to below 2°. In contrast, the dislocation density rarely changes by more than 10% throughout a run. This means that throughout the run the relative weight of the dislocation density slowly increases.

6.5. DISCUSSION

In-plane dislocations with $[\bar{1}\bar{1}1]$ and $[\bar{1}11]$ burgers vectors dominate in the dislocation arrays produced by the genetic algorithm. To explore the role of these two burgers vectors, we ran the algorithm using only these two burgers vectors for the IP dislocations, and again excluding these two burgers vectors (i.e. only the other 6 <111>-type burgers vectors were allowed). The resulting dislocation arrays are shown in Figures 6.12 and 6.13.

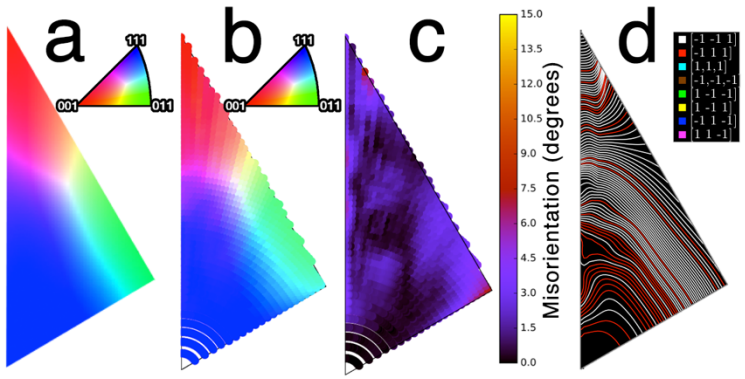

Figure 6.12: Results of genetic algorithm with in-plane burgers vectors ***restricted to*** $[\bar{1}\bar{1}1]$ *and* $[\bar{1}11]$. *a: desired orientation, b: genetic algorithm orientation, c: misorientation, d: location and burgers vectors of in-plane dislocations.*

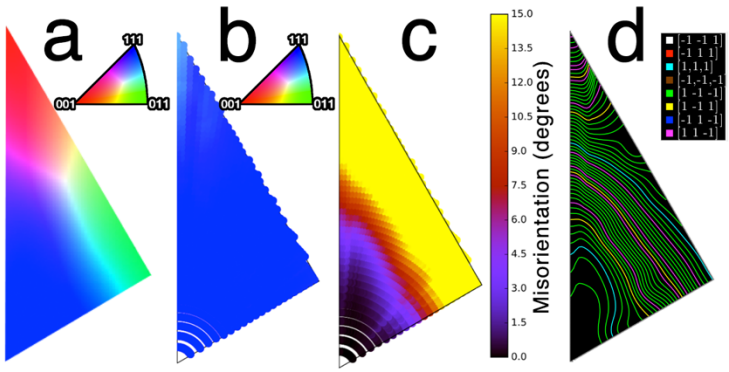

Figure 6.13: Results of genetic algorithm with in-plane burgers vectors $[\bar{1}\bar{1}1]$ *and* $[\bar{1}11]$ ***excluded****. a: desired orientation, b: genetic algorithm orientation, c: misorientation, d: location and burgers vectors of in-plane dislocations.*

While the individual in Figure 6.12 provides a good match to the desired orientation, the one shown in Figure 6.13 cannot match the model microstructure at all. Only in-plane rotations seem to be allowed, as the out-of-plane orientations are virtually all (111) over the entire region. This is consistent with our speculation that the triangular feature is formed by rotations about axes lying in the plane of the film, as the only difference between the successful arrays in Figures 6.11 and 6.12 and the unsuccessful one in 6.13 is the absence of those burgers vectors that permit such rotations.

The out-of-plane dislocations, on the other hand, do not form any obvious pattern. The out-of-plane dislocations are included to allow for rotations in the plane of the film, which must arise as a consequence of the growth mechanism proposed in ELCB [18]. As orientation rotates continually about axes in the moving phase boundary, neighboring points will develop larger and

larger misorientations. These misorientations could be accommodated by elastic strains, dislocations with their sense vectors out of plane, or by orientation boundaries, The required strains would certainly be unphysically large, so we determined to include a population of out-of-plane dislocations which could arrange themselves into low-angle boundaries. However, the out-of-plane dislocations selected by the genetic algorithm do not form boundaries or any other recognizable pattern, so we conclude that there are multiple configurations that are similarly effective.

The dislocation densities generated by this genetic algorithm model are comparable to GND densities in real systems. For example, Kysar *et al.* [28] performed wedge indentation on single-crystal Cu and Al, after which they observed orientation gradients of up to approximately 0.4°/μm, and GND densities ~10^{13} m^{-2}. The phase-transformed Ta films have orientation gradients approximately an order of magnitude larger, about 4°/μm, and the dislocation densities generated by the genetic algorithm model are approximately an order of magnitude larger as well, ~10^{14} m^{-2}. Demir *et al.* [38] deformed nickel by equal channel angular pressing and observed orientation gradients slightly larger than those of the phase-transformed films, ~10°/μm, and calculated GND densities slightly larger than those of the genetic algorithm model, ~10^{15} m^{-2}. A key difference between the phase-transformed films and the work by Kysar *et al.* and Demir *et al.*, however, is that their samples are heavily deformed whereas the tantalum films are not.

The genetic algorithm used here divides the dislocation array into two independent groups, one with sense vectors lying in the plane of the film, and one with sense vectors normal to the film. In reality, it is unlikely that the dislocations present in the real films are so organized. In fact, the results of the genetic algorithm suggest that we must consider the film as a three-dimensional object. Our analysis shows that in-plane dislocations with [-1 -1 1] and [-1 1 1] burgers vectors are required to produce the types of rotations seen in the portion of the triangular pattern we modeled. However, it is clear that these same dislocations must produce exactly the wrong types of rotation in other sections of the triangle. These dislocations cannot stop in the

middle of the triangle, which has no internal orientation boundaries, and so must turn and exit out the top or bottom of the film, becoming out-of-plane dislocations. Modeling these three-dimensional dislocation lines will require significant alteration of the model.

The mechanism proposed by Baker et al. [16] is still the best available explanation for how the orientation gradients observed in phase-transformed Ta might form. According to this model, the difference in density between the β and α phases causes a step to form at the surface of the film, and as the phase boundary moves through the film the surface step must follow. This means that some amount of material must travel down the height of the surface step before it is able to join a growing α-Ta lattice plane. If diffusion rates are slow enough to interfere with this process, some of these lattice planes will not be completed and will form edge dislocations lying approximately in the plane of the film. If this process occurs around the entire boundary of a growing α-Ta region, we would expect a trail of dislocations left behind along the path of the phase boundary, and the rotations produced would tend to cause rotations away from the center of the α nucleus. This is consistent with the in-plane dislocation arrays produced by the genetic algorithm, which form concentric bands around the initial (111) center of the triangle pattern. The out-of-plane dislocations might therefore be regarded as a consequence of the strains that must arise from continual in-plane rotations,

6.6. SUMMARY AND CONCLUSIONS

When tantalum thin films are phase transformed from β to α they exhibit orientation gradients as high as 4°/μm over tens of μm. Dislocations must be present in order to account for these orientation gradients, and in this article, we attempt to understand the structure of these required dislocations. We first generated an artificial microstructure with has smooth orientation gradients that replicates a prominent pattern in the microstructure of the phase-transformed tantalum films. We then created a genetic algorithm that generates dislocation structures that account for the orientation gradients in the orientation data in the model microstructure.

The model microstructure was generated by rotating outward from a (111)-oriented center orientation. The close match between the model microstructure and EBSD orientation data from the phase-transformed film, as validated by orientation maps and pole figures, shows that this radial process can account for observed orientation gradients. The genetic algorithm model then generates dislocation arrays that match the orientation of the model microstructure as closely as possible. The genetic algorithm model uses dislocation density and average misorientation to evaluate each dislocation structure, and consistently converges on similar dislocation structures with similar misorientations and dislocation densities across multiple runs. The genetic algorithm model also consistently selects two dislocation types, with $[\bar{1}\bar{1}1]$ and $[\bar{1}11]$ burgers vectors and sense vectors in the plane of the film, which are shown to be necessary for the orientations produced by the dislocation structure to match those of the smooth analytical model. The dislocations in the model have also been linked to a proposed mechanism that could explain the origin of the orientation gradients in phase-transformed Ta films.

6.7. ACKNOWLEDGMENTS

Support for this work was provided by the National Science Foundation (DMR 0706507 and DMR 1106223). This work also made use of the facilities of the Cornell Center for Materials Research with support from the National Science Foundation Materials Research Science and Engineering Centers program (DMR 1120296). The authors would also like to thank Michael Thompson for his ideas and insights about modeling, and his recommendation of using a genetic algorithm to create dislocation structures.

6.8. REFERENCES

[1] S.L. Lee, M. Doxbeck, J. Mueller, M. Cipollo, P. Cote, Texture, structure and phase transformation in sputter beta tantalum coating, Surf. Coatings Technol. 177–178 (2004) 44–51. doi:10.1016/j.surfcoat.2003.06.008.

[2] K. Holloway, P.M. Fryer, Tantalum as a diffusion barrier between copper and silicon, Appl. Phys. Lett. 57 (1990) 1736. doi:10.1063/1.104051.

[3] L.A. Clevenger, N.A. Bojarczuk, K. Holloway, J.M.E. Harper, C. Cabral, R.G. Schad, F. Cardone, L. Stolt, Comparison of high vacuum and ultra-high-vacuum tantalum diffusion barrier performance against copper penetration, J. Appl. Phys. 73 (1993) 300–308.

[4] T. Laurila, K. Zeng, J.K. Kivilahti, J. Molarius, I. Suni, Effect of oxygen on the reactions in the Si/Ta/Cu metallization system, J. Mater. Res. 16 (2001) 2939–2946. doi:10.1557/JMR.2001.0404.

[5] J.S. Fang, T.P. Hsu, M.L. Ker, H.C. Chen, J.H. Lee, C.S. Hsu, L.C. Yang, Evaluation of properties of Ta-Ni amorphous thin film for copper metallization in integrated circuits, J. Phys. Chem. Solids. 69 (2008) 430–434. doi:10.1016/j.jpcs.2007.07.046.

[6] D.W. Matson, High rate sputter deposition of wear resistant tantalum coatings, J. Vac. Sci. Technol. A Vacuum, Surfaces, Film. 10 (1992) 1791. doi:10.1116/1.577748.

[7] A. Arakcheeva, G. Chapuis, V. Grinevitch, The self-hosting structure of ??-Ta, Acta Crystallogr. Sect. B Struct. Sci. 58 (2002) 1–7. doi:10.1107/S0108768101017918.

[8] P.N. Baker, R.F. sputtered tantalum films deposited in an oxygen doped atmosphere, Thin Solid Films. 6 (1970) R57–R60.

[9] W.D. Westwood, F.C. Livermore, Phase composition and conductivity of sputtered tantalum, Thin Solid Films. 5 (1970) 407–420. doi:10.1016/0040-6090(70)90112-4.

[10] N. Schwartz, W.A. Reed, P. Polash, M.H. Read, Temperature coefficient of resistance of beta-tantalum films and mixtures with b.c.c.-tantalum, Thin Solid Films. 14 (1972) 333–347. doi:10.1038/467S2a.

[11] A. Yohannan, Characterization of α and β phases of tantalum coatings, New Jersey Institute of Technology, 2001.

[12] K. Kondo, Stress stabilization of β-tantalum and its crystal structure, J. Vac. Sci. Technol. A Vacuum, Surfaces, Film. 11 (1993) 3067. doi:10.1116/1.578298.

[13] T. Yoshihara, K. Suzuki, Sputtering of fibrous-structured low-stress Ta films for x-ray masks, J. Vac. Sci. Technol. B Microelectron. Nanom. Struct. 12 (1994) 4001–4004.

[14] R. Knepper, B. Stevens, S.P. Baker, Effect of oxygen on the thermomechanical behavior of tantalum thin films during the β-α phase transformation, J. Appl. Phys. 100 (2006) 123508. doi:10.1063/1.2388742.

[15] L.A. Clevenger, A. Mutscheller, J.M.E. Harper, C. Cabral, K. Barmak, The relationship between deposition conditions, the beta to alpha phase transformation, and stress relaxation in tantalum thin films, J. Appl. Phys. 72 (1992) 4918. doi:10.1063/1.352059.

[16] S.P. Baker, R. Knepper, K. Jackson, Aubain, In progress, (2018).

[17] R. Knepper, B. Stevens, S.P. Baker, Effect of oxygen on the thermomechanical behavior of tantalum thin films during the β–α phase transformation, J. Appl. Phys. (2006). doi:10.1063/1.2388742.

[18] E.A.I. Ellis, M.A. Linne, M. Chmielus, S.P. Baker, In Progress, (2018).

[19] R.A. Knepper, Thermomechanical behavior and microstructure evolution of tantalum thin films during the beta-alpha phase transformation, Cornell University, 2007.

[20] E.A.I. Ellis, M. Chmielus, S.P. Baker, Effect of sputter pressure on Ta thin films: Beta phase selection, texture, and stress, Acta Mater. 150 (2018) 317–326.

[21] E.A.I. Ellis, M. Chmielus, S. Han, S.P. Baker, In Progress, (2018).

[22] J.F. Nye, Some Geometrical Relations in Dislocated Crystals, Acta Metall. 1 (1953) 153–162.

[23] R.J. McCabe, A. Misra, T.E. Mitchell, Experimentally determined content of a geometrically necessary dislocation boundary in copper, Acta Mater. 52 (2004) 705–714. doi:10.1016/j.actamat.2003.10.006.

[24] D.P. Field, P.B. Trivedi, S.I. Wright, M. Kumar, Analysis of local orientation gradients in deformed single crystals, Ultramicroscopy. 103 (2005) 33–39. doi:10.1016/j.ultramic.2004.11.016.

[25] D.P. Field, M.M. Nowell, P. Trivedi, S.I. Wright, T.M. Lillo, Local Orientation Gradient and Recrystallization of Deformed Copper, Solid State Phenom. 105 (2005) 157–162. doi:10.4028/www.scientific.net/SSP.105.157.

[26] S. Sun, B.L. Adams, W.E. King, Observations of lattice curvature near the interface of a deformed aluminium bicrystal, Philos. Mag. A. 80 (2000) 9–25. doi:10.1080/01418610008212038.

[27] B.S. El-Dasher, B.L. Adams, A.D. Rollett, Viewpoint: experimental recovery of geometrically necessary dislocation density in polycrystals, Scr. Mater. 48 (2003) 141–145. doi:10.1016/S1359-6462(02)00340-8.

[28] J.W. Kysar, Y.X. Gan, T.L. Morse, X. Chen, M.E. Jones, High strain gradient plasticity associated with wedge indentation into face-centered cubic single crystals: Geometrically necessary dislocation densities, J. Mech. Phys. Solids. 55 (2007) 1554–1573. doi:10.1016/j.jmps.2006.09.009.

[29] W. D. Nix, Elastic and plastic properties of thin films on substrates: nanoindentation techniques, Mater. Sci. Eng. A. 234–236 (1997) 37–44. doi:10.1016/S0921-5093(97)00176-7.

[30] M.A. Haque, M.T.A. Saif, Strain gradient effect in nanoscale thin films, Acta Mater. 51 (2003) 3053–3061. doi:10.1016/S1359-6454(03)00116-2.

[31] V. Srikant, J.S. Speck, D.R. Clarke, Mosaic structure in epitaxial thin films having large lattice mismatch, J. Appl. Phys. 82 (1997) 4286. doi:10.1063/1.366235.

[32] Q. Ma, D.R. Clarke, Size dependent hardness of silver single crystals, J. Mater. Res. 10 (1995) 853–863. doi:10.1557/JMR.1995.0853.

[33] W.D. Nix, H. Gao, Indentation size effects in crystalline materials: A law for strain gradient plasticity, J. Mech. Phys. Solids. 46 (1998) 411–425. doi:10.1016/S0022-5096(97)00086-0.

[34] H. Gao, Y. Huang, W.D. Nix, J.W. Hutchinson, Mechanism-based strain gradient plasticity — I. Theory, J. Mech. Phys. Solids. 47 (1999) 1239–1263. doi:10.1016/S0022-5096(98)00103-3.

[35] N.A. Fleck, J.W. Hutchinson, Strain Gradient Plasticity, in: Adv. Appl. Mech., 1997: pp. 295–361. doi:10.1016/S0065-2156(08)70388-0.

[36] N.A. Fleck, G.M. Muller, M.F. Ashby, J.W. Hutchinson, Strain gradient plasticity: Theory and experiment, Acta Metall. Mater. 42 (1994) 475–487. doi:10.1016/0956-7151(94)90502-9.

[37] B. Klusemann, B. Svendsen, H. Vehoff, Modeling and simulation of deformation behavior, orientation gradient development and heterogeneous hardening in thin sheets with coarse texture, Int. J. Plast. 50 (2013) 109–126. doi:10.1016/j.ijplas.2013.04.004.

[38] E. Demir, D. Raabe, N. Zaafarani, S. Zaefferer, Investigation of the indentation size effect through the measurement of the geometrically necessary dislocations beneath small indents of different depths using EBSD tomography, Acta Mater. 57 (2009) 559–569. doi:10.1016/j.actamat.2008.09.039.

[39] M. Calcagnotto, D. Ponge, E. Demir, D. Raabe, Orientation gradients and geometrically

necessary dislocations in ultrafine grained dual-phase steels studied by 2D and 3D EBSD, Mater. Sci. Eng. A. 527 (2010) 2738–2746. doi:10.1016/j.msea.2010.01.004.

[40] X. Maeder, C. Niederberger, S. Christiansen, A. Bochmann, G. Andrä, A. Gawlik, F. Falk, J. Michler, Microstructure and lattice bending in polycrystalline laser–crystallized silicon thin films for photovoltaic applications, Thin Solid Films. 519 (2010) 58–63. doi:10.1016/j.tsf.2010.07.058.

[41] K. Wloch, P.J. Bentley, Optimising the Performance of a Formula One Car Using a Genetic Algorithm, in: X. Yao, E.K. Burke, J.A. Lozano, J. Smith, J.J. Merelo-Guervós, J.A. Bullinaria, J.E. Rowe, P. Tiňo, A. Kabán, H.-P. Schwefel (Eds.), Int. Conf. Parallel Probl. Solving from Nat., Springer Berlin Heidelberg, Berlin, Heidelberg, 2004: pp. 702–711. doi:10.1007/b100601.

[42] G. Hornby, A. Globus, D. Linden, J. Lohn, Automated Antenna Design with Evolutionary Algorithms, Am. Inst. Aeronaut. Astronaut. (2006) 19–21.

[43] D. Deaven, K. Ho, Molecular geometry optimization with a genetic algorithm., Phys. Rev. Lett. 75 (1995) 288–291. doi:10.1103/PhysRevLett.75.288.

[44] J.A. Wright, H.A. Loosemore, R. Farmani, Optimization of building thermal design and control by multi-criterion genetic algorithm, Energy Build. 34 (2002) 959–972. doi:10.1016/S0378-7788(02)00071-3.

[45] M.M. Eusuff, K.E. Lansey, Optimization of Water Distribution Network Design Using the Shuffled Frog Leaping Algorithm, J. Water Resour. Plan. Manag. 129 (2003) 210–225. doi:10.1061/(ASCE)0733-9496(2003)129:3(210).

[46] Y. Rahmat-Samii, E. Michielssen, Electromagnetic Optimization by Genetic Algorithms, John Wiley & Sons, Inc., New York, NY, 1999.

[47] S.E. Restrepo, S.T. Giraldo, B.J. Thijsse, A genetic algorithm for generating grain boundaries, Model. Simul. Mater. Sci. Eng. 21 (2013) 55017. doi:10.1088/0965-0393/21/5/055017.

[48] A.L.-S. Chua, N.A. Benedek, L. Chen, M.W. Finnis, A.P. Sutton, A genetic algorithm for predicting the structures of interfaces in multicomponent systems., Nat. Mater. 9 (2010) 418–22. doi:10.1038/nmat2712.

[49] J. Zhang, C.-Z. Wang, K.-M. Ho, Finding the low-energy structures of Si[001] symmetric tilted grain boundaries with a genetic algorithm, Phys. Rev. B. 80 (2009) 174102. doi:10.1103/PhysRevB.80.174102.

[50] T. Murata, H. Ishibuchi, H. Tanaka, Multi-objective genetic algorithm and its applications to flowshop scheduling, Comput. Ind. Eng. 30 (1996) 957–968. doi:10.1016/0360-8352(96)00045-9.

[51] F. Fortin, F. De Rainville, M. Gardner, M. Parizeau, C. Gagne, DEAP : Evolutionary Algorithms Made Easy, J. Mach. Learn. Res. 13 (2012) 2171–2175. doi:10.1.1.413.6512.

[52] Y. Hold-Geoffroy, O. Gagnon, M. Parizeau, Once you SCOOP, no need to fork, Proc. 2014 Annu. Conf. Extrem. Sci. Eng. Dicovery Environ. (2014) 1–8.

[53] S. van der Walt, S.C. Colbert, G. Varoquaux, The NumPy Array: A Structure for Efficient Numerical Computation, Comput. Sci. Eng. 13 (2011) 22–30. doi:10.1109/MCSE.2011.37.

[54] E. Jones, T. Oliphant, P. Peterson, SciPy: Open Source Scientific Tools for Python, (2001).

[55] J.D. Hunter, Matplotlib: A 2D Graphics Environment, Comput. Sci. Eng. 9 (2007) 90–95. doi:10.1109/MCSE.2007.55.

[56] T. Blickle, L. Thiele, A Comparison of Selection Schemes Used in Evolutionary Algorithms, Evol. Comput. 4 (1996) 361–394. doi:10.1162/evco.1996.4.4.361.

Driving forces for texture transformation in thin Ag films

Elizabeth A. Ellis[1,*], Markus Chmielus[1,2,*], Ming-Tzer Lin[1,3], Howie Joress[1,4], Kyle Visser[1], Arthur Woll[4], Richard P. Vinci[5], Walter L. Brown[5], and Shefford P. Baker[1,‡]

1. *Cornell University, Department of Materials Science and Engineering, Bard Hall, Ithaca, NY 14853 USA*
2. *University of Pittsburgh, Department of Mechanical Engineering & Materials Science, Benedum Hall, Pittsburgh, PA 15261 USA*
3 *National Chung Hsing University, Graduate Institute of Precision Engineering, 402, Taichung, Taiwan, ROC*
4 *Cornell University, Cornell High Energy Synchrotron Source, Wilson Lab, Ithaca, NY 14853 USA*
5. *Lehigh University, Department of Materials Science and Engineering, Whitaker Laboratory, 5 East Packer Ave, Bethlehem, PA 18015 USA*

* *These two authors contributed equally to this work*
‡ *Corresponding author*

This chapter appeared in Acta Materialia, Vol. 105, pp. 495-504. My contribution to the work was in helping to deposit films and perform in-situ XTD experiments, and in performing stress and driving force calculations.

ABSTRACT

The well-known thickness-dependent (111)-to-(100) texture transformation in thin FCC films is usually attributed to a competition between interface and strain energies. In this model, thin films retain their (111) texture due to the lower energy of the (111) interface, while thick films transform to (100) due to the lower stiffness and thus strain energy of a (100) film. However, recent work has called this model into question, suggesting that neither the stress nor the interface energy play a dominant role in texture transformation. We investigated the driving forces involved in this transformation by using a bulge test apparatus to induce different stresses in thin Ag films under identical annealing conditions. *In situ* synchrotron XRD measurements show the change in texture during annealing, and reveal that applied stresses have no effect on the transformation. Stress analysis shows that differences in driving forces for texture transformation due to applied bulge pressure were significant (≈200 kJ/m^3), suggesting that a

different, much larger driving force must be responsible. Reduction in defect energy has been proposed as an alternative. However, vacancy and dislocation densities must be exceptionally high to significantly exceed the strain energy and do not provide obvious orientation selection mechanisms. Nanotwins in reported densities are shown to provide greater driving force (≈ 1000 kJ/m^3) and may account for orientation selection. The large difference between the calculated strain and defect energies and the driving force for grain growth (21,100 kJ/m^3) casts doubt on the applicability of a thermodynamic model of texture transformation.

7.1. INTRODUCTION

A thickness-dependent (111)-to-(100) texture transition is well known in thin FCC metal films. Fine-grained structures having (111) fiber texture (grains with (111) planes parallel to the film plane and random orientations in the plane of the film) are produced by many deposition processes, regardless of film thickness [1]. During subsequent annealing, the behavior depends on the film thickness. In films that are sufficiently thin, the (111) grains grow normally and the (111) texture is retained. In films that are sufficiently thick, (100)-oriented grains grow at the expense of (111) grains, transforming the film to a (100) fiber texture by what has been described as an abnormal grain growth process [2,3]. Since the orientation distribution determines properties, there has been much interest in this texture transformation [2-17].

The (111)-to-(100) texture transformation has been attributed [2-4] to a competition between strain energy and interface energy. In FCC materials, the (111) orientation has the lowest interface energy, while the (100) orientation has the lowest biaxial modulus. Thus, the interface energy per unit volume decreases as the inverse of the film thickness, while, at a given strain, the strain energy per unit volume is constant with film thickness. This model therefore predicts that a critical thickness exists, below which a film should adopt (111) fiber texture to minimize interface energy, and above which it should adopt a (100) fiber texture to minimize strain energy. This interface/strain energy model is widely cited (*e.g.* [18, 19]) and appears to be the reigning explanation for this phenomenon.

However, recent studies have questioned the role of both stresses and interface energies in this texture transformation. Where stresses are known with certainty, they have been shown to be insufficient to produce the texture transition [10, 11, 15-17]. Indeed, even films removed from their substrates and thus nominally stress-free have been observed to transform [10, 11]. Furthermore, the transitions seem to occur in films of similar thickness regardless of the interface conditions [10, 17]. Thus, it is evident that additional driving forces must be in play. Elimination of microstructural defects (*e.g.* point defects, dislocations, and planar defects) has also been

proposed as a driving force for the texture transformation [15, 17]. However, very little work has been done to identify, separate, and quantify the different driving forces associated with the texture transformation. In only a handful of studies [15-17] have the stresses actually been measured, and even more rarely has the reduction in defect energy been considered [15, 17]. One complication is that films of different thicknesses have not only different stresses [16], but different microstructures [10, 11, 15], and thus possibly different combinations of driving forces that conspire to direct the texture transformation.

We have conducted experiments designed to *impose* different strain energies as driving forces for the transformation, independent from interface and defect energies, so that the results could be compared with energies arising from elimination of different defect types (point, line, and planar). To do this, we used a bulge test apparatus to impose widely different stresses on thin Ag films during annealing and tracked the texture transformation in-situ using synchrotron x-ray diffraction. All films had the same initial structure and thickness. Remarkably, the imposed strain energies had no effect on the kinetics of the texture transformation, indicating that much larger driving forces must be at work. Furthermore, the previously neglected strains that arise due to reduction in excess free volume during grain growth were found to play an important role in the transformation. Calculations show that the strain energy contribution to the driving force for transformation was successfully varied over a range of about 200 kJ/m^3, suggesting that the actual driving force must be much larger. If reduction in defect energy is indeed that driving force, then a minimum defect density with a strong orientation dependence in the as-deposited films is necessary. We show that extremely high densities of vacancies or dislocations would be required, but don't provide an obvious orientation selection mechanism. However, nanotwins in experimentally reported densities can provide a driving force relative to the opposing strain energy and may also provide an orientation selection mechanism. All of the driving forces considered were much smaller than the driving force for grain growth (≈21,100 kJ/m^3) suggesting that kinetics must also play a role.

7.2. EXPERIMENTAL

Substrates were fabricated by etching through the thickness from the backside of Si_3N_4-coated, (001)-oriented, 20 mm x 20 mm Si dies to create either a 2 mm x 12 mm or a 3 mm x 12 mm rectangular nitride membrane in the center of each die (Figure 7.1a and b, and Table 7.1). The Si_3N_4 layer was 210 nm thick for all dies.

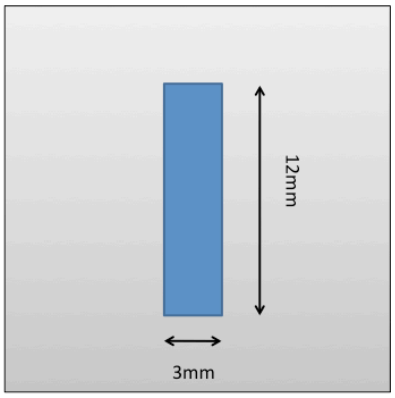

(a)

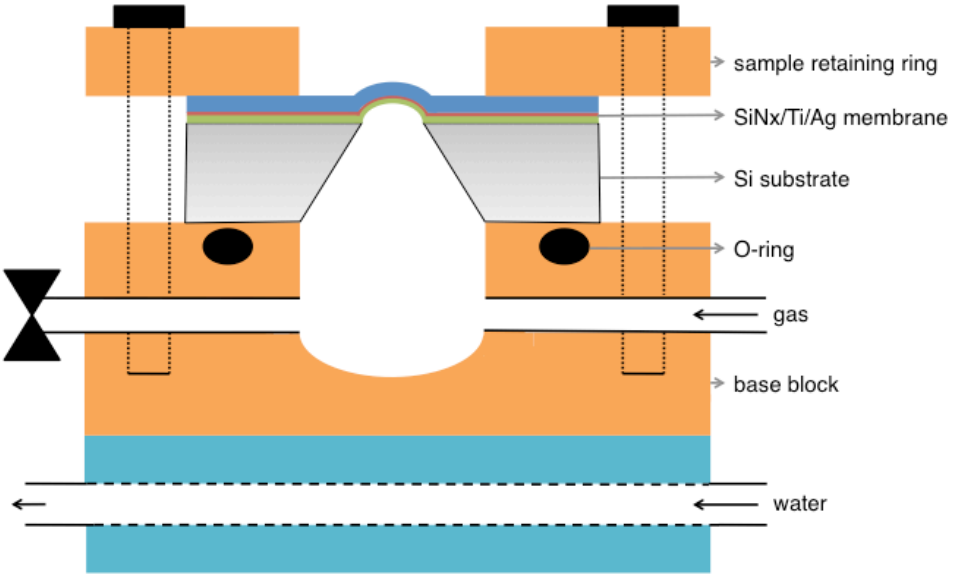

(b)

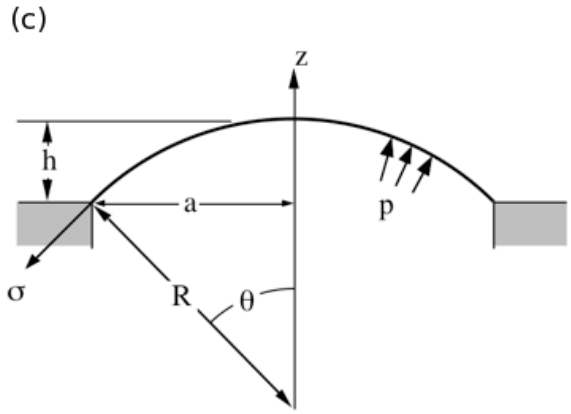

Figure 7.1: Schematic of bulge sample and test. (a) View of Si die from below showing Si_3N_4 membrane. (b) Cross section showing sample mounted on bulge tester with Si_3N_4/Ti/Ag membrane bulged up during testing. (c) Schematic cross section of the bulge test. Bulge width 2a, height h, radius R, and pressure p are as illustrated.

Table 7.1: Sample and test parameters. Pressure is the applied bulge pressure; membrane size is the dimension of the bulge membrane; t_{Ag} is the thickness of the silver layer, $\sigma_{p,70}^{111}$ and $\sigma_{p,70,gg}^{100}$ are the stresses in the silver layer before and after the transformation; R^2 is the correlation coefficient of the Avrami fit; $\Delta\varepsilon_{th,Ag}$, $\Delta\varepsilon_b$, and $\Delta\varepsilon_{gg}$ are the thermal, bulge, and grain growth strains; and $\Delta\phi_{\mathrm{TT}} - \Delta\phi_{\mathrm{GG}}$ is the strain energy driving force for the transformation.

Pressure (kPa)	Membrane size (mm × mm)	t_{Ag} (nm)	$\mathrm{T}_{\mathrm{average}}$ (°C)	$\sigma_{p,70}^{111}$ (MPa)	$\sigma_{p,70,gg}^{100}$ (MPa)	$\Delta\varepsilon_{th,Ag}$	$\Delta\varepsilon_b$	$\Delta\varepsilon_{gg}$	$\Delta\phi_{\mathrm{TT}} - \Delta\phi_{\mathrm{GG}}$
0	2×12	1204	67.8	-83	38	-8.28×10^{-4}	0	1.53×10^{-3}	7
5	3×12	1179	68.2	-35	60	-8.28×10^{-4}	3.23×10^{-4}	1.53×10^{-3}	-113
13	3×12	1179	69.7	31	108	-8.28×10^{-4}	1.08×10^{-3}	1.53×10^{-3}	-198

A titanium adhesion layer followed by a silver film were then deposited onto the nitride on the front side of each die using e-beam evaporation at room temperature. Ti was deposited from 99.995% pure pellets at a rate of 0.5 nm/s to a thickness of 40 nm. Silver films were deposited on top of the Ti adhesion layer from 99.99% pure pellets at a rate of 4.0 nm/s to a nominal thickness of 1200 nm. Both the silver and titanium layers were evaporated out of molybdenum crucibles. The chamber base pressure was between 8.9×10^{-7} and 1.9×10^{-6} Torr ($1.2–2.5 \times 10^{-4}$ Pa) for all depositions. Film thicknesses were measured after deposition using contact profilometry (Table 7.1).

Each sample was then mounted onto a bulge tester that consists of a chamber cut into a brass block with a port and a gas inlet tube (Fig. 7.1b). The sample was clamped over the port using a metal retaining ring that pushed the die against a Viton O-ring, providing a gas-tight seal. The chamber could then be pressurized with helium, causing the Si_3N_4/Ti/Ag membrane in the sample to bulge out as shown in Fig. 7.1c, inducing a net tensile stress in the membrane. The bulge tester was attached to an OFHC copper base block (Fig. 7.1b) whose temperature was controlled by flowing water from a thermostat-controlled heater through a channel in the base block. The temperature was measured using a thermocouple attached to the upper portion of the bulge tester. The measured temperature could be maintained within about 2 ˚C at a nominal annealing temperature of 70 ˚C.

Texture volume fractions were determined *in-situ* during annealing using synchrotron x-ray diffraction (XRD). The bulge tester was mounted in a 6-circle κ goniometer [20] at the G2 beamline of the Cornell High Energy Synchrotron Source (CHESS). The X-ray beam from a Be crystal monochromator had a LaB_6 (NIST SRM 660) calibrated wavelength of 1.2952 Å and a bandwidth of approximately 0.1%. The incident beam, with dimensions of 0.2 x 2.0 mm defined by a set of slits, was aligned such that it was centered on the bulge with the long axis of the rectangular beam parallel to the long axis of the bulge. The diffraction geometry is shown in Figure 7.2.

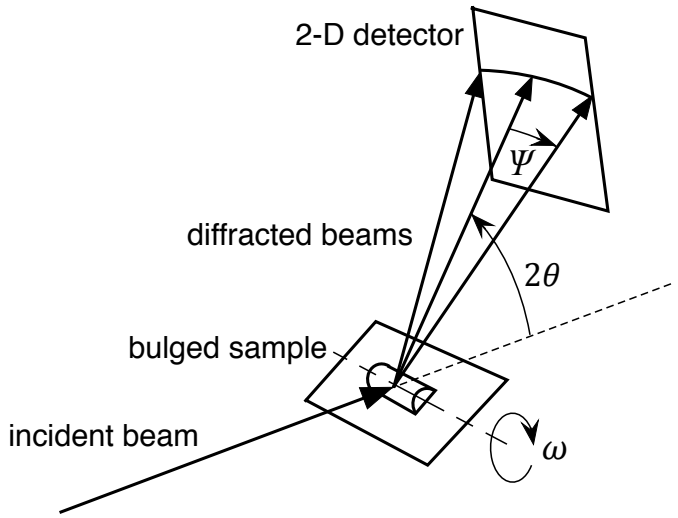

Figure 7.2: Schematic of the x-ray experiment. A 2-D detector was used to capture diffracted intensity from a segment of a diffraction cone. Rocking curves were conducted by rotating about ω.

Diffracted beam intensities were measured using a 2-D detector with a point-to-point resolution of 0.0113° that spanned an angular range of 2.2° in 2θ, and 5.5° in the horizontal plane at $2\theta = 0°$. Use of the 2-D detector was necessary because the transformed films were expected to have very large grain sizes [11]. By capturing a portion of the diffraction cone ($\pm\ \psi$), the chances of capturing peaks from large grains with slight misorientation were increased. Rocking curves were generated by rotating the sample about ω, an axis perpendicular to the incident beam and parallel to the sample surface (ω geometry). The sample height was aligned by setting the beam at $\theta = 0°$ to correspond to the top of the sample retainer and then offsetting by the thickness of the retainer. The maximum bulge height was about 50 μm and was neglected during diffraction experiments on bulged films, introducing a small height error. To minimize air scattering, a He-filled flight path was installed between sample and detector. A N_2 ion chamber upstream from the sample provided a continuous measurement of the incident beam intensity.

To study the effect of stress on the texture transformation, three different samples were tested, each at different applied bulge pressures, and therefore film stresses (Table 7.1). The highest pressure level was selected to provide as much bulge displacement as possible without risk of bursting the membrane during the experiment. One sample was tested with zero applied pressure, and the third was tested at an intermediate pressure. For all three samples, the

procedure was the same: First, the bulge pressure was set. Then, a θ-2θ scan covering a range of $30° \leq 2\theta \leq 80°$ (step size 0.0667°) was performed at room temperature. Next, the water flow to the heater block was started. The sample temperature reached 67 °C within 3 minutes, and stabilized at a final temperature between 67 and 70 °C (Table 7.1) within another 5 minutes. A set of four scans of the (222) and (400) silver diffraction peaks, including 2θ scans (± 1° around the peak center, step size 0.05°) as well as ω rocking curve scans (± 10° around the film normal, step size 1°) of both peaks, was conducted. The photon count was recorded at each pixel in the 2D detector for 0.5 s at each point and a full set of four scans lasted on the order of 4 minutes. These measurements began when heating was started and the full set of four scans was repeated continuously until the end of the experiment. In all three samples, the (222) peak intensity declined and the (400) peak intensity increased during annealing. The XRD scan sequence was terminated when the (400) peak intensity stopped increasing. A final 2θ scan from 30 to 80° was conducted before the bulge pressure was released and the bulge tester and sample were cooled to room temperature.

Following the XRD measurements, the bulge tester was removed from the diffractometer and the stress-strain behavior of the annealed film was determined using a bulge test to obtain an accurate measurement of the stress in the film during the XRD experiments. The bulge height, h, was measured as a function of pressure, p, using a simple Fabry-Perot optical interferometer with the bulge as the fully reflective surface and an optically flat half-silvered mirror as a reference surface. A CCD camera was used to record interference fringe motion as the pressure was increased. The bulge height was obtained by counting the number of fringes that passed a given point. A laser light source with a 532 nm wavelength gave a height resolution of 266 nm.

7.3. RESULTS

The texture evolution was determined from the x-ray data and the stresses were determined from the post-annealing bulge test pressure-height data.

7.3.1 Texture evolution

The only peaks seen during 2θ scans performed both before and after transformation were those associated with (111) and (100) texture components. All films had strong (111) texture before annealing, and strong (100) texture after annealing. Figure 7.3 shows detector images of the diffracted (222) intensity before, and the (400) intensity after annealing, respectively.

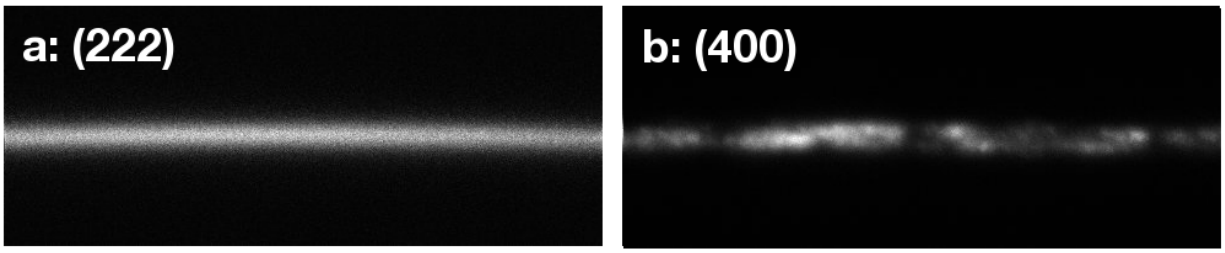

Figure 7.3: Detector images showing segments of (a) (222) diffraction ring before annealing, and (b) (400) diffraction ring after annealing. The smooth (222) ring is consistent with the presence of many small (111) grains before annealing and the spotty (400) ring is consistent with the presence of few large (100) grains formed by anomalous grain growth during annealing. (Note that the maximum intensity in each image is shown as white, so brightness does not indicate relative intensities from image to image.)

The (222) intensity forms a smooth ring segment, consistent with the expected fine (111) grain size in the as-deposited films. The (400) intensity occurs in a few intense spots, consistent with the presence of only a few large (100) grains produced by abnormal grain growth during annealing. For the ω rocking curve scans, the diffracted intensity associated with each measurement was taken to be the total intensity collected by the detector (after background subtraction) at that point — *i.e.* the integrated intensity over the small segment in ψ and 2θ captured by the detector (*e.g.* the total intensity from detector images such as those in Fig. 7.3), which included only the peak of interest. Figures 7.4a and b show the (222) rocking curve before and the (400) rocking curve after annealing for the sample tested at 0 kPa applied pressure. Again, the smoothness of the (222) rocking curve is consistent with the expected fine grain size, while the jagged appearance of the (400) rocking curve arises because of the very large (100) grains in the annealed films. (Note that, since the intensity at each point in the rocking curve is the total detector intensity at that point (*e.g.* Fig. 7.3b), the peaks in the rocking curve don't necessarily correspond to individual grains.) The evolution of the (222) and (400) rocking curve peaks as a function of time during annealing for the sample tested at zero applied bulge pressure

is presented in Figures 7.4c and d, which show that the texture transformation occurred smoothly over a period of about 4 hours.

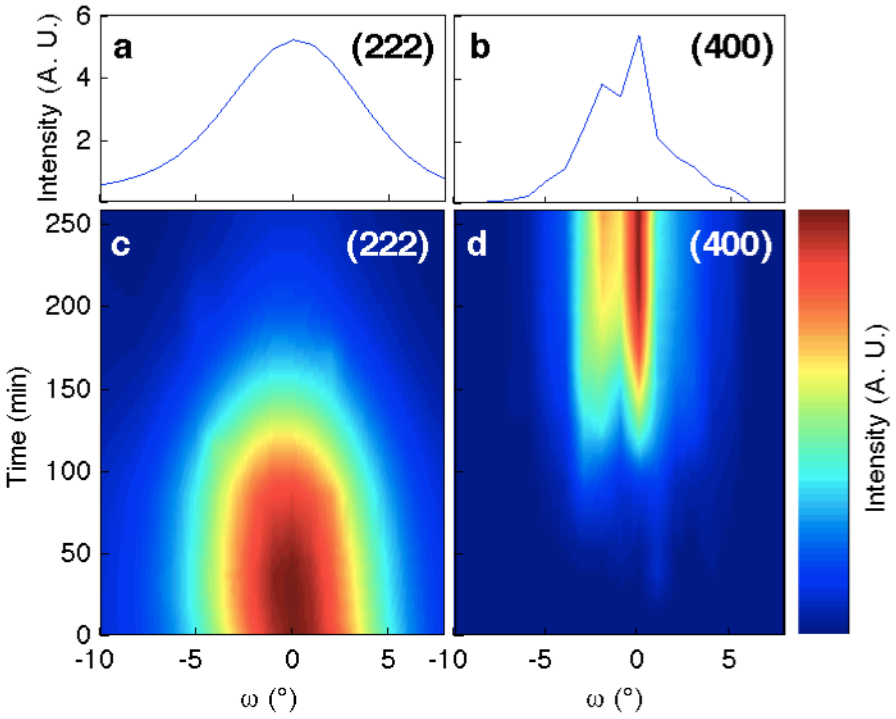

Figure 7.4: ω rocking curves taken during annealing from the sample tested at zero applied bulge pressure. (a) and (b) show, respectively, (222) intensity before annealing and (400) intensity after annealing. (c) and (d) show the evolution of rocking curve intensity with time for the (222) and (400) peaks, respectively. The fine-grained (111) texture component is replaced with a coarse-grained (100) texture component in a classic texture transformation.

Since only peaks corresponding to the (100) and (111) texture components were found, the volume fraction of the 100 texture component, f_{100}, can be estimated by comparing the normalized integrated intensity of the (400) peak with the combined normalized integrated intensities of the (400) and the (222) peaks:

$$f_{100} = \frac{I_{400}}{I_{400} + I_{222}} \tag{7.1}$$

I_{222} is taken to be the area under a Gaussian fitted to each (222) rocking curve, and, because of the irregular shape of the (400) rocking curves, I_{400} was calculated by summing the intensity over the points in each rocking curve.

To account for slight variations in x-ray flux, all count measurements were normalized to the incoming flux as measured by the ion detector upstream of the sample. Corrections were also made to account for changes in sample diffraction volume, Lorentz factor, and scattering factor (structure factor is the same for both peaks) as well as for the solid angle covered by the detector at each 2θ value for each peak. Due to the imperfect alignment of the incident beam to the peak of the bulge, the sample normal was not parallel to the goniometer normal. To account for this, the ω value was shifted by moving the center of the rocking curve for the first (222) peak to zero and the offset applied to all other data taken for that sample.

The texture transformation is quantified by plotting f_{100} *vs*. time as shown in Figure 7.5.

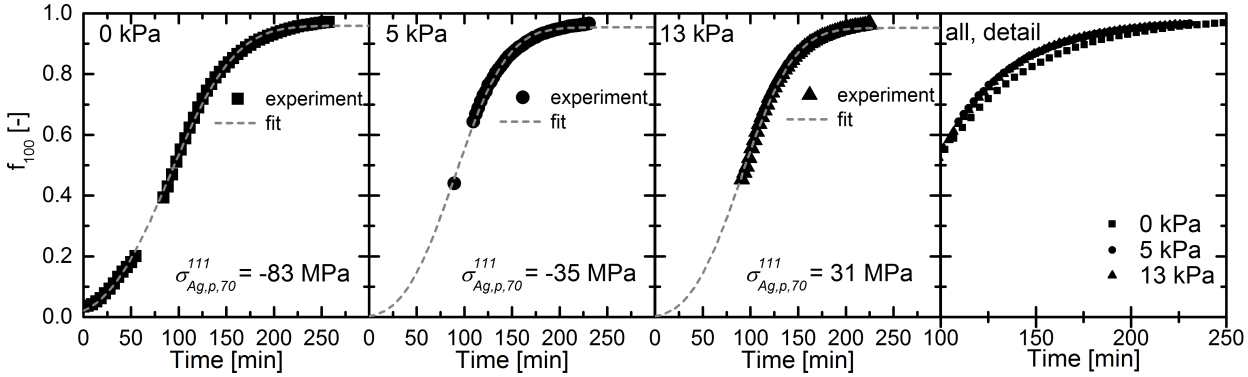

Figure 7.5: Volume fractions of the (100) texture component as a function of time during annealing of samples tested under (a) 0 kPa, (b) 5 kPa, and (c) 13 kPa bulge pressure. (d) Data from all three tests plotted together. X-ray data shown by black symbols; modified Avrami fits (Eq 7.4) shown by dashed lines. All transformation curves are equal to within 5%.

As is evident from the sample tested at an applied bulge pressure of 0 kPa, the texture transformation follows a typical "s-shaped" curve typical of nucleation and growth processes and seen previously in texture transformations [15, 17]. The first sample was tested approximately 27 hours after being removed from the deposition chamber and was untransformed (Fig's 7.3 and 7.4) at the start of the test. However, the second sample (p = 5 kPa) was tested approximately 36 hours after deposition and had an initial value of f_{100} = 0.44, while the third sample (p = 13 kPa) was tested 41 hours after deposition and had an initial value of f_{100} = 0.45. It has been reported that small amounts of impurities dramatically inhibit the texture transformation in Ag films [17]. These results show that if sufficiently pure films are produced, samples transform readily even at room temperature on the scale of days. The transformation curves can be compared if the

transformation data are shifted to account for the extent of transformation that occurred before x-ray measurements began. As evident in Fig. 7.5d, all three samples show virtually indistinguishable transformation kinetics.

7.3.2 Stress calculations

Ideally, one could determine the stresses using the strains calculated from the plane spacing measured using x-rays. However, the bulge test tester did not have sufficiently precise temperature control for this, and the geometry and time precluded measurements of the stresses in the few large (100) grains from which diffraction peaks were captured. Instead, we used the bulge test to determine the stresses. The bulged films consisted of a ≈ 210 nm Si_3N_4 layer, a ≈ 40 nm Ti layer and a ≈ 1200 nm Ag layer. The Si_3N_4 layer, as prepared, had a stress at room temperature of 424 MPa [21]. We ignore any stress in the thin Ti layer, and seek an estimate of the stresses in the Ag layers under pressure and temperature at the beginning of the in-situ annealing experiment (and thus the strain energy available to drive the texture transformation) using a bilayer analysis.

The length-to-width aspect ratios of the rectangular bulged films (Fig. 7.1a and Table 7.1) were all greater than 4 allowing us to use a plane strain bulge test analysis [22, 23]. We modify this analysis for the case of a bilayer membrane comprised of layer 1 with thickness t_1 residual stress $\sigma_{1,0}$, and plane strain modulus S_1, and layer 2 having thickness t_2, residual stress $\sigma_{2,0}$, and plane strain modulus S_2. The total force per unit width along the edges of the bulge membrane, $F_{T,}$ is just the sum of the edge forces in the two layers so that

$$F_T = F_1 + F_2 = \sigma_T t_T = \sigma_1 t_1 + \sigma_2 t_2 \ . \tag{7.2}$$

Thus, the plane strain pressure-height relation presented by Vlassak and Nix [22] and Xiang and Vlassak [23] can be modified for the biaxial bilayer case, resulting in

$$p = \frac{2}{a^2}\left(\sigma_{1,0} t_1 + \sigma_{2,0} t_2\right) h + \frac{4}{3a^4}\left(S_1 t_1 + S_2 t_2\right) h^3 \ . \tag{7.3}$$

In our case, layer 1 is Si_3N_4 for which we use the subscript SiNx and layer 2 is Ag (subscript Ag). The Si_3N_4 layer is amorphous and therefore isotropic, so its plane strain modulus can be found using $S_{\mathrm{SiNx}} = E_{SiNx} \Big/ \left(1 - \nu_{SiNx}^2\right)$ with E_{SiNx} = 150 GPa and ν_{SiNx} = 0.24 [21] giving S_{SiNx} = 159 GPa. The Ag layer is anisotropic. Using tensor elastic constants, we find

$$S_{Ag}^{100} = \frac{3C_{11}^2 - 4C_{12}^2 + C_{11}\left(C_{12} + C_{44}\right) + C_{11}\left(C_{11} - C_{12} - C_{44}\right)\cos\left(4\phi\right)}{4C_{11}} \ , \tag{7.4}$$

and

$$S_{Ag}^{111} = \frac{3C_{11}^2 + 3C_{11}C_{12} - 6C_{12}^2 + 22C_{11}C_{44} + 16C_{44}^2}{7C_{11} + 11C_{12} + 22C_{44}} \ , \tag{7.5}$$

where ϕ is the azimuthal angle relative to the [100] direction. S_{Ag}^{111} is not a function of ϕ and can be evaluated explicitly. Since S_{Ag}^{100} varies with azimuthal angle, the average over ϕ (roughly appropriate for a fiber texture) may be calculated instead. Using published values for single crystal elastic constants [24], this gives plane strain moduli of S_{Ag}^{100} = 69 and S_{Ag}^{111} = 112 GPa.

In principle, one could perform a bulge test of the as-deposited films to determine both the stress in the as-deposited state and the stress under pressure. However, the membrane regions were wrinkled in the as-deposited samples, indicating a net compressive stress at room temperature that made quantitative bulge test measurements impossible [23, 25]. However, the membranes were flat at room temperature after annealing, indicating a net tensile stress. Thus, we conducted bulge tests at room temperature in the annealed films to find the residual stress, and estimated the stress in the Ag layer at the start and end of the transformation by accounting for the changes in stress due to temperature, the texture transformation, grain growth, and the bulge pressure.

This procedure is illustrated in Figure 7.6.

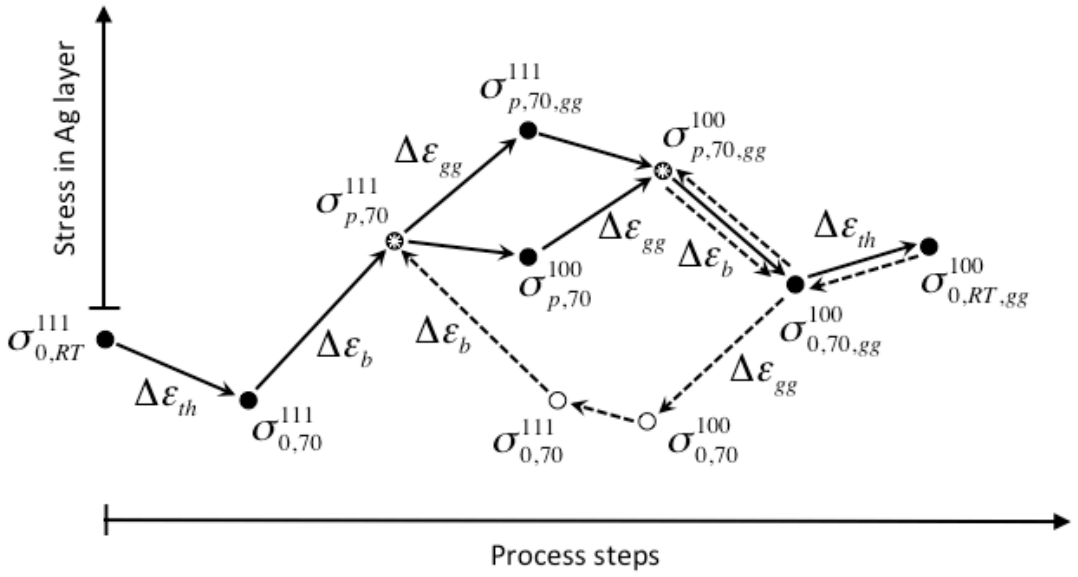

Figure 7.6: Schematic showing how the stresses in the silver layers vary with the different steps in the experimental procedure (solid lines) as well as the thought experiment (dashed lines) leading to an estimate of the stress in the (111) Ag films at temperature and under bulge pressure, $\sigma^{111}_{Ag,p,70}$*, at the beginning of the texture transformation and of the stress in the (100) Ag films at temperature and pressure,* $\sigma^{100}_{Ag,p,70,gg}$*, after the texture transformation (these values are indicated with stars). Remaining symbols are defined in the text.*

Our approach is to go step by step to describe the changes in stress that must occur during the experimental procedures (solid lines, left to right in Fig. 7.6), then, knowing the stresses in the final annealed films from the ex-situ bulge tests, we calculate the actual stresses in the films by going through the steps in reverse order (dotted lines, right to left in Fig. 7.6). Note that, since the stress values depicted in Fig. 7.6 reflect only the behavior of the Ag layer, the *'Ag'* subscript is omitted in this figure for clarity. In this work, the Si_3N_4 layer is assumed to behave elastically throughout the experiment and the contribution of the Ti layer is assumed to be negligible.

We begin with a thought experiment to describe the stresses and their origins during the experimental procedure (solid lines in Fig. 7.6). The Ag layer starts out in the (111) orientation at room temperature. For the moment, we neglect the fact that the bilayers containing the as-deposited films were wrinkled and treat them as if they could somehow be artificially held flat (*i.e.* not buckled), so that the Ag film there would have the same residual compressive stress,

$\sigma^{111}_{Ag,0,RT}$, that it must have in regions where it is directly over the Si substrate. This will allow us to find the correct strain state when the film is bulged.

When the temperature is raised (and the bilayer remains flat!), a thermal strain is imparted to each layer, which, if the temperature dependence of the thermal expansion coefficients can be neglected, is given by

$$\Delta\varepsilon_{th} = \left(\alpha_{Si} - \alpha_{film}\right)\left(T_f - T_i\right) , \tag{7.6}$$

where α_{Si} and α_{film} are the thermal expansion coefficients of the Si substrate and the Si_3N_4 or Ag layers, respectively, and T_{f} and T_{i} the final and initial temperatures. This leads to a stress in the (111) Ag layer of $\sigma^{111}_{Ag,0,70}$. When the bulge pressure is applied, an additional strain given by

$$\Delta\varepsilon_b = \frac{2h^2}{3a^2} , \tag{7.7}$$

is added to both layers, and the stress in the (111) Ag layer, now at the test temperature (subscript *'70'*) and pressure (subscript *'p'*), is $\sigma^{111}_{Ag,p,70}$. When the film then undergoes the texture transformation, two things happen that change the stress and strain state. First the grains grow, eliminating excess free volume from the film and inducing an additional tensile strain given by

$$\Delta\varepsilon_{gg} = \delta\left(\frac{1}{\mathrm{d}_i} - \frac{1}{\mathrm{d}_f}\right), \tag{7.8}$$

where δ is the grain boundary width and d_{i} and d_{f} are the initial and final grain sizes [26]. Second, the new grains that grow have the (100) orientation. This does *not* change the strain directly, but the lower modulus means that the Ag layer supports less stress at a given strain, causing more of the total load to be transferred to the Si_3N_4 layer. These processes occur simultaneously, but we can think of either letting the grains grow first, leading to $\sigma^{111}_{Ag,p,70,gg}$, and then changing the orientation, or we can change the orientation first, leading to $\sigma^{100}_{Ag,p,70}$, and then letting the grains grow. Either way, the layer ends up at $\sigma^{100}_{Ag,p,70,gg}$, the stress state of a pressurized, fully transformed film. Next, the bulge pressure is reduced to zero, inducing a change in bulge strain (Eq. 7.7) leading to $\sigma^{100}_{Ag,0,70,gg}$, as shown in Fig. 7.6. Finally, the sample is

cooled to room temperature, inducing a tensile thermal strain (Eq. 7.6), and leading to a final stress of $\sigma^{100}_{Ag,0,RT,gg}$.

Since the real films were observed to be flat at the end of the actual experimental process, we used the bulge test (Eq. 7.3) to directly measure the residual stress $\sigma^{100}_{Ag,0,RT,gg}$ in the transformed Ag films at room temperature. We could then calculate the values we want, $\sigma^{111}_{Ag,p,70}$ and $\sigma^{100}_{Ag,p,70,gg}$ (points marked with stars in Fig. 7.6), by simply working backwards, from right to left in Fig. 7.6, as indicated by the dashed lines, assuming that: (1) the films remain flat until the bulge pressure is applied, and (2) no plasticity occurs.

First, we fit Eq. 7.3 to bulge test data (not shown). We use the values for the plane strain moduli and the residual stress in the nitride described above (Table 7.1). The residual stress in the Ag layer, $\sigma_{Ag,0} = \sigma^{100}_{Ag,0,RT,gg}$, is the sole variable and is found to be 100 ± 5 MPa. Next, using Hooke's law and the equal-biaxial moduli $Y^{100}_{Ag} = 75$ GPa [17] and $Y_{\mathrm{SiNx}} = E_{SiNx}/\left(1-\nu_{SiNx}\right) = 197$ GPa, we find the residual strains in the Ag and nitride layers, $\varepsilon^{100}_{Ag,0,RT,gg}$, and $\varepsilon_{\mathrm{SiNx},0,\mathrm{RT}}$, respectively, from the residual stresses. We then imagine heating the samples to the test temperature. The residual strains then become

$$\varepsilon_{SiNx,0,70} = \varepsilon_{SiNx,0,RT} + \left(\alpha_{Si} - \alpha_{SiNx}\right)\left(T_{70} - T_{RT}\right) \tag{7.9}$$

And

$$\varepsilon^{100}_{Ag,0,70,gg} = \varepsilon^{100}_{Ag,0,RT,gg} + \left(\alpha_{Si} - \alpha_{Ag}\right)\left(T_{70} - T_{RT}\right) \tag{7.10}$$

Using values for α_{Si}, α_{SiNx} and α_{Ag} of 2.6×10^{-6} K^{-1} [27], 3.3×10^{-6} K^{-1} [28], and 16.5×10^{-6} K^{-1} [29], we find that the thermal strains for this heating process are -3.43×10^{-4} and -8.28×10^{-4} in the nitride and silver layers respectively (Table 7.1). We again apply Hooke's law using the biaxial moduli as described above to find the residual stresses $\sigma_{\mathrm{SiNx},0,70} = Y_{\mathrm{SiNx}}\varepsilon_{\mathrm{SiNx},0,70}$ and $\sigma^{100}_{Ag,0,70,gg} = Y^{100}_{Ag}\varepsilon^{100}_{Ag,0,70,gg}$.

From this point, we can now imagine conducting a bulge test to find the stress at the end of the annealing process, $\sigma^{100}_{Ag,p,70,gg}$; that is, the stress in the (100)-oriented Ag film at pressure and

temperature at the end of the annealing process. We simply apply pressure p and find h from the bulge equation, which now has the form

$$p = \frac{2}{a^2}\left(\sigma_{SiNx,0,70} t_{SiNx} + \sigma^{100}_{Ag,0,70,gg} t_{Ag}\right) h + \frac{4}{3a^4}\left(S_{SiNx} t_{SiNx} + S^{100}_{Ag} t_{Ag}\right) h^3 \ , \tag{7.11}$$

and find the stress in the bulged film from

$$\sigma^{100}_{Ag,p,70,gg} = Y^{100}_{Ag} \varepsilon^{100}_{Ag,0,70,gg} + S^{100}_{Ag} \frac{2h^2}{3a^2} . \tag{7.12}$$

The resulting values of $\sigma^{100}_{Ag,p,70,gg}$ are shown in Table 7.1. The values of the bulge strain are 0, 3.23×10^{-4}, and 1.08×10^{-3} for the films bulged using p = 0, 5, and 13 kPa, respectively (also shown in Table 7.1).

To find the stress in the (111)-oriented film at the beginning of the annealing process, $\sigma^{111}_{Ag,p,70}$, we first imagine releasing the bulge pressure and returning to $\sigma^{100}_{Ag,0,70,gg}$. By removing the bulge pressure, we take advantage of the fact that the hypothetical bilayer membrane remains flat during subsequent calculations, so we may assume that the strain in the nitride layer does not change. Thus, we can calculate the strains in the Ag due to grain growth and the change in stress due to texture transformation without having to calculate a force balance between Ag and SiN_x at each step, as would be the case if the Ag film in the bilayer transformed under pressure. As before, it does not matter which order we choose. In this case we first imagine shrinking the grains back to their as-deposited size. The residual strain in the Ag layer is then

$$\varepsilon^{100}_{Ag,0,70} = \varepsilon^{100}_{Ag,0,70,gg} + \delta\left(\frac{1}{d_{asdep}} - \frac{1}{d_{annealed}}\right) , \tag{7.13}$$

where δ is the thickness of the grain boundary (excess volume per unit area) and d_{asdep} and d_{annealed} are the grain sizes of the as deposited and annealed films, respectively. Based on measurements of blanket films prepared in the same equipment under nominally identical conditions, our films are expected to have initial grain sizes of about 90 nm [30]. Final grain sizes in similar films annealed at similar temperatures (without added bulge stresses) were about 1800 nm [31]. Using

these values and assuming δ = 145 pm (*b/2* [26], where *b* is the magnitude of the Burgers vector [32]), we find the strain due to shrinking of the grains to be -1.53 × 10^{-3} (Table 7.1). Note that this shows that grain growth provides the largest strain in the problem ($\Delta\varepsilon_{th}$ = -8.28 × 10^{-4} (Eq. 7.6, heating), $\Delta\varepsilon_{b,max}$ = 1.08 × 10^{-3} (Eq. 7.7, for the film tested at *p* = 13 kPa), and $\Delta\varepsilon_{gg}$ = 1.53 × 10^{-3} (Eq. 7.8)).

We then allow the orientation of the Ag layer to change to (111). The film remains flat in this step so the strain does not change ($\varepsilon_{Ag,0,70}^{111} = \varepsilon_{Ag,0,70}^{100}$). We again apply Hooke's law, $\sigma_{Ag,0,70}^{111} = Y_{Ag}^{111}\varepsilon_{Ag,0,70}^{111}$, using Y_{Ag}^{111} = 169 GPa [17] leading to a stress of $\sigma_{Ag,0,70}^{111}$ = -173 MPa. Since we assume that the bilayer remains flat until it is bulged, the changes in orientation and grain size in the Ag film do not change the residual strain in the nitride layer. Thus, the residual stress in the nitride is just $\sigma_{SiNx,0,70} = Y_{SiNx}\varepsilon_{SiNx,0,70}$.

To find the stress in the (111)-oriented Ag film at pressure and temperature, we simply apply pressure *p* and find *h* from the bulge equation, which now has the form

$$p = \frac{2}{a^2}\left(\sigma_{SiNx,0,70}t_{SiNx} + \sigma_{Ag,0,70}^{111}t_{Ag}\right)h + \frac{4}{3a^4}\left(S_{SiNx}t_{SiNx} + S_{Ag}^{111}t_{Ag}\right)h^3, \tag{7.14}$$

and find the stress in the bulged film from

$$\sigma_{Ag,p,70}^{111} = Y_{Ag}^{111}\varepsilon_{Ag,0,70}^{111} + S_{Ag}^{111}\frac{2h^2}{3a^2}. \tag{7.15}$$

The values for the films tested at 5 and 13 kPa are -35 and 31 MPa, respectively. Note that though the Ag film in the sample tested at 5 kPa is in compression, the overall stress in the bilayer membrane (Eq. 7.2) remains tensile due to the large tensile stress in the nitride layer, so our assumption that the bilayer remains flat is valid. However, for the film tested at 0 kPa, this assumption is invalid as the overall stress in the bilayer (Eq. 7.2) must be compressive as the film is observed to be wrinkled when no pressure is applied. To find the stresses in the wrinkled films we simply determine the stresses in the bilayer if it were held flat at 70°C and then allow the bilayer to buckle. Values of $\sigma_{Ag,0,70}^{111}$ and $\sigma_{SiNx,0,70}$ for a flat membrane can be found using thermal

expansion coefficients as described above. We then allow the bilayer to buckle by adding an additional strain ε_w to both layers until the overall stress in the bilayer is zero. Equation 7.2 becomes:

$$F_T = F_1 + F_2 = \sigma_1 t_1 + \sigma_2 t_2 = Y_{SiNx}\left(\varepsilon_{SiNx,0,70} + \varepsilon_w\right)t_{SiNx} + Y_{Ag}^{111}\left(\varepsilon_{Ag,0,70} + \varepsilon_w\right)t_{Ag} = 0 \tag{7.16}$$

We find that $\varepsilon_w = 4.94 \times 10^{-4}$, and that the initial stress in the (111)-oriented 0 kPa Ag film at 70°C, $\sigma_{Ag,p,70}^{111}$, is -83 MPa. The values found for $\sigma_{Ag,p,70}^{111}$ for all three films are shown in Table 7.1 and Fig. 7.5.

7.4. DISCUSSION

Figure 7.5 shows both that the Ag films transformed nearly completely from (111) to (100) and that the stress applied via the bulge test had no discernable effect on the texture transformation kinetics. When overlaid one atop the other in Fig. 7.5d, the data from the three samples are indistinguishable to within about 5%. To further quantify this comparison, a modified Johnson-Mehl-Avrami-Konavolav (JMAK) equation [17],

$$f_{100}(t) = c\left[1 - \exp\left(-K\left(t - t_0\right)^n\right)\right], \tag{7.17}$$

was fit to the f_{100} *vs.* time data shown in Fig. 7.5. In this expression, t is the measured time in the experiment and t_0 is the time at which the texture transformation can be thought to have started (accounts for the partial transformation prior to x-ray measurement of the films tested at p = 5 and 13 kPa), K is determined by an Arrhenius relation that contains both nucleation and growth, n is the Avrami exponent, and $c \leq 1$ is a constant that allows for a transformation that does not proceed to completion but approaches a stable mixed texture. The fit parameters, c, K, t_0, and n, are reported in Table 7.2. (It should be noted that due to the missing initial transformation data for the films tested at 5 kPa and at 13 kPa, a range of values for these parameters produce fits of reasonable quality. Since the three films are the same in their as-deposited state, we simply set the time at the first measurement point for the 5 and 13 kPa tests to the same time as that of the

equivalent f_{100} value for the 0 MPa test.) In accord with previous studies [15, 17], the fits show transformation behavior that is consistent with nucleation and growth. The values of $n \approx 3$ suggest 2-D growth [33] as would be expected in a film.

Table 7.1: Fit parameters for Johnson-Mehl-Avrami-Konavolav analysis.

Pressure (kPa)	c	K (1/min)	n	t_0 (min)	R^2
0	0.9447	2.648×10^{-7}	3.012	-39.15	0.9992
5	0.9282	1.412×10^{-7}	3.183	-33.28	0.9937
13	0.9098	1.064×10^{-7}	3.278	-25.53	0.9965

The lack of any significant difference between these curves is remarkable. While it has been demonstrated that films can transform without the level of stress that is required according to the interface/strain energy model [10, 15, 17], it is surprising that the rather significant differences in stress (and, therefore necessarily strain energy) imposed by the bulge tester had no discernable effect on the transformation. This suggests that the actual driving force is significantly larger than the strain energy driving force.

To understand this, we calculate that portion of the driving force that can be attributed to strain energy changes during the bulge test and compare it to other possible driving forces in the problem. Using the stresses under pressure at the beginning ($\sigma^{111}_{Ag,p,70}$) and end ($\sigma^{100}_{Ag,p,70,gg}$) of the texture transformation (points marked with stars in Fig. 7.6), we calculate the difference in the strain energy due to texture transformation in each silver layer from

$$\Delta\phi_{TT} = \frac{\left(\sigma^{100}_{Ag,p,70,gg}\right)^2}{S^{100}_{Ag}} - \frac{\left(\sigma^{111}_{Ag,p,70}\right)^2}{S^{111}_{Ag}}, \tag{7.18}$$

and come up with another surprising result. We find $\Delta\phi_{TT}$ to be -21 kJ/m^3, 41 kJ/m^3 and 160 kJ/m^3 for the samples with no applied pressure, 5 kPa and 13 kPa applied pressure, respectively (Table 7.1)—that is, this analysis predicts that the strain energy actually *increases* during the transformation for all but the sample tested at 0 kPa. This arises because the strain energy is raised more by the increase in the tensile strain due to grain growth (Eq. 7.13) than it is

decreased by the reduction in modulus that accompanies the orientation change. Because the strain due to grain growth is tensile, increases in bulge pressure increasingly *oppose* the grain growth associated with texture transformation. However, this thermodynamic approach to texture transformation does not require that the strain energy decline during the transformation, only that the energy be reduced relative to the case in which the orientation does not change. Thus, to translate this into a driving force for texture transformation, we calculate the change in strain energy, $\Delta\phi_{GG}$, for the same grain growth (with bulge pressure at 70°C) but *without* the orientation change and find $\Delta\phi_{GG}$ to be -28, 154, and 357 kJ/m^3, for the samples tested under 0, 5, and 13 kPa applied bulge pressure, respectively. The differences, $\Delta\phi_{TT} - \Delta\phi_{GG}$, give the driving forces for texture transformation as 7, -113, and -198 kJ/m^3 for the three increasing bulge pressures. (It is interesting to note that, for the films tested at 5 and 13 kPa bulge pressure, some of the increase in strain energy for the transforming films arises because the film undergoes additional strain under constant stress due to the transformation to a lower modulus orientation, so the bulge pressure does work on the film. Use of the load-controlled bulge test thus slightly lowers the driving force for texture transformation compared with a strain-controlled experiment. For example, this accounts for about 19% of the calculated strain energy change in the film tested at 13 kPa.) Thus, by using the bulge test to impose initial stresses that spanned nearly 140 MPa including both tension and compression, we were able to vary the driving force for texture transformation by more than 200 kJ/m^3. For comparison, a difference in interface energies of $\Delta\gamma = \gamma_{100} - \gamma_{111} = 0.184$ J/m^2 [17], in a 1200 nm film provides an energy change of 153 kJ/m^3. So the interface/strain energy model would then predict that the film tested under 13 kPa bulge pressure should transform, but the others should not. The fact that the transformation kinetics are unaffected regardless of whether the strain energy assists the transformation by decreasing 198 kJ/m^3 (film tested at 13 kPa) or opposes the transformation by increasing by 7 kJ/m^3 (film tested at 0 kPa) indicates that the actual driving force for the transformation must be much larger than the difference between these two cases, *i.e.* much larger than $\approx$ 200 kJ/m^3.

With this requirement in mind, we can now consider elimination of defects in the film during grain growth, and the accompanying reduction in total defect energy, as potential driving forces. Of course, a significant driving force arises from elimination of grain boundary area due to grain growth itself. Assuming a grain boundary energy of 1 J/m^2 and a hexagonal columnar grain structure, the total change in grain boundary energy for growth of grains from 90 to 1800 nm as considered above, is about 21,100 kJ/m^3. This is two orders of magnitude larger than our calculated strain energy driving force, which may explain why the transformation is insensitive to the applied bulge strains. Following the logic of the interface/strain energy model, the change energy for a film that changes orientation is only 50 kJ/m^3 (-198 kJ/m^3 strain energy +153 kJ/m^3 interface energy) lower than that of a film that does not, or 0.2% of the grain boundary driving force. The actual driving force for the orientation change must be able to influence the grain growth process so it can't be too much smaller than 21,100 kJ/m^3.

Accordingly, we calculate the change in energy due to elimination of point, line, and planar defects *within* the grains—that is, vacancies, dislocations, and twin boundaries—to determine if and when *differential* defect energies that would be capable of influencing orientation selection during grain growth can be achieved in as-deposited PVD films. This process is a form of recrystallization [34], in which new defect-free grains grow at the expense of pre-existing grains containing high densities of defects. As with the strain energies, it is important to emphasize that the defect energy magnitude alone is not sufficient. An orientation-dependent differential in such energies would be required to generate a texture transformation.

Sonnweber-Ribic et al. [15], studied texture transformations in Cu films and estimated the potential driving force due to elimination of dislocations by assuming that all of the peak width that they observed in x-ray diffraction arose from dislocations. Their analysis gave a dislocation density of $1.25 \times 10^{14}/m^2$. Reducing this to zero would recover about 170 kJ/m^3, which would not be enough to significantly overcome even the opposing interface energy in our films. While dislocation densities in heavily deformed FCC metals can reach 10^{15}-$10^{16}/m^2$, which would translate to total defect energies of 1360–13,600 kJ/m^3, the actual dislocation densities in as-

deposited PVD films are not well known. Studies reporting dislocation densities in this range on the basis of TEM investigations [35, 36] and analysis of x-ray peak widths [37, 38] in as-deposited FCC films have been published. However, Legros *et al*. [36] note that the densities they obtained using TEM should be considered as upper limits with typical values nearer to $10^{12}/m^2$, and Kamminga *et al*. [38] note that dislocation densities obtained by XRD methods are not reliable due to the assumptions (sets of infinite, straight, parallel dislocations) underlying the analysis. Thus, while reduction in dislocation energy can provide sufficient driving force magnitudes, very high dislocation densities, in the 10^{15}-$10^{16}/m^2$ range, would be required. The extent to which such densities actually exist in as-deposited PVD films remains to be determined. More importantly, the orientation selection mechanism is not clear. Sonnweber-Ribic *et al*. [15] claimed that the initial dislocation density was higher in (100) grains, which led to more rapid recovery and ultimately to lower dislocation densities in those grains; which, in turn allowed them to grow at the expense of the (111) grains. However, neither the differential in initial dislocation densities, nor the ability of the dislocation density in (100) to recover faster and farther than that in the (111) grains, nor the reason why the (100) grains should then grow were explained. If the interface/strain energy balance adds only 50 kJ/m^3 as we show above, then one might expect defect-free (111) grains to grow at the expense of both (100) and (111) grains containing dislocations in order to minimize both interface and defect energies.

While vacancy densities in PVD (particularly sputtered) films are often said to be high [39], estimating the change in energy due to elimination of vacancies is difficult, as the actual vacancy concentrations in as-deposited metal films seem also not to be well known. However, assuming a vacancy formation energy of 1.85×10^{-19} J [40], we find that the vacancy concentration must be greater than 3.85×10^{-4} in order for the energy change due to vacancy annihilation to exceed the opposing strain energy of the film with the highest applied bulge pressure. For reference, this is higher than the equilibrium vacancy concentration in silver near the melting point (1.6×10^{-4} [41]). While such high vacancy densities have been seen in simulations [35] of PVD film deposition, it is not yet clear if they exist in real evaporated Ag films. Thus, as with dislocations,

we can conclude that reduction in vacancy energy can provide sufficient driving force to explain our results, but very high vacancy densities, 10^{-3} and larger, would be required. Even if this were the case, the same problems with orientation selection as described regarding dislocations above, would exist.

We note that twin boundaries may also play a role in driving the transformation. Thin FCC metal films produced by sputter deposition have been shown to contain very high densities of twin boundaries in their as-deposited state [4, 6, 14, 42], including several where texture transformation subsequently occurred [4, 6, 14]. Nanotwins with twin boundary spacings of order 10 nm have been reported in Ag films prepared by magnetron sputtering [42]. Assuming a twin boundary energy of 0.01 J/m^2 and a twin spacing of 10 nm, a driving force of 1000 kJ/m^3 could be realized if these defects were eliminated by the texture transformation. While still much smaller than the driving force due to elimination of grain boundaries, this value meets the criterion of significantly exceeding the strain and interface energies in our films. Furthermore, it is possible for nanotwins to provide an orientation selection mechanism. For example, if only (111) grains show such densities of nanotwins [39], then those grains would not grow, while nanotwin-free grains would. Why (100) grains should be singled out from among all other orientations for growth remains to be determined.

Thus, we conclude that, while stored defect energy in the form of dislocations and vacancies could, in principle, provide energies that are large compared with the (obviously ineffective) interface and strain energy contributions and thus might drive the observed texture transformation, very high densities of these defects would be required, and the orientation selection mechanism is not obvious. In contrast, a recrystallization process driven by elimination of excess energy in the form of twin boundaries in experimentally reported densities could provide that driving force, and a simple orientation selection mechanism may be possible.

It is important to note that the approach we are taking here, like the canonical interface/strain energy model [2-4], is purely thermodynamic. This approach runs into conceptual difficulties when we consider that the driving force for grain growth is at least 20 times greater than the

other defect-energy-driven processes that might lead to texture transformation. If we accept a simple picture in which the grain boundary velocity scales with the product of the driving force and the grain boundary mobility, neglect any differences in the grain boundary mobility, and assume that (100) grains—which are not evident in the initial structures in many films that undergo texture transformation [7, 10, 11, 12, 14, 16, 17]—nonetheless exist or are rapidly formed during the initial stages of the transformation, then we would at best expect a 5% differential in driving force to result in only a small difference in the final texture. That is, both the existing (111) grains and any existing (100) grains should grow, but the (100) grains should grow only slightly faster such that the final texture would contain only slightly more (100) than would have been the case without the differential driving force. The fact that in many cases a virtually 100% (111) texture is replaced with a virtually 100% (100) texture [7, 10, 11, 14, 16, 17] suggests that a kinetic argument might be more appropriate. For example, situations where the mobility of (111)/(111) boundaries was significantly lower than that of (111)/(100) boundaries [12], or where the only new defect-free nuclei created had the (100) orientation, would be much more consistent with the experimental data.

As described in Section 2, the Ag/Si_3N_4 bilayers were wrinkled in the as-deposited state indicating that they were in net compression. Due to the wrinkling, the stresses in the as-deposited membranes could not be directly measured. Additional experimental constraints prevented us from being able to determine the stresses in-situ during the transformation. As a result, a circuitous route was followed to estimate the stresses (Fig. 7.6), and thus the strain energy available to drive the texture transformation (Eq 7.12). We can obtain a rough check on validity and accuracy of those stresses as follows:. Since the as-deposited films were wrinkled, the Ag/Si_3N_4 bilayers were in net compression, and since we know the stress in the nitride layer was tensile at 424 MPa, we can use Eq. 7.3 to find that the residual stress in the as-deposited silver films at room temperature, $\sigma^{111}_{Ag,0,RT}$, must be more compressive than -76 MPa. By comparison, if we add the initial thermal strain (Eq. 7.6) to take our calculated value of $\sigma^{111}_{Ag,0,70}$ back to $\sigma^{111}_{Ag,0,RT}$, we find a value of -33 MPa. This is actually quite good agreement considering

the assumptions that were made during the calculations, suggesting that the stresses found for $\sigma_{Ag,0,70}^{111}$ and $\sigma_{Ag,0,RT}^{111}$ are reasonable. For example, we assumed a grain boundary width of $\delta = b/2$ in Eq. 7.13, a fairly common assumption [26]. An increase of only 15% in δ, or a decrease of only 13% in the initial grain size (taken from TEM measurements [30]) would be sufficient to result in a value for $\sigma_{Ag,0,70}^{111}$ of -76 MPa. Similarly, an error in the measurement of the residual stress in the Ag layer at the end of the experiment of only 17 MPa would meet this requirement. Finally, we ignored plasticity in our calculations for two reasons. First, in thermal cycles of very similar films (same deposition process, Ti interlayer, and thickness), significant plastic deformation was not observed until temperatures were above 100°C and stresses above 100 MPa [16]. Second, our calculations resulted in very similar predicted stresses in the as-deposited films for all three samples. Had different amounts of plastic strain occurred in the films due to the different applied bulge pressures, we would have ended up predicting different stresses in the as-deposited films. This would have meant that three nominally identical films prepared in the same way would have had significantly different initial stresses. As this is unlikely, it must be the case either that plastic deformation is small or that it is the same in all films, despite rather different loadings. A crude estimate based on allowing both tensile and compressive stresses to relax in the same way suggests that the calculated stresses are probably within several tens of MPa of the actual values, which, in turn, suggests that the strain energies are known within about 100 kJ/m^3. Our main conclusions are not affected by variations in stresses at this level.

7.5. SUMMARY AND CONCLUSIONS

The established model that describes the thickness-dependent (111) to (100) texture transformation in thin FCC metal films in terms of a competition between strain and interface energies [2-4] has been challenged by reports in which films transformed although the required strain energy was not present [10, 11, 15-17]. A recrystallization process driven by reduction in dislocation energy as an alternative driving force has been proposed [15]. On the assumption that many different driving forces might contribute to the texture transformation, we investigated

those driving forces in the current work by using a bulge test apparatus to impose different strain states to otherwise nominally identical thin Ag films during annealing to vary the strain energy driving force as much as possible. The corresponding texture transformation behavior was characterized using in-situ synchrotron x-ray diffraction. Since stresses could not be measured in-situ, the residual stress in the films after annealing was determined using the bulge test and the stresses at the beginning and end of the transformation were determined using an analysis that included strains due to differential thermal expansion, applied bulge strains, and strains that arise due to elimination of excess grain boundary volume during grain growth.

Strains due to grain growth have not generally been considered in reports of the (111)-to-(100) texture transformation (for example, Thompson and Carel specifically assumed its effects would be negligible [47]), but our analysis makes it clear that they are too large to be ignored. The strain due to grain growth (1.53×10^{-3}) is much larger than either the thermal strain (-8.28×10^{-4}) or the largest applied bulge strain (1.08×10^{-3}). For a certain amount of grain growth, the difference in energy between a film that changes orientation and one that does not gives the driving force for texture transformation. Application of different bulge strains successfully varied the strain energy contribution from +7 kJ/m^3 to -198 kJ/m^3. Considering an opposing change in interface energy of 153 kJ/m^3 [17] these results should have produced films with and without texture transformation according to the widely accepted interface/strain energy model [2-4]. However, despite these significant differences in strain energy, the kinetics of the (111)-to-(100) transformation were unaffected, indicating that the actual driving force for the transformation is much larger.

Assuming that the texture-transformation is a recrystallization process, driven by the reduction in energy that occurs when new defect-free grains grow to replace existing defect-containing grains, we calculated the defect densities that would be necessary to meet this criterion if those defects were dislocations, vacancies, or twin boundaries. Dislocation and vacancy densities would have to exist at very high levels and the orientation selection mechanism is not obvious. However, the necessary driving force can be provided by twin

boundary densities similar to those reported experimentally in nanotwinned Ag films prepared by magnetron sputtering [42] (≈ 1000 kJ/m^3), and an orientation selection mechanism is possible. Additional work to directly confirm the correlation between the presence of the necessary twin boundary density and their elimination during texture transformation is required.

We note that, even in the most extreme cases, the additional driving forces considered are only a fraction of the driving force available for grain growth, suggesting that a simple driving force model may not be appropriate to describe the texture transformation process.

7.6. ACKNOWLEDGMENTS

This work was supported by the National Science Foundation (NSF) via award DMR-1106223. This work is based upon research partially conducted at the Cornell High Energy Synchrotron Source (CHESS) which is supported by NSF and the National Institutes of Health/National Institute of General Medical Sciences under NSF award DMR-0936384. M-T L received support for a sabbatical visit at Cornell University from the Taiwan National Science Council under grant No. NSC 101-2918-I-005-005. The authors would like to thank Prof. Michael O. Thompson for assistance with the construction and operation of the interferometer.

7.7. REFERENCES

1. Polop C, Rosiepen C, Bleikamp S, Drese R, Mayer J, Dimyati A, Michely T, The STM view of the initial stages of polycrystalline Ag film formation, New J Phys 2007;9.
2. Floro JA, Thompson CV, Carel R, Bristowe PD, Competition between strain and interface energy during epitaxial grain growth in Ag films on Ni(001), J Mater Res 1994;9:2411,
3. Zielinski EM, Vinci RP, Bravman JC, Effects of barrier layer and annealing on abnormal grain growth in copper thin films, J Appl Phys 1994;76:4516.
4. Vook, RW, Witt F, Structure and annealing behavior of metal films deposited on substrates near 80K: I. Copper films on glass, J Vac Sci Technol 1965;2:49.
5. Patten JW, McClanahan ED, Johnston JW, Room-temperature recrystallization in thick bias-sputtered copper deposits, J Apply Phys 1971;42:4371.
6. Dahlgren SD, Columnar grains and twins in high-purity sputter-deposited copper, J Vac Sci Technol 1974;11:832.
7. Ohmi T, Saito T, Otsuki M, Shibata T, Nitta T, Formation of copper thin films by a low kinetic energy particle process, J Electrochem Soc 1991;138:1089.
8. Zielinski EM, Vinci RP, Bravman JC, The influence of strain energy on abnormal grain growth in copper thin films, Appl Phys Lett 1995;67:1078.
9. Zielinski EM, Vinci RP, Bravman JC, The effects of processing on the microstructure of copper thin films on tantalum barrier layers, MRS Online Proc Libr 1995;391.
10. Greiser J, Muller D, Mullner P, Thompson CV, Arzt E, Growth of giant grains in silver thin films, Scripta Mater 1999;41:709.
11. Greiser J, Mullner P, Atzt E, Abnormal growth of giant grains in silver thin films, Acta Mater 2001;49:1041.
12. Koike J, Wada M, Sanada M, Maruyama K, Effects of crystallographic texture on stress-migration resistance in copper thin films, Appl Phys Lett 2002;81:1017.
13. Sonnweber-Ribic P, Gruber P, Dehm G, Arzt E, Texture transition in copper thin films: Electron backscatter diffraction vs. x-ray diffraction, Acta Mater 2006;54:3863.
14. Vanstreels K, Brongersma SH, Tokei Z, Carbonell L, De Ceuninck W, D'Haen J, D'Olieslaeger M, Increasing the mean grain size in copper films and features, J Mater Res 2008;23:642.
15. Sonnweber-Ribic P, Gruber PA, Dehm G, Strunk HP, Arzt E, Kinetics and driving forces of abnormal grain growth in thin Cu films, Acta Mater 2012;60:2397.
16. Baker SP, Saha K, Shu JB, Effect of thickness and Ti interlayers on stresses and texture transformation in thin Ag films during thermal cycling, Appl Phys Lett 2013;103:191905.
17. Baker SP, Hoffman B, Timian L, Silvernail A, Ellis EA, Texture transformations in Ag thin films, Acta Mater 2013;61:7121.
18. Thompson CV, Carel R, Texture development in polycrystalline thin films, Mater Sci Eng B 1995;32:211.
19. Thompson CV, Texture evolution during processing of polycrystalline films, Ann Rev Mater Sci 2000;30:159.

20. Nowak DE, Blasini DR, Vodnick AM, Blank B, Tate, MW, Six-circle diffractometer with atmosphere-and temperature-controlled sample stage and area and line detectors for use in the G2 experimental station at CHESS, Rev Sci Instrum 2006;77:113301.
21. Mongkolsuttirat, Kittisun, Time and Temperature Dependence of Viscoelastic Stress Relaxation in Gold and Gold Alloy Thin Films, PhD Dissertation, Lehigh University, 2013.
22. Vlassak JJ, Nix WD, A new bulge test technique for the determination of Young's modulus and Poisson's ratio of thin films, J Mater Res 1992;7:3242.
23. Xiang Y, Chen X, Vlassak JJ, Plane-strain bulge test for thin films, J Mater Res 2005;20:2360.
24. Neighbors JR, Alers GA, Elastic constants of silver and gold, Phys Rev 1958;111:707.
25. Small MK, Nix WD, Analysis of the accuracy of the bulge test in determining the mechanical properties of thin films, J Mater Res 1992;7:1553.
26. Chaudhari, P, Grain-growth and stress relief in thin-films. J Vac Sci Technol 1972;9(1):520.
27. Fransila, Sami, Introduction to Microfabrication, 2nd Ed., John Wiley & Sons, Chichester, West Sussex, England, 2010.
28. Hughey MP, Cook RF, Massive stress changes in plasma-enhanced chemical vapor deposited Silicon nitride films on thermal cycling, Thin Solid Films 2004;460:7.
29. Ashby, Michael F, Materials and the Environment, Butterworth-Heinemann, 2012.
30. Baker SP, Ellis EA. In progress.
31. Dorokhov S, Visser K, Baker SP. In progress.
32. Dubiel M, Brunsch S, Troger L, Temperature dependence of thermal expansion coefficient of silver nanoparticles and bulk material determined by EXAFS, J Synch Rad 2001;8:539.
33. Avrami MJ, Kinetics of phase change, I: General theory, Chem Phys 1939;7:1103.
34. Humphreys, F. J. and M. Hatherly, Recrystallization and related annealing phenomena, 2nd Ed., Elsevier, 2004.
35. Amin-Ahmadi B, Idrissi H, Galceran M, Colla MS, Raskin JP, Pardoen T, Godet S, Schryvers D, Effect of deposition rate on the microstructure of electron beam evaporated nanocrystalline palladium thin films, Thin Solid Films 2013;539:145.
36. Legros M, Cabie M, Gianola D, In Situ Deformation of Thin Films on Substrates, Microsc Res Tech 2009;79:270.
37. Csiszar G, Balogh L, Misra A, Zhang X, Ungar T, The dislocation density and twin-boundary frequency determined by X-ray peak profile analysis in cold rolled magnetron-sputter deposited nanotwinned copper, J of Appl Phys 2011;110:043502.
38. Kamminga JD, Seijbel LJ, Diffraction Line Broadening Analysis if Broadening Is Caused by Both Dislocations and Limited Crystallite Size, J Res Nat Inst Stand Technol;2004;109(1):65.
39. Zhou XW, Johnson RA, Wadley HNG, Vacancy formation during vapor deposition, Acta Mater 1997;45(11):4441.
40. Triftshauser W, McGervey JD, Monovacancy formation energy in copper, silver, and gold by positron annihilation, Appl Phys 1975;6:177.
41. Simmons RO, Balluffi RW, Measurement of the equilibrium concentration of lattice vacancies near the melting point, Phys Rev 1960;119:600.

42. Bufford D, Wang H, Zhang X, High-strength, epitaxial nanotwinned Ag films, Acta Mater 2011;59: 93.
43. Barmak K, Eggeling E, Kinderlehrer D, Sharp R, Ta'asan S, Rollett AD, Coffey KR, Grain growth and the puzzle of its stagnation in thin films: the curious tale of a tail and an ear, Prog Mater Sci 2013;58(7):987.
44. Mullins WW, Two-dimensional motion of idealized grain boundaries, J Appl Phys;27(8):900.
45. Frost HJ, Thompson C, Walton DT, Simulation of thin film grain structures—I. Grain growth stagnation, Acta Metall Mater;38(8):1455.
46. Gottstein G, Schvindlerman L, Triple Junction drag and grain growth in 2D polycrystals, Acta Mater;50(4):703.
47. Thompson C, Carel R, Stress and grain growth in thin films, J Mech Phys Solids 1996;44(5):657.

CHAPTER 8

Summary and Future Work

In this thesis, structural defects have been shown to be instrumental in two thin film transformations. Specific dislocations are shown to be required to form the phase-transformed α-Ta structure, and nanotwins are shown to be a potential source of the driving force for the (111)-to-(100) texture transformation.

In addition, we have shown that it is possible to deposit 100% β-Ta on Si over a wide range of sputter pressures in a very low-oxygen environment. We observe a phenomenon we have called "texture broadening", in which the prominent (002)-β texture component becomes broader as sputter pressure increases, but no other texture component appears. These observations have allowed us to propose mechanism explaining phase formation in Ta films: that depositing Ta interacts with oxygen on the substrate to form a TaO_2 seed layer, upon which β-Ta grows epitaxially. If this layer is removed (e.g. by energetic bombardment), covered (e.g. by organic impurities), or if it cannot form in the first place (e.g. because no oxygen is available), then α-Ta forms. Because we have 100% β-Ta films without α-Ta or oxygen content, we are also able to examine the properties of pure β-Ta, and show that the modulus is anisotropic, and give values for the Hall-Petch constants and resistivity.

In transforming these films to the α phase, we show that the initial microstructure of the β-Ta phase has a strong influence on the magnitude and length of the orientation gradients that appear in the phase-transformed films. We propose a simple rotation mechanism by which the orientation gradients might form, wherein the α phase nucleates with a (111) orientation and the

orientation of the growing grain rotates outward as the phase boundary moves, rotating about axes lying in the plane of the film and perpendicular to the growth direction. This mechanism can reproduce various texture patterns observed in the phase-transformed films, and can explain our observation that seemingly distinct film areas are actually related. To evaluate this mechanism and determine which dislocations are necessary to create it, we generated a model microstructure that replicates a prominent triangular pattern observed in the phase-transformed films, featuring a (111) center, (110) edges, and (100) vertices. We then used a genetic algorithm to create and evaluate dislocation arrays that to replicate the triangular texture pattern in the model microstructure. We represent the dislocations as two independent arrays: a population with sense vectors in the plane of the film, and one with sense vectors parallel to the film normal, each with a burgers vector of the ⟨111⟩ type. We show that in-plane dislocations with $[\bar{1}\bar{1}1]$ and $[\bar{1}11]$ burgers vectors are required to form the observed orientation gradients in the upper right sixth of the model microstructure, and that out-of-plane dislocations provide necessary strain relief from accumulated rotations.

We have also investigated the role of various driving forces in the (111)-to-(100) texture transformation in FCC films. By imposing different stresses via bulge testing and observing the texture transformation *in situ* in Ag films, we show that strain energy cannot provide the necessary driving force for the texture transformation. We suggest instead that nanotwins in the as-deposited (111) films provide both the necessary driving force, and a mechanism for texture selection.

In answering these questions about defect-mediated transformations in metal films, we have of course raised new questions. Suggestions for future work on these topics are listed below:

8.1 On the nature and formation of the *β* phase of Ta

One possible path for future study is on the nature of the *β* phase of Ta itself, which must inform the phase transformation to the stable *α* phase.

Is our proposed mechanism for the formation of *β*-Ta correct? We have proposed that the metastable *β* phase of Ta forms by growing epitaxially on a TaO_2 layer formed during the first few layers of growth on an oxygen-containing substrate. Chapter 3 provides indirect evidence for this formation mechanism by showing correlations between substrate oxygen and *β* phase formation. Future experiments might investigate this directly by examining the first few layers of growth of *β*-Ta films for the presence of a TaO_2 layer. One possible approach would be to use RHEED to study the nucleation and growth of *β*-Ta on oxide substrates, and watch for formation of a TaO_2 layer.

Are there *β*-like phases in other metals? Ta is one of a group of similar BCC metals in Groups 5 and 6 of the periodic table, comprising V, Cr, Nb, Mo, Ta and W. Metastable phases are fairly well established in W [1] and Cr [2], and have also been reported in V [3] and Mo [4]. Metastable Nb has been predicted but never observed [5]. However, relatively little is known about any of these phases besides the *β* phase of Ta. If these phases exist and are similar to *β*-Ta, they might form by a similar epitaxial mechanism to the one we propose in Chapter 3. Future work might therefore focus on depositing V, Cr, Nb, Mo and W in conditions known to produce *β*-Ta and studying the resulting phases. In addition, any metastable phases produced could be annealed in a UHV environment to determine if an orientation gradient microstructure similar to that described in Chapter 5 forms upon transformation to the stable BCC phase. I participated in writing a proposal to study this problem [], which has recently been funded by the NSF.

8.2 On the phase-transformed α-Ta microstructure

Several questions remain about the unusual microstructure observed in phase-transformed α-Ta films, which has long-range orientation gradients and discontinuous grain boundaries.

What dislocations are present in real phase-transformed Ta films? Our efforts to understand the orientation gradients in phase-transformed Ta have so far assumed the geometrically necessary dislocations underlying this microstructure are of the low-energy $(110)\langle 111\rangle$ slip system. Identifying specific real dislocations present in these structures via TEM could tell us which of these 12 slip systems is active in various portions of the film, and could confirm or refute our findings in Chapter 6. Similarly, studying the paths of the dislocation lines in the film will help to inform future generations of modeling as well as suggesting formation mechanisms for texture patterns other than the two described in Chapter 5.

Can we model 3D dislocations paths? The genetic algorithm model described in Chapter 6 uses two independent sets of dislocations: a set of dislocations in the plane of the film, and a set parallel to the film normal. It seems very likely that real dislocations would follow three-dimensional paths through the film. To model such structures would require both adjustments to the genetic algorithm in Chapter 6 and 3D orientation information from real phase-transformed α-Ta films. This might be obtained by examining film cross-sections with precession TEM or even high-resolution EBSD.

8.3 On the role of nanotwins in the (111)-to-(100) texture transformation

The suggestion of nanotwins in as-deposited FCC films provides several new approaches to understanding the (111)-to-(100) texture transformation.

Why and how do nanotwins form in as-deposited films? Nanotwins in thin films have recently become an area of interest, particular because they have been suggested to increase film

strength while preserving ductility [6]. However, the formation of nanotwins is still relatively poorly understood. To understand the role of nanotwins in the (111)-to-(100) texture transformation it is first necessary to understand nanotwins themselves, and one possible approach is to develop a model of film deposition that describes nanotwin formation. Nate Rogers, another student in the Baker group at Cornell, is currently working to develop a Monte Carlo simulation to investigate nanotwin formation.

Why is the (100) texture preferred in the annealed films? The nanotwin driving force proposed in Chapter 8 can explain why (111) grains might be selected against—(111) grains are the only grains in which existing nanotwins will not eventually exit the top or bottom of a growing grain—but does not explain why (100) in particular should be preferred. One possible reason is that a small population of (100) nuclei may exist in the as deposited films. TEM of as-deposited films could help to determine whether these (100) nuclei exist.

8.4 References

[1] H. Hartmann, F. Ebert, O. Bretschneider, Elektrolysen in Phosphatschmelzen. I. Die elektrolytische Gewinnung von alpha- und β-Wolfram, Zeitschrift Für Anorg. Und Allg. Chemie. 198 (1931) 116–140. doi:10.1002/zaac.19311980111.

[2] K. Kimoto, I. Nishida, An Electron Diffraction Study on the Crystal Structure of a New Modification of Chromium, J. Phys. Soc. Japan. 22 (1967) 744–756. doi:10.1143/JPSJ.22.744.

[3] Y. Saito, S. Yatsuya, K. Mihama, R. Uyeda, Crystal structure and habit of fine metal particles formed by gas-evaporation technique; bcc metals (V, Fe, Cr, Mo and W), J. Cryst. Growth. 45 (1978) 501–505. doi:10.1016/0022-0248(78)90483-9.

[4] M. Maoujoud, P. Kons, M. Jardinier-Offergeld, F. Bouillon, C-growth of d.c.-sputtered Mo and W thin films, Thin Solid Films. 238 (1994) 62–69. doi:10.1016/0040-6090(94)90649-1.

[5] N.O. Nnolim, T.A. Tyson, L. Axe, Theory of the structural phases of group 5B–6B metals and their transport properties, J. Appl. Phys. 93 (2003) 4543. doi:10.1063/1.1562751.

[6] L. Lu, X. Chen, X. Huang, K. Lu, Revealing the Maximum Strength in Nanotwinned Copper, Science (80-.). 17004 (2009) 2007–2010. doi:10.1126/science.1167641.